

Nano-Structured Films on Optical Fibres as Chemical Sensors and Actuators

Marziyeh Nazari

M.Sc.

College of Engineering and Science
Victoria University

Submitted in fulfillment of the requirements for the degree of
Doctor of Philosophy

August 2015



To My Parents

Declaration

"I, Marziyeh Nazari, declare that the PhD thesis entitled "Nano-Structured Films on Optical Fibres as Chemical Sensors and Actuators" is no more than 100,000 words in length including quotes and exclusive of tables, figures, appendices, bibliography, references and footnotes. This thesis contains no material that has been submitted previously, in whole or in part, for the award of any other academic degree or diploma. Except where otherwise indicated, this thesis is my own work."

Marziyeh Nazari

August 20, 2015

Abstract

This thesis focuses on using conventional telecommunication optical fibres with nanoporous thin films for different environmental and medical applications. Nanoporous materials are materials with morphological features such as cavities, channels or interstices. Owing to their high surface area, tunable pore size and adjustable framework, they have been used in various applications ranging from catalysis, adsorption, sensing, energy storage and electronics. Two specific nanoporous materials were used, zeolite and MOF (Metal Organic Framework), and a summary of experimental facilities used including important FPI (Fabry-Perot Interference) details (e.g. signal processing) that enable sensor behaviour to be measured is given.

Optical fibre chemical sensors with zeolite thin films were used to detect different selective contaminants in the liquid or gas phase. However, as existing thin film based optical fibre chemical sensors lack the desired sensitivity and specificity for many applications such as chemical and biological analysis, other nanoporous materials were sought.

Thus, in this research, a novel fibre sensor platform of MOF optical fibre thin film was fabricated and demonstrated, which to the best of the author's knowledge, is the first approach towards utilising a MOF coated thin film on optical fibres.

The first application of this MOF optical fibre thin film is to detect some contaminants present at ppm level in Australian waste water systems. These type of thin films, due to their high porosity, can adsorb different types of the molecules (based on their size and chemical bond) and upon adsorption, the refractive index of the thin film is expected to change with this effect being monitored by optical detectors which are connected to

optical fibre. The encouraging results reveal that integration of porous MOF with optical fibre devices presents a promising solution for development of high performance optical chemical sensors.

The second application took advantage of optical fibre and its thin film to trigger release of certain anti-cancer medicines from the thin film. Anti-cancer medicines are toxic and when they go to the body by intravenous infusion, they destroy all live cells, regardless of being healthy or cancerous. By applying our method of delivery, the medicine will go only to the tumours by locating the optical fibre at the appropriate body location with the medicine encapsulated in the thin film.

The sensitive MOF framework (UiO-66) was chosen because it was stable in water and also the presence of contaminants in water can change its refractive index. This change brings about a variation in the intensity of light in the core of the optical fibre which can be analyzed and related to the concentration of analyte. Also, due to the matching pore size of this material and one of the anti-cancer medicines, 5-Fluorouracil (5-FU), this sensitive material can store the drug in its cage and release it by shining the light through optical fibre and weakening the chemical bonds between the drug and the sensitive material.

Possibilities for how both of these applications could be optimized and improved in terms of sensitivity and selectivity in the future for commercial use are provided.

Acknowledgements

I would like to express my deepest appreciation to my supervisors, Prof. Stephen Collins, A/Prof. Matthew R. Hill, Prof. Mikel C. Duke and Dr. Fotios Sidiroglou for all their support, advice and encouragement. They have taught me, both consciously and unconsciously, how good experimental physics is done. I appreciate all their contributions of time, ideas, and funding to make my PhD experience productive and stimulating.

I gratefully thank Dr. Gerard Tobias from Institut de Ciència de Materials de Barcelona (ICMAB-CSIC), Spain for giving me the opportunity to work in his lab and demonstrate my idea on drug delivery.

I am grateful to the College of Engineering and Science, Victoria University, Australia for the scholarship which enabled me to undertake this PhD program.

I especially thank my parents, two sisters and brother. They provided unconditional love and care for me. I love them so much, and I would not have made it this far without them.

Special thanks to my colleagues, specifically Dr. Marta Rubio Martinez and Dr. Kristina Konstas, who formed the core of my research time in the CSIRO. I couldn't have survived in the wet chemistry lab without them.

My special gratitude also goes to my dear friend, Ms Elham Habib Akhyari, who has supported me all through my last year of PhD. Elham is a wonderful and generous friend who has been through a lot and I admire her positive outlook and her ability to smile despite the situation.

I also thank my friends (too many to list here but you know who you are!) for providing support and friendship that I needed.

Contents

Declaration	ii
Abstract	iii
Acknowledgements	v
1 Introduction	1
1.1 Research Objectives	3
1.2 Research Contributions	4
1.3 Thesis Outline	5
2 Optical Fibre Chemical Sensors and Actuators with Nanoporous Materials: a Review	7
2.1 Optical Fibre Chemical Sensors	8
2.2 Optical Techniques Employed in OFCS	13
2.2.1 Fresnel Reflection	13
2.2.2 Fabry-Perot Interferometry (FPI)	14
2.2.3 Optical Fibre Evanescent Wave Sensing	19
2.3 Zeolite Coated Optical Fibre Sensors	22
2.3.1 Ammonia Detection in Gas and Liquid Phases	23
2.3.2 Ethanol, Methanol, 2-Propanol and Toluene Vapours Detection .	24
2.3.3 Trinitrotoluene (TNT) Detection	24

2.3.4	Detection of Mercury (II) Ion in Water	25
2.3.5	Methanol, 2-Propanol and Toluene Detection in Liquid Phase	26
2.3.6	Issues with Zeolite Thin Films	26
2.4	MOFs - Smart Materials	27
2.4.1	MOFs in Water Evaluation	28
2.4.2	MOFs as Drug Delivery Vehicles	33
2.4.3	MOFs Toxicity Studies	34
2.5	Summary	35
3	Experimental Instruments and Methods	36
3.1	Standard Chemical Characterisation Techniques	37
3.1.1	Thermogravimetric Analysis (TGA)	37
3.1.1.1	TGA Instrumentation	38
3.1.2	X-Ray Diffraction (XRD)	39
3.1.2.1	Fundamental Principles of X-ray Diffraction (XRD)	39
3.1.2.2	XRD Instrumentation	40
3.1.3	Gas Adsorption Analysis	41
3.1.3.1	Gas Adsorption Instrumentation	42
3.2	Thin Film Deposition and Characterization	43
3.2.1	Radio Frequency Glow Discharge (RFGD) Plasma Polymerisation	43
3.2.1.1	RFGD Polymerisation Instrumentation	43
3.2.2	Scanning Electron Microscopy (SEM)	44
3.2.2.1	SEM Instrumentation	45
3.2.3	Fourier Transform Infrared Spectroscopy (FTIR)	46
3.2.3.1	FTIR Instrumentation	46
3.2.4	Energy-Dispersive X-Ray Spectroscopy (EDX)	46
3.2.4.1	EDX Instrumentation	47
3.3	Biological Applications	47
3.3.1	Microplate Photometer	47
3.3.1.1	Microplate Photometer Instrumentation	48

3.3.1.2	Microplate Photometer Calibration Curve for 5-Fluorouracil	48
3.4	Optical Components	49
3.4.1	Optical Fibres	49
3.4.1.1	Fibre Couplers	50
3.4.2	Light Sources	51
3.4.2.1	Superluminescent Light Emitting Diode (SLED)	51
3.4.2.2	Erbium ASE Light Source	51
3.4.3	Optical Spectrum Analyzer (OSA)	52
3.4.4	Signal Processing Method	54
3.5	Summary	58
4	Zeolite Coated Optical Fibre for Aqueous Contaminant Detection	59
4.1	The Principles of the Sensor	59
4.2	Synthesis of Zeolite Thin Film on Optical Fibre	60
4.3	Zeolite Material and Optical Fibre Coating Characterization	61
4.4	Contaminants Detection by Zeolite Thin Film Optical Fibre	63
4.4.1	Ammonium Detection	64
4.4.2	4-Aminopyridine Detection	65
4.4.3	Methanol Detection Studies	67
4.4.4	2-Propanol and Ethanol Adsorption Studies in Zeolite Thin Film	69
4.5	Discussion and Summary	70
4.6	Conclusion	72
5	Metal Organic Framework Thin Film Coated on Optical Fibre End-Face for Aqueous Contaminant Detection	74
5.1	Thin Film Role in Sensing	75
5.2	Optical Detection Method	75
5.3	MOF Water Stability	76
5.4	Optical Fibre UiO-66 Thin Film Synthesis	78
5.4.1	Synthesis of UiO-66	78
5.4.2	Synthesis of Optical Fibre UiO-66 Thin Film	81

5.5	Contaminants Detection by UiO-66 Optical Fibre Thin Film	83
5.5.1	Rhodamine-B Detection	84
5.5.1.1	RhB Adsorption Mechanism	87
5.5.2	4-Aminopyridine Detection	87
5.5.2.1	4-AP Adsorption Mechanism	90
5.6	Conclusion and Future Work	91
6	Triggered Release of 5-Fluorouracil from Optical Fibre Thin Film	93
6.1	Potential for Triggered Release as an Alternative to Chemotherapy . . .	95
6.2	Simulation Methodology	96
6.3	5-FU Encapsulation into UiO-66 MOF	99
6.3.1	Encapsulation <i>via</i> Impregnation	99
6.3.2	Encapsulation <i>via</i> Sublimation	104
6.3.2.1	Unit Cell Dimension Calculation	109
6.4	Determining UiO-66 Stability in Different Biological Media	110
6.5	Light Triggered Release of 5-FU from UiO-66 Thin Film	111
6.5.1	Release Amount	114
6.6	Efficiency of the Process	115
6.7	Conclusion and Future Work	116
7	Conclusions and Future Work	118
7.1	Summary of the Thesis Outcome	118
7.2	Future Directions	121
A	Signal Processing Algorithm	123
A.1	Matlab Coding for Signal Processing	123
	References	126

Chapter 1

Introduction

For many centuries humans have pondered the nature of light, seeking to both understand its behaviour and to exploit its properties for enhancing human endeavours. Thus in 2015 the International Year of Light highlighted 1000 years since Al-Haytham's "Book of Optics", Fresnel's description of light as a wave in 1815, Maxwell's formulation of electromagnetism in 1865 and 50 years since the advent of low-loss optical fibre by Kao in 1965.

Scientists and engineers have continued to further seek methods and materials for enhancing and controlling the interaction of light and matter including the identification or control of particular chemical species. Nanoporous materials (a regular porous structure having pore size up to several hundred nanometres) have attracted interest in recent times because they allow particular species to be included within. Importantly, the interaction of light with such species can be used in two ways:

- **Light Sensing:** detection of species within such frameworks;
- **Light Actuation:** triggering the release of species from such a framework.

Every living creature on earth needs water to survive. Monitoring the quality of surface water will help protect our waterways from pollution. Water quality is important not only to protect public health but also as water is used for farming, fishing and mining and contributes to recreation and tourism. If water quality is not maintained, it is not just the environment that will suffer; the commercial and recreational value of our water resources will also diminish.

Light sensing can be used in contaminant detection, as one of the major steps towards controlling water quality is to develop sensor devices that can monitor systems even in harsh environment conditions. The current means of measuring trace amounts of contaminants in water is by taking samples directly from the water, taking them to the laboratory, concentrating and analyzing by chromatography. So, at best, these harmful contaminants will be recorded weekly or monthly depending on regulatory requirements or priorities. This leads to inaccurate results due to not immediate and irregular sample collection or long transportation and handling times. Instead, the water quality management system needs to have a device (e.g. optical fibre chemical sensor) that has the potential to give an instantaneous signal in proportion to the harmful contaminants' concentration in water. Optical fibre sensors have been used in a broad range of applications, taking advantage of the advances in optical fibre technology of the last 50 years. As an example, an optical fibre with a thin film at its end-face forms an effective system to sense chemical species. The presence of chemical species in water can modulate a property of light such as intensity, phase, refractive index or polarization in the

optical fibre thin film. These changes can be detected at the fibre output signal and can be related to the concentration of the chemical species present at the point in water.

Fabricating a light actuator (e.g. optical fibre) is another major challenge for developing a new low cost and high reliability system that would be able to deliver toxic drugs (e.g. anti-cancer medicines) to remote areas in the human body with the same dosage as intravenous infusion. In this application, the optical fibre will serve as a sole light guiding element (waveguide) to its end-face thin film which is encapsulated with a drug, and the light would cause trigger release of the drug from thin film in a second. This drug delivery system would reduce side effects of chemotherapy which are: anemia, bleeding, mouth sores, nausea, diarrhoea and hair loss.

1.1 Research Objectives

The target of this research is to make an advanced optical fibre chemical sensor and actuator device for selective sensing of contaminants in water and drug delivery applications, with a particular focus on implementation of a new thin film technology, stable in water and biological media. This research is significant because it brings advanced materials science in conjunction with optical physics to the forefront of a major need to provide safe drinking water and simplified drug delivery systems. Thus, the main effort was on coating chemically functional materials, zeolite and Metal Organic Frameworks (MOFs) that also interact with light on optical fibres. MOFs specifically have been used in carbon dioxide capture for many years [1–4]. Furthermore, because MOFs have large pore size and surface area, they can be a very good candidate for drug delivery [5–7].

The research objectives were:

- To develop an appropriate and advanced thin film based optical fibre chemical sensor to detect contaminants in water.
- To choose a suitable technology for realizing a practical optical fibre chemical sensor based on the previous aim.
- To design, fabricate and assess a thin film based optical fibre device for drug delivery purposes.

1.2 Research Contributions

The research has led to the following contributions:

- **M. Nazari**, M. R. Martinez, G. Tobias, J. P. Barrio, R. Babarao, F. Nazari, K. Konstas, B. W. Muir, S. F. Collins, A. J. Hill, M. C. Duke, M. R. Hill, (2016): “Metal-Organic Framework Coated Optical Fibers as Light-Triggered Drug Delivery Vehicles”, *Adv. Funct. Mater.* (IF=11.805), *in press*,
<http://dx.doi.org/10.1002/adfm.201505260>
- **M. Nazari**, M. A. Forouzandeh, C. M. Divarathne, F. Sidirolou, M. R. Martinez, K. Konstas, B. W. Muir, A. J. Hill, M. C. Duke, M. R. Hill, S. F. Collins, (2016): “UiO-66 MOF End-Face-Coated Optical Fiber in Aqueous Contaminant Detection”, *Opt. Lett.* (IF=3.292), Vol. 41 (8), pp. 1696-1699;
<http://dx.doi.org/10.1364/OL.41.001696>

- **M. Nazari**, M. R. Hill, M. C. Duke, F. Sidiroglou, S. F. Collins, “Aqueous Contaminant Detection *via* a Metal Organic Framework Thin Film Coating on an Optical Fiber End-Face”, 40th Australian Conference on Optical Fiber Technology, Adelaide, December **2015**
- **M. Nazari**, M. Hill, M. Duke, F. Sidiroglou, and S. Collins, “Selective Sensing of Alcohols in Water Influenced by Chemically Zeolite Coatings on Optical Fiber Sensors”, Proc. SPIE 9157, 23rd International Conference on Optical Fiber Sensors, 915752 (June **2014**); <http://dx.doi.org/10.1117/12.2059516>
- **M. Nazari**, M. C. Duke, M. R. Hill, S. F. Collins and F. Sidiroglou, “Zeolite-Based Optical Fiber Sensor for Selective Sensing of Alcohols in Water”, Australia and New Zealand Conference on Optics and Photonics (ANZCOP), Poster #45. Perth, December **2013**

1.3 Thesis Outline

This thesis is organised into the following chapters:

- Chapter 2 reviews the background information including thin film based optical fibre chemical sensors and their applications particularly as related to the water industry.
- Chapter 3 discusses the instruments and characterization methods which have been used throughout this study.

- Chapter 4 provides instructions and results on zeolite based optical fibre thin film for trace contaminant detection in water.
- Chapter 5 introduces a new type of thin film based optical fibre chemical sensor for water quality testing including the design, manufacture and application of this optical fibre chemical sensor.
- Chapter 6 discusses one of the applications of the chemical optical fibres in biology and mainly as a vehicle for drug delivery.
- Finally, a summary of this research and potential future work is provided in Chapter 7.

Chapter 2

Optical Fibre Chemical Sensors and Actuators with Nanoporous Materials: a Review

Sensing chemicals in gas and liquid systems based on optical fibre technology has several inherent advantages that make it attractive for a wide range of industrial process control [8], environmental monitoring [9–13] and national security [14] applications. Optical fibres are typically small in size, passive, immune to electromagnetic interference, robust in hostile environments [15] and have a capability to provide distributed sensing [16].

Also, optical fibres can be bundled and then inserted into a specialized catheter (tube) that can then be placed at a specified area of the body [17–20].

In this chapter, a brief review on optical fibre chemical sensors (OFCS), the techniques used in the optical detection and their applications particularly in regard to nanoporous materials will be provided.

To the best of the author's knowledge, there are no other reports of a MOF coating at the end-face of an optical fibre.

2.1 Optical Fibre Chemical Sensors

Optical fibre chemical sensors (OFCS) operate by transporting light to provide information about analytes in the environment surrounding an optical fibre. The surrounding environment is usually gas or a liquid. There are two categories of OFCS: extrinsic or intrinsic.

Extrinsic OFCS simply use an optical fibre to transport light to an immobilized indicator, a thin film, deposited at the end-face of the optical fibre. The operation mechanism is based on the fact that alterations in a specific physical property of a medium (gas or liquid) being sensed will cause a predictable change in the light reflection characteristics of the fibre. The reflected light, recorded by the detector, would be analyzed to get information on the concentration of the analyte. A major benefit of extrinsic sensors is their ability to reach places which are inaccessible [21].

In intrinsic OFCS, a portion of the optical fibre cladding is removed and replaced with a chemically selective layer, thereby allowing the guided mode's evanescent field to interact with the analyte. The sensor is then placed directly into the media to be analyzed. Interaction of the analyte with the chemically selective layer creates a change

in absorbance, reflectance, fluorescence, or light polarization. The optical change is then detected by measuring changes in the light characteristic carried by the optical fibre. In short, an intrinsic OFCS uses the optical fibre directly as a detector.

Examples of optical fibre chemical sensors with various coatings is given in Table 2.1. A complete list of optical fibre chemical sensors are in [22, 23]

The main interest in this thesis is the selection of possible contaminants in water that would be absorbed within a thin film, resulting in changes to the optical properties of the film and in turn this change being detected by either an extrinsic or intrinsic detection method. The contaminants in this study were chosen on the following basis:

- **4-Aminopyridine**, $C_5H_6N_2$, a solid colourless pyridine compound (molar mass: 94.1146 g/mol, boiling point: 273 °C and soluble in polar organic solvents) is an extremely effective bird poison. It is registered for use against red-winged blackbirds, blackbirds in agricultural fields, grackles, pigeons, and sparrows around public buildings. 4-Aminopyridine is highly toxic to mammals and when present in water, 75 ppm is the threshold of toxicological concern [34, 35].
- **Ammonium**, NH_4^+ with molar mass of 18.04 g/mol, is highly toxic. Normally blood ammonium concentration is less than 50 $\mu\text{mol/L}$, and an increase to only 100 $\mu\text{mol/L}$ can lead to disturbance of consciousness. A blood ammonium concentration of 200 $\mu\text{mol/L}$ is associated with coma and convulsions. The primary use of ammonium is as a fertilizer for alkaline soils. While ammonia and ammonium are not directly an issue for drinking water safety to humans, indirectly

they are because of interference in disinfection for control of disease causing organisms. Therefore, having low concentrations of ammonia and ammonium in surface water systems is helpful for aquatic life and water treatment for human consumption [36].

- **Methanol**, CH_3OH (molar mass: 32.04 g/mol, boiling point: 64.7 °C), is a colourless liquid that does not bind well to soil. Methanol that makes its way into the ground can move through the soil and enter ground water. Exposure to methanol can occur in the workplace or in the environment following releases to air, water, land, or ground water. Exposure can occur when people use certain paint strippers, aerosol spray paints, wall paints and windscreen wiper fluid [37].
- **Ethanol**, $\text{CH}_3\text{CH}_2\text{OH}$ (molar mass: 46.07 g/mol, boiling point: 78.37 °C), is a labile electron donor and is readily consumed by microorganisms. Laboratory, field and numerical studies have identified a number of key geochemical and microbiological features of such spills which quickly drive into ground water systems [38].
- **2-Propanol**, $(\text{CH}_3)_2\text{CHOH}$ (molar mass: 60.10 g/mol, boiling point: 82.06 °C and miscible in water), may enter the atmosphere, water or soil following waste disposal and has been identified in the air and leachates from hazardous waste sites and landfills. It is emitted in waste water from industrial sources and may be removed by biological oxidation or reverse osmosis [39].
- **Rhodamine-B** (BV10), $\text{C}_{28}\text{H}_{31}\text{ClN}_2\text{O}_3$ (molar mass: 479.02 g/mol, melting point: 210-211 °C and soluble in water at ~ 15 g/L in 20 °C), is mixed with Quinacridone Magenta (PR122) to make the bright pink water colour known as Opera Rose. The textile industry discharges large amounts of Rhodamine-B dye into waste water. It

has been medically proven that drinking water contaminated with Rhodamine-B dye could lead to subcutaneous tissue borne sarcoma which is highly carcinogenic. In addition, other kinds of toxicity such as reproductive and neurotoxicity have been widely and intensively investigated and proved as well by exposure to this dye [40–43].

TABLE 2.1: Examples of optical fibre chemical sensors

Sensing Area	Coating Material	Optical Fibre Type	Sensing Mechanism	Reference
Humidity	Rhodamine-B: hydroxypopyl cellulose	Single polymer-clad silica fibre	Evanescent field absorption	[24]
Humidity	Agarose gel	Tapered fibre	Lossy mode resonances	[25]
Humidity	PolyVinyl Acetate (PVA) and CoCl ₂	SMF-28	Evanescent field absorption	[26]
Humidity	Hydrophilic gel (agarose)	Tapered plastic optical fibre	Intensity modulation technique	[27]
Ammonium	Organic dye immobilized in a porous silica	SMF-28	UV-vis absorption spectrometry	[28]
Ammonia	polyaniline (PANi)	SMF-28	Monitoring electrical and optical responses	[29]
Hydrogen	SnO ₂	SMF-28	UV-vis absorption spectrometry	[30]
Ethanol, Methanol and 2-Propanol	An organometallic compound	Plastic Cladding Optical Fibre	Lossy Mode Resonances	[31]
Taste	Dye/silicon polymer	Plastic-clad silica fibre	Evanescent field absorption	[32]
H ₂ O ₂	Titanium(IV) oxyacetyl-acetate doped Nafion	SMF-28	Evanescent field absorption	[33]

There are various techniques used in extrinsic and intrinsic OFCS, including Fabry-Perot Interferometry (FPI) for extrinsic OFCS and Optical Fibre Evanescent Wave technique for intrinsic OFCS.

In the next sections, a brief review of these techniques will be provided.

2.2 Optical Techniques Employed in OFCS

2.2.1 Fresnel Reflection

The end-face coated reflective sensor operates by measuring the reflection from a surface. Reflection of light may occur whenever light travels from a medium of given refractive index into a medium with a different refractive index. As shown in Figure 2.1, when light travels from a medium of refractive index n_1 into a second medium with refractive index of n_2 , both reflection and refraction of the light occur:

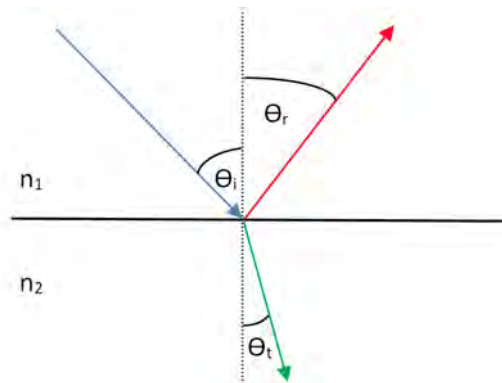


FIGURE 2.1: Light reflection and refraction on the interface of two materials with different refractive indices ($n_1 < n_2$)

The intensity of light reflected from the interface is given by reflectance R , and the fraction refracted given by the transmittance T . If the two materials are both nonmagnetic, the Fresnel equations can be used to calculate R and T . The law of reflection states that the angle of incidence θ_i is equal to the angle of reflection θ_r . When the light is at near-normal incidence to the interface (i.e. $\theta_i = \theta_r = 0$), the reflectance and transmittance are given by [44]:

$$R = \left(\frac{n_1 - n_2}{n_1 + n_2} \right)^2 \quad (\text{Eqn. 2.1})$$

$$T = 1 - R = \frac{4n_1n_2}{(n_1 + n_2)^2} \quad (\text{Eqn. 2.2})$$

For common glass materials, the reflectance is about 4% [44]. In this study, n_2 is the refractive index of analyte and any change in its concentration would bring a change in T and R . However, the deleterious effect of possible fluctuations in the source optical power on sensor output in these devices may detract from sensor performance and it is usually better to use a technique that is not dependent of a simple intensity measurement (e.g. interferometry).

2.2.2 Fabry-Perot Interferometry (FPI)

The Fabry-Perot interferometer is composed of a pair of partially reflective glass optical flats spaced micrometres to centimetres apart, with the reflective surfaces facing each other. Considering a simple FPI, the principle of operation of the fibre optic Fabry-Perot

interferometer is well-established [45] with a review of sensing applications of FPI being provided 3 years ago [46].

In Figure 2.2, the radiation of the source is coupled into the fibre arm (1) and propagates through the coupler to arm (2). Then, some of the radiation is reflected from the end-face of the fibre (2) and the remaining radiation is launched into the second medium (refractive index, n), reflected from the mirror and returned back into the fibre (2). The optical beam reflected from the end-face of the fibre (2) superimposes on the beam reflected from the mirror and is detected through arm (3) in an optical spectrum analyzer (OSA). As a result, the intensity of the optical radiation at OSA has a periodicity that depends on the distance (d) between the fibre arm (2) and mirror, and n .

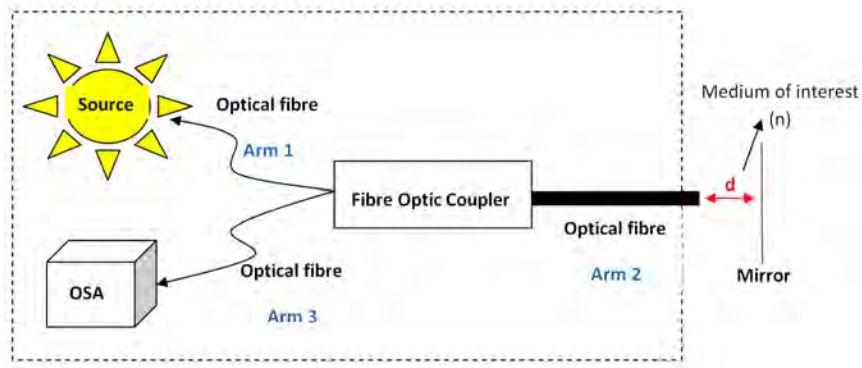


FIGURE 2.2: A schematic of FPI instrumentation technique

In general, the total intensity of the interference signal (I) depends on the two reflected intensities from bare optical fibre in arm (2) (I_1) and from the mirror (I_2) through the equation:

$$I = I_1 + I_2 + 2\gamma I_1 I_2 \cos\left(\frac{4\pi n d}{\lambda} + \varphi\right) \quad (\text{Eqn. 2.3})$$

where γ is the degree of coherency and $(\frac{4\pi n d}{\lambda} + \varphi)$ is the phase difference of the interfering intensities which depends on refractive index of the cavity medium (n), distance

(d) between the fibre arm (2) and mirror and arbitrary initial phase difference of the two reflected intensities (φ).

In a Fabry-Perot interferometer, $I_1 = R_1 I_0$ is the intensity of the light reflected from the end-face surface of the fibre and $I_2 = (1 - R_1)^2 R I_0$ is the intensity of the light reflected from the mirror and returned back into the fibre, where I_0 is the intensity of the source radiation coupled into the fibre, R_1 is the reflectivity of the end-face of the fibre and R is the reflectivity of the mirror. For quartz glass fibre, $R_1 = 0.04$ is the Fresnel reflectance of the boundary surface between two substances - glass with refractive index $n \approx 1.5$ and air with refractive index $n = 1$.

The source radiation can not be exactly monochromatic, and consequently it has limited coherence length. This radiation consists of typically of several frequency modes and the total width of the spectrum $\delta\lambda$ is equal approximately to 3-5 nm. Coherence length l_c of such radiation can be estimated as follows:

$$l_c = \frac{\lambda^2}{\delta\lambda} \quad (\text{Eqn. 2.4})$$

Substituting in this equation the typical parameters of a single mode laser diode we can find that the coherence length equals approximately 0.5 mm. The visibility of an interference fringe depends on the spectral width (and, consequently, upon the coherence length) of the light. Enlargement of the path-length difference of interfering beams decreases the visibility of interference pattern. When the path-length difference reaches the coherence length, the visibility equals to zero.

Generally, because of the divergence of light at the output of the fibre, the percentage of radiation reflected from the mirror and returned back into the fibre depends upon the distance between the fibre and the mirror as given in Figure 2.3.

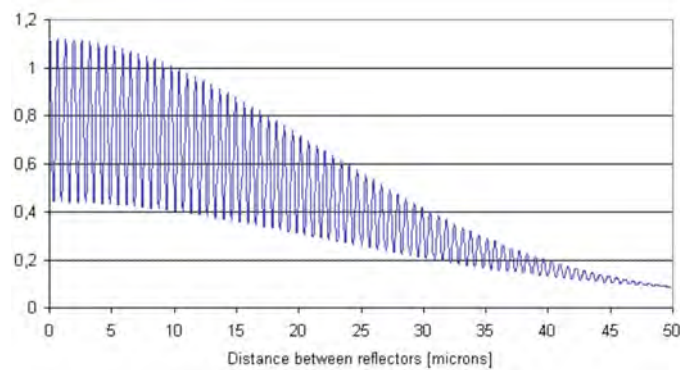


FIGURE 2.3: Dependence of the optical power upon the distance between the fibre and the mirror [47]

The two reflective surfaces (the mirror and optical fibre in arm (2)) could be replaced by a non opaque thin film (etalon). In other words, the end-face of optical fibre can be coated with a reflective thin film of a certain thickness. The light will go through a number of reflections (R) and transmissions (T) in the thin film that are wavelength dependent and thus these reflections and transmissions will make a fringe pattern, as shown in Figure 2.4.

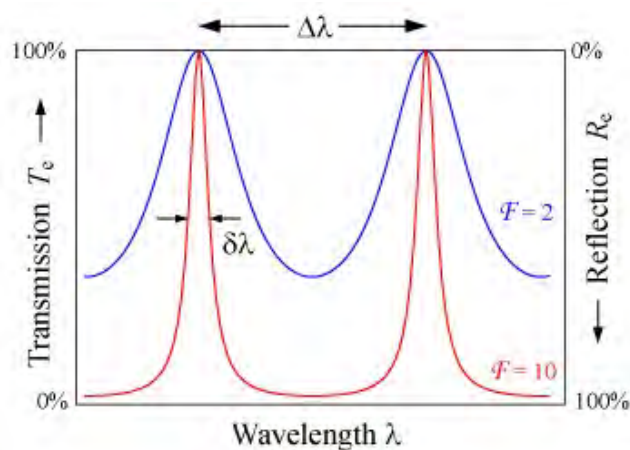


FIGURE 2.4: The transmission of an etalon as a function of wavelength [44]

The visibility of this fringe or interference pattern depends on the following factors [48, 49] :

- The thin film refractive index (n)
- The thickness of the thin film (optical path length) (d)
- Thin film surface reflectance (R)
- The angle the light travels through the thin film (θ)
- The optical wavelength of maximum transmission

While the choice of thin film material and the thickness used for an etalon gives a wide range of design options, its fringe visibility should be improved by ensuring a flat surface at the end of optical fibre and the distal end of the thin film. The thin film roughness could be removed by means of optical fibre polishing; this will enhance the reflectivity of the surface. Figure 2.5 shows the finesse dependence on the thin film reflectance. As can be seen, by increasing the reflectivity, the fringe visibility (finesse) would be increased and in order to have very high finesse factors, highly reflective surfaces are required [50].

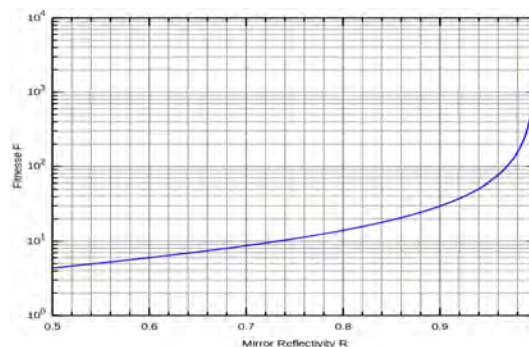


FIGURE 2.5: Finesse as a function of reflectivity [50]

2.2.3 Optical Fibre Evanescent Wave Sensing

An evanescent field generally refers to the portion of the guided mode within an optical fibre that lies in the cladding. In order to enhance evanescent field intensity, either cladding thickness could be reduced or cladding modes could be generated via TFBGs or LPFGs (*vide infra*). In optical fibre sensing, variation in the refractive index of the unclad region of the optical fibre is used for making different sensors to detect or measure different physical or chemical variables [51].

Optical fibre evanescent wave sensing technique is based on coating an unclad portion of an optical fibre with a porous material (thin film). Wet chemical etching using concentrated aqueous solutions of hydrofluoric (HF) acid should be employed in order to remove the fibre cladding. By removing the cladding and coating the unclad area with a thin film, the evanescent field of the propagating mode will interact with the surrounding environment or the analyte. Information about any change in the optical properties of the thin film under investigation could be detected by optical devices. The role of the thin film is to provide a support in which selective analyte molecules (based on size or chemistry) are entrapped into it while others are not [52, 53].

If this coating is applied on a Fibre Bragg Grating (FBG), change in the optical properties of the thin film arises through a shift in the Bragg wavelength. A FBG is a periodic perturbation of the effective refractive index in the core of an optical fibre over a certain length of a few millimetres or centimetres. These perturbations are made by using an intense ultraviolet (UV) source such as a UV laser. Figure 2.6 shows a schematic of the FBG.

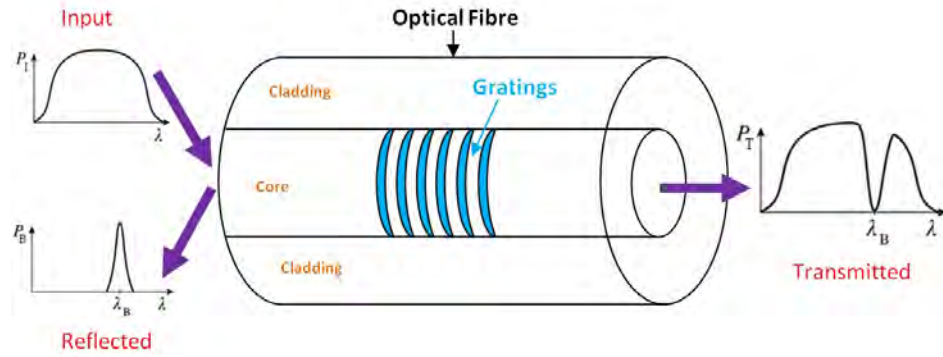


FIGURE 2.6: Schematic structure of a fibre Bragg grating (FBG)

The refractive index perturbation leads to the reflection of light with a certain wavelength and transmitting all others for which a Bragg condition is satisfied:

$$\frac{2\pi}{\Lambda} = 2 \times \frac{2\pi n_{eff}}{\lambda} \Rightarrow \lambda = 2n_{eff}\Lambda \quad (\text{Eqn. 2.5})$$

where Λ is the grating period, λ is the vacuum wavelength, and n_{eff} is the effective refractive index of the fibre.

If the variation of the refractive index is at an angle to the optical fibre axis, a Tilted Fibre Bragg Grating (TFBG) is made. The angle of tilt in a TFBG has an effect on the reflected wavelength and bandwidth. Since the tilt angle and refractive index modulation determine coupling efficiency and the bandwidth of cladding mode resonance peak, the transmission characteristics of TFBGs provide a great amount of information related to the fibre and grating structures [54]. Figure 2.7 shows a schematic of the TFBG.

Typical FBGs have grating periods of a few hundred nanometres, while Long Period Bragg Gratings (LPGs) have gratings in the order of hundreds of microns and often with tilted grating planes. Such gratings can couple modes with the same propagation direction. When a LPG is coated with a thin film, a core mode can be coupled to

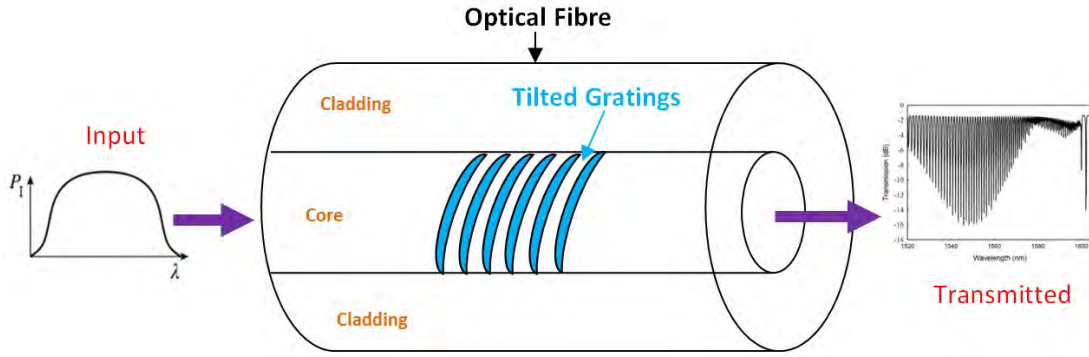


FIGURE 2.7: Schematic structure of a tilted fibre Bragg grating (TFBG)

cladding modes. In other words, coupling is observed between the core and circularly symmetric cladding modes of odd order. TFBGs and LPFGs have only transmitted spectra while normal FBGs show both transmitted and reflected spectra.

Phase matching in a LPG between the mode propagating in the core of the fibre and a forward propagating cladding mode is achieved when Eqn. 2.6 is satisfied:

$$\lambda = [n_{eff}(\lambda) - n_{cladd}^i(\lambda)]\Lambda \quad (\text{Eqn. 2.6})$$

where Λ is the period of the LPG, $n_{cladd}^i(\lambda)$ is the refractive index of the i th cladding mode, and n_{eff} is the effective refractive index of the propagating core mode at wavelength λ .

The exact form of the spectrum is sensitive to the period of the LPG, the length of the LPG and to the local environmental factors (e.g. temperature, strain, bend radius and the refractive index of the medium surrounding the fibre). Any change in the above parameters would modify the period of the LPG or the differential refractive index of the core and cladding modes which, in fact, dictates the phase matching conditions for coupling to the cladding modes. The LPG's sensitivity to a particular parameter depends

on the composition of the fibre and the order of the cladding mode to which the guided optical power is coupled and is different for each attenuation band [55, 56].

In the literature a very wide range of thin films have been synthesized on optical fibres. Here those that are most relevant to the work of this thesis are discussed.

2.3 Zeolite Coated Optical Fibre Sensors

The word “zeolite”, which means boiling stone in the Greek language, is a microporous crystalline aluminosilicate composed of TO_4 (T = Si, Al, Ga, Ge, Fe, P and Co) tetrahedral with oxygen atoms connecting neighboring tetrahedral. Zeolites can be represented by the general formula of $M_{n/m}^{m+} \cdot [\text{Si}_{1-n}\text{Al}_n\text{O}_2] \cdot n\text{H}_2\text{O}$, where $M_{n/m}^{m+}$, $[\text{Si}_{1-n}\text{Al}_n\text{O}_2]$ and $n\text{H}_2\text{O}$ are extraframework cations, framework, and sorbate phase, respectively. In general, zeolites are crystalline aluminosilicate with uniform subnanometre or nanometre scale pores and unique surface properties that are suitable for highly selective gas or analyte adsorption. The effective pore sizes of zeolites vary from ~ 0.3 to > 1 nm, depending on the crystal's structure. Figure 2.8 shows the pore system in the MFI-type (Mordenite Framework Inverted) zeolite with straight channels in y-direction and interconnecting channel system in 3 dimensions.

Thus zeolite materials are capable of discriminating between chemicals by molecular sieving. The Si/Al ratio in the zeolite framework can be adjusted by substitution of Al for Si to create positive charges in the framework and give selectivity to framework [58]. Since 1980, several types of zeolites have been synthesized into polycrystalline thin

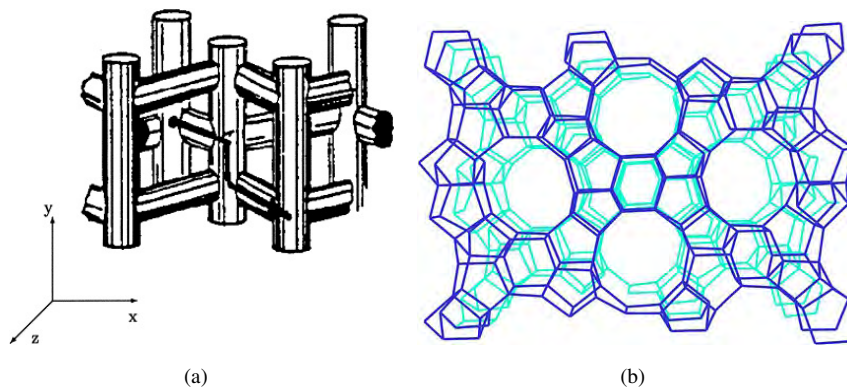


FIGURE 2.8: Pore system in the MFI-type zeolite (a) 3-D interconnecting channel system and (b) straight channels in y-direction [57]

films for molecular separations [59–66], heavy metal removal from water [67] and sensor applications [68]. In the next sections, applications of zeolite thin film coated optical fibres in contaminant detection in gas and liquid phases will be discussed.

2.3.1 Ammonia Detection in Gas and Liquid Phases

A modified ZSM-5 zeolite thin film (with Si/Al ratio of 15/20) coated long period fibre grating (LPFG) sensor was used for *in situ* detection of ammonia by Tang et al. [69] in 2009. Upon loading the ammonia molecules, the refractive index of the zeolite film changed and its close vicinity to the optical fibre containing the LPFG produced a large response giving high sensitivity. In this work, the zeolite - coated LPFG was treated in a 0.1 M NH_4Cl solution after the template removal step to exchange the Na^+ ions with NH_4^+ . The sensor exhibited high sensitivity to NH_3 at ppm levels. The zeolite thin film is shown in Figure 2.9.

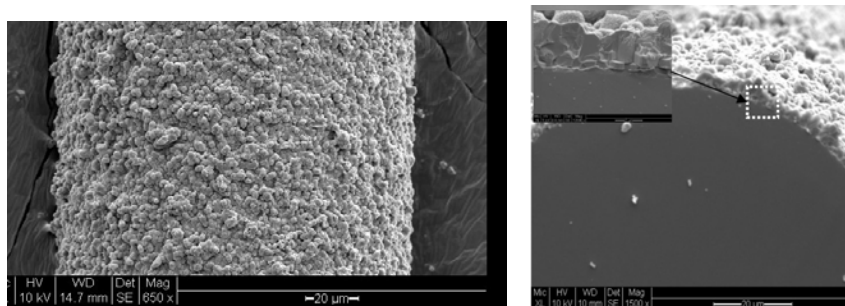


FIGURE 2.9: SEM image of ZSM-5-LPFG sensor [69]

2.3.2 Ethanol, Methanol, 2-Propanol and Toluene Vapours Detection

2-Propanol was detected using an optical fibre chemical sensor which had been coated with zeolite thin film on its end face. The 2005 paper by Xiao et al. [70] reported that by using a zeolite thin film, their sensor responded very fast (within 1 s) to a 2-propanol concentration of 1.3 mol% in N₂ mixture. They had used a standard single-mode optical fibre in a synthesis solution of 30 ml of water, 5.65 ml of tetrapropyl ammonium hydroxide (TPA) and 10.2 ml of tetraethyl orthosilicate. The SEM images of the optical fibre with and without zeolite thin film are shown in Figure 2.10.

2.3.3 Trinitrotoluene (TNT) Detection

Walsh et al. [71] in 2006 used a previously made sensor to detect Trinitrotoluene (TNT) trace vapour in helium carrier gas. The sensor was made of a dense silica thin film grown on the straight-cut endface of a standard 125 μm diameter telecommunication optical fibre. Experiments were conducted for more dilute TNT/helium gas mixtures by diluting the stream (10 mg of TNT flake with helium in a flow rate of 3 cc/min) with

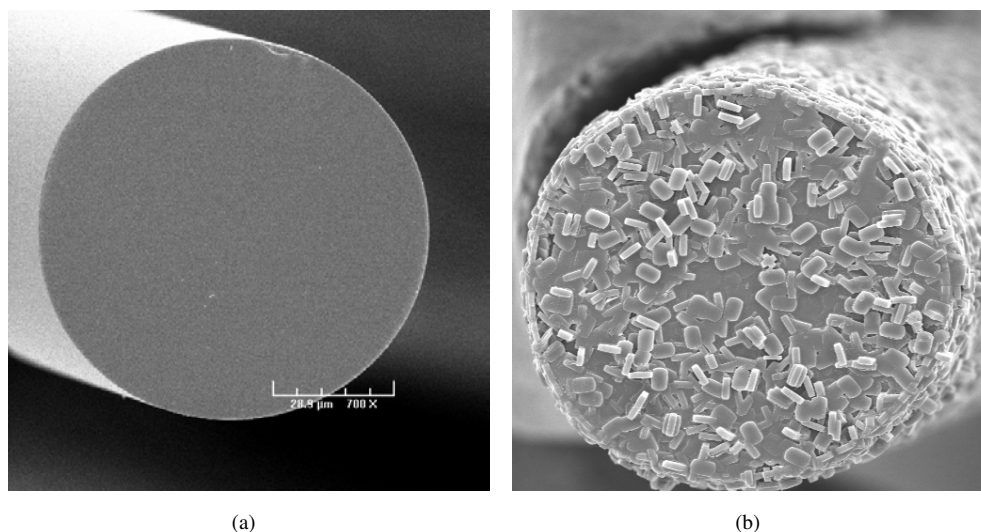


FIGURE 2.10: a) SEM image of the cleaved end-face of a single mode optical fibre, b) end-face SEM image of a MFI zeolite-coated optical fibre [70]

helium by 3 to 10 times. The results showed that the sensor was capable of detecting TNT vapour at low ppb level.

2.3.4 Detection of Mercury (II) Ion in Water

An integrated zeolite-captured silver optical fibre chemical sensor has been developed by Liu et al. [72] in 2011. The sensor was made by coating a b-oriented zeolite thin film onto the end surface of an optical fibre. Then Ag^+ ions were loaded onto the zeolite crystal via ion exchange. The exchanged Ag^+ ions were reduced in the zeolite channel by formaldehyde. By monitoring the reflection intensity change, the resulting Ag-embedded zeolite optical fibre was used for *in situ* Hg^{2+} detection in water. It is known that Ag nanoparticles can selectively react with Hg^{2+} ions in solutions with high sensitivity, and thus the crystal's refractive index changed when the Hg^{2+} ions reacted with the zeolite-captured Ag particles so that, the reflected light intensity from the crystal surface changed. After the Hg^{2+} ions reached equilibrium with the captured silver

in 20 ppm Hg²⁺ solution, the crystal's refractive index did not change any more and the reflected intensity remained constant.

2.3.5 Methanol, 2-Propanol and Toluene Detection in Liquid Phase

An optical fibre intrinsic Fabry-Perot interferometric (IFPI) chemical sensor was developed by Liu et al. [73] by fine-polishing a thin layer (10 μ m) of polycrystalline nanoporous MFI zeolite on the cleaved endface of a single mode fibre. The concentration of methanol in DI water was varied from 1 ppm to 13.1% by volume. When the concentration reached about 1000 ppm, the optical thickness increased with increasing methanol concentration. Based on the results, the sensor showed a detection limit of about 1000 ppm for methanol in water. In another experiment the concentration of 2-propanol in water was staircase increased from 1 ppm to 25600 ppm. The sensor response had a detection limit of 5 ppm for 2-propanol in water. The concentration of toluene in water was changed from 1 ppm to 150 ppm monotonically and a similar threshold behavior was observed in the sensor response, indicating a detection limit of about 2 ppm for toluene in water.

2.3.6 Issues with Zeolite Thin Films

The literature review reported in the previous sections suggests that industry and science needs to pay attention to make new functional materials. As already mentioned, either the coating materials were not stable in water/biological mediums or they did not have a good coverage to detect different heavy organic molecules (herbicides and pesticides)

in water. This knowledge gap is an important issue relating to waste water quality monitoring and purification. Also, the current science is looking for new materials for broad applications in both water purification and drug delivery in medicine. In the following sections, a brief description of a new functional material and its utilisation in water treatment and drug delivery will be discussed.

2.4 MOFs - Smart Materials

Metal Organic Frameworks (MOFs) are a class of materials consisting of a metal ion or cluster of metal ions coordinated to organic linkers called ligands. They form one- two- or three- dimensional structures which are porous. This coordination network is an extension, through repeating coordination entities, in one dimension, but with cross-links between two or more individual chains, loops, or spiro-links, or a coordination compound extending through repeating coordination entities in two or three dimensions. The choice of metal and linker defines the structure and hence properties of the MOF. The metal's coordination preference influences the size and shape of pores by dictating how many ligands can bind to the metal and in which orientation. Careful selection of MOF constituents can yield crystals of ultrahigh porosity and high thermal and chemical stability [1, 4, 74]. The pores are stable during elimination of the solvent molecules and could be used for the storage of gases such as hydrogen and carbon dioxide. Other possible applications of MOFs are in gas purification, in gas separation, in catalysis and as sensors [75]. Figure 2.11 shows the MOFs structures (1D, 2D, and 3D) reported in the Cambridge Structural Database (CSD) from 1971 to 2011. The trend shows a striking

increase during this period for all structure types. In particular, the doubling time for the number of 3D MOFs (inset) is the highest among all reported metal-organic structures.

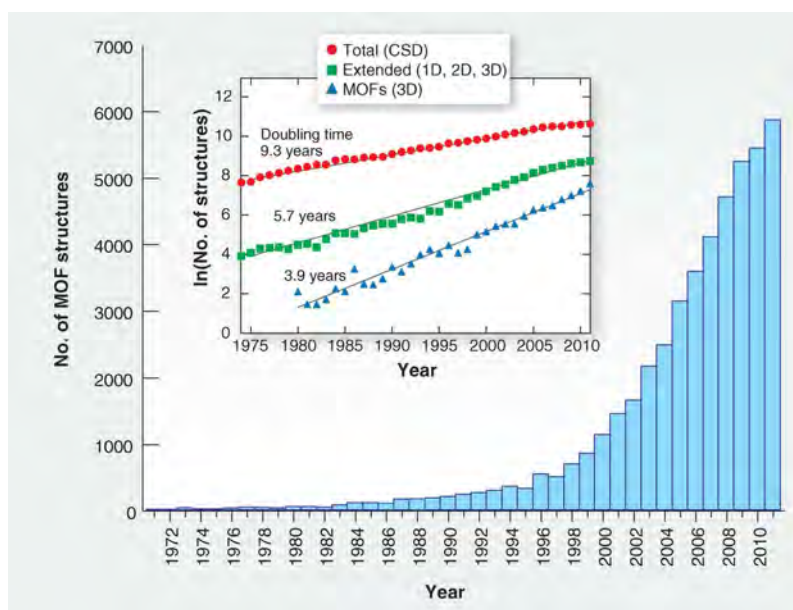


FIGURE 2.11: MOFs structures (1D, 2D, and 3D) reported in the Cambridge Structural Database (CSD) from 1971 to 2011 [75].

The organic units are typically mono-, di-, tri-, or tetravalent ligands. Subunits of a MOF, called secondary building units (SBU), can be described by topologies common to several structures. Each topology, also called a net, is assigned a symbol, consisting of three lower-case letters in bold. Inorganic secondary building units (A) and organic linkers (B) are shown in Figure 2.12.

2.4.1 MOFs in Water Evaluation

The issue of supplying clean water and sanitation has become a major problem due to increasing population in the world. In the past decades, a few desalination techniques have been developed for seawater [76]. In particular, reverse osmosis currently dominates, accounting for approximately half of the installed desalination methods worldwide [77].

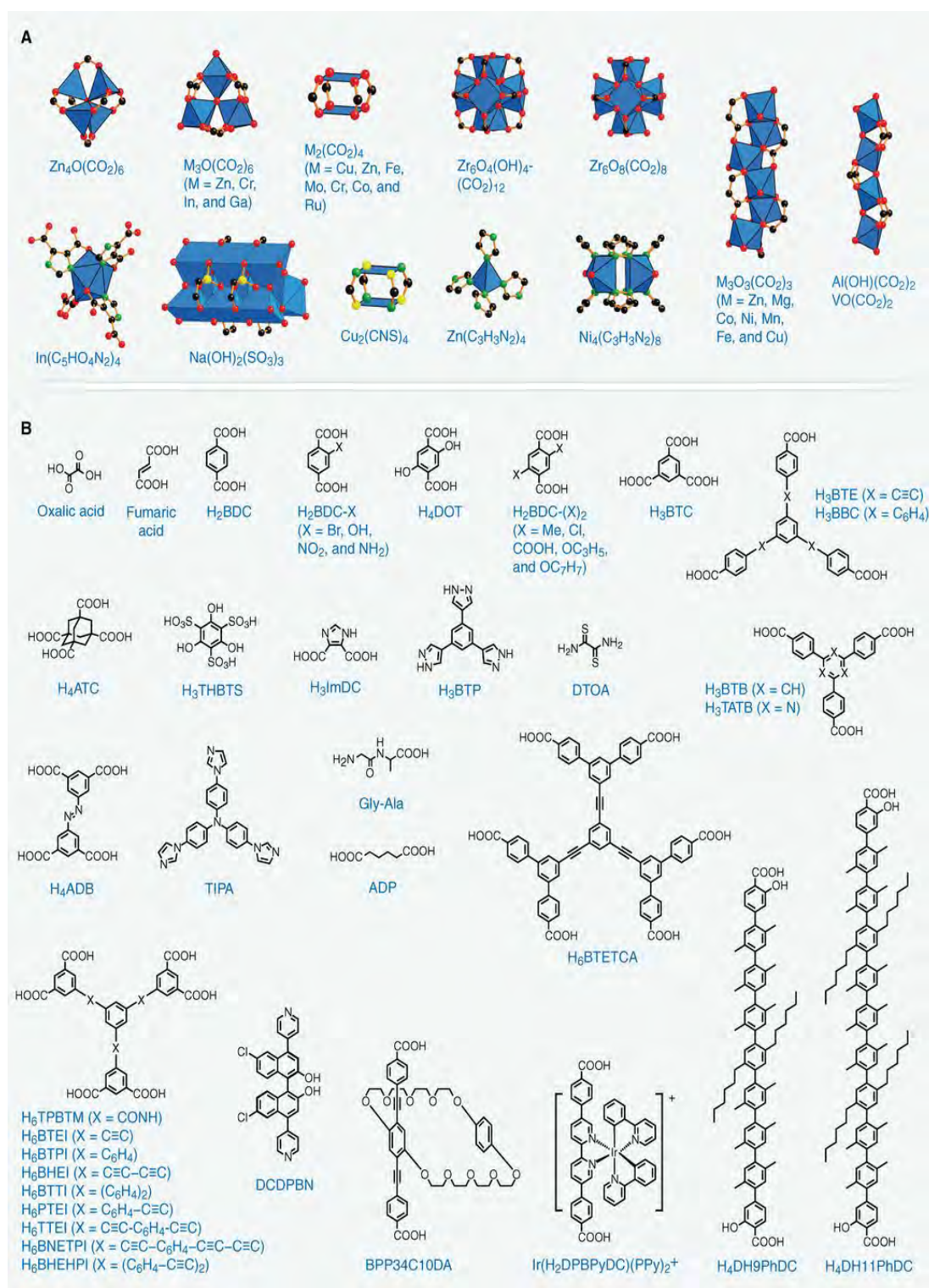


FIGURE 2.12: Inorganic secondary building units (A) and organic linkers (B). Color code: black, C; red, O; green, N; yellow, S; purple, P; light green, Cl; blue polyhedra, metal ions. Hydrogen atoms are omitted for clarity. AIPA, tris(4-(1H-imidazol-1-yl)phenyl)amine; ADP, adipic acid; TTFTB4, 4,4,4,4-[(2,2-bis(1,3-dithiolylidene))-4,4,5,5-tetrayl]tetrabenzoate [75].

Removal of harmful materials from contaminated water is very important because water quality is adversely influenced by them. However, so far, there has been a few reports on the use of MOFs in the removal of harmful materials [78–82].

Zeolites, specially ZIF-8 (Zeolitic Imidazolate Framework) thin film, are capable for desalination. However ZIF-8 has a rigid framework and it is not flexible enough to have a higher uptake of salts in the water. For example, a molecular simulation showed that ZIF-8 is resistant to water and organic solvents, because of hydrophobic pores [83, 84]. The paper highlighted that desalination can occur under external pressure, which includes Na^+ and Cl^- ions being unable to pass through the thin film due to a molecular sieving effect. In this study there was an assumption that the thin film material was entirely defect free. So, the increasing interest in utilizing new materials has led to a surge of interest in preparing MOF thin films as selective thin films for water purification.

MIL- group (Materials Institute Lavoisier) MOFs have shown promising results in removal of toxic and even carcinogenic dye materials from aqueous solution. For example, MIL-101-Cr (chromium terephthalate-based mesoscopic metalorganic framework) has been identified for the removal of both methyl orange (MO) and xylenol orange due to its excellent adsorption properties [85, 86]. Also, MIL-101-Cr and MIL-100-Fe MOFs have been used for liquid phase adsorptive removal of naproxen and clofibrac acid, two typical PPCPs (pharmaceuticals and personal care products) [87, 88]. Furthermore, MIL-100-Al gels have been used for high efficiency removal of microcystin-LR in 2013 [89].

The use of MOF-235 (Iron terephthalate) has also shown promise for the removal of methyl orange (MO), as well as methylene blue (MB) through electrostatic interactions

between the dyes and the adsorbent [90].

In another study n-hexane, cyclohexane, benzene, toluene, and p-xylene showed reversible adsorption in FMOF-1 (a fluorinated MOF) with no detectable water adsorption even at near 100% relative humidity due to MOF's high capacity and affinity to C₆-C₈ hydrocarbons. In comparison with FMOF-1, FMOF-2, obtained from the annealing of FMOF-1, showed double the amount of toluene adsorption due to having enlarged cages and channels [91].

Bisphenol-A was removed from aqueous solution by MIL-53-Cr(Benzenedicarboxylate) [92] and MIL-101-Cr and MIL-100-Fe [93]. Results showed that the addition of different amount of NaCl lead to BPA adsorption into MIL-101-Cr pore through free diffusion and MIL-100-Fe adsorbed BPA with electrostatic interaction. The adsorption capacity and adsorption kinetic constant of MIL-101-Cr were greater than those of MIL-100-Fe which proved the importance of porosity and pore size for adsorption.

Several toxic chemicals (NH₃, H₂S and CNCl) were reported to remove by Zr(OH)₄/HKUST-1 composites from effluent water. In all, materials exhibited good broad spectrum removal capabilities. The NH₃ performance of the composites were substantially higher than a broad spectrum carbon, while CNCl and H₂S removal capacities were slightly lower than those of the broad spectrum carbon [94].

Also in another study some heavy-metal ions including Cd(II), Co(II), Cr(III), Cu(II) and Pb(II) were studied to remove by TMU-4, TMU-5 and TMU-6 (Azine-Decorated Zinc(II) MOFs) in water [95].

UiO-66 was also used in water treatment. By using an *in situ* solvothermal synthesis method, the pure-phase Zr-MOF polycrystalline thin films were fabricated on alumina hollow fibers. Because of the exceptional chemical stability of UiO-66 material the thin films had very stable water filtration performance. These thin films exhibited high multivalent ion rejection (86.3% for Ca^{2+} , 98% for Mg^{2+} , and 99.3% for Al^{3+}) on the basis of size-exclusion mechanisms with moderate permeance ($0.14 \text{ Lm}^{-2}\text{h}^{-1}\text{bar}^{-1}$) and good permeability ($0.28 \text{ Lm}^{-2}\text{h}^{-1}\text{bar}^{-1}\mu$) for water desalination. These promising results shows the UiO-66 thin film as a promising candidate for water desalination [96]. In another study the AgI/UiO-66 composites with different composition ratios were synthesized by a simple solution method and exhibited remarkable activity for the degradation of Rhodamine-B (RhB) under visible-light irradiation [97]. Due to the strong interaction between polar phenols and the aqueous matrix, effective solid-phase microextraction of polar phenols from water samples is usually difficult. But by fabrication of a UiO-66 coated stainless steel fiber via physical adhesion, the detection limits ranged from $0.11 \mu\text{gL}^{-1}$ for 2,6-dimethylphenol to $1.23 \mu\text{gL}^{-1}$ for phenol [98]. In other studies, UiO-66 was incorporated with bismuth tungstate (Bi_2WO_6) and BiOBr by a simple hydrothermal method for the development of visible-light photocatalysts. These composites not only exhibited enhanced photocatalytic activity for the degradation of Rhodamine-B (RhB) under visible-light irradiation, but also showed good catalyst stability during long exposure to light [99, 100]. Highly dispersed Pd nanoparticles of about 36 nm in diameter were immobilized in UiO-66-NH₂ via a hydrothermal method. Results showed that the Pd@UiO-66-NH₂ exhibited excellent reusability and much higher catalytic performance than UiO-66-NH₂ for reduction of aqueous Cr(VI) under visible light illumination [101].

2.4.2 MOFs as Drug Delivery Vehicles

MOFs are one of the most promising candidates for drug delivery. Their unprecedented internal surface areas, uniform pore sizes and chemical versatility make them an attractive alternative to conventional nanocarriers for drug delivery and for imaging contrast agent applications [5, 102]. Thus far, several studies have shown that nontoxic MOFs can be used as efficient nanocarriers for a large variety of therapeutic agents.

In 2010, Horcajada and co-workers showed that iron carboxylate nanoparticle MOFs can adsorb and release anticancer and antiviral drugs [6]. In this study, Busulfan was encapsulated into the framework using an impregnation method thereby loading up to 25 wt%. These frameworks lead to a retarded release over 7 days which had the additional benefit of avoiding the normal biodegradation of the drug.

More recently, Lin et al. [7] reported the encapsulation of Cisplatin and siRNA into UiO-66 nanoparticles using aminotriphenyldicarboxylic acid (amino-TPDC) as a bridging ligand. After 2 h of incubation the active siRNA was able to escape from the endo/lysosome entrapment of the siRNA/UiO-Cis. The results showed that the resistant ovarian cancer cells resensitized after being treated with siRNA/UiO-Cis and increased the in vitro chemotherapeutic efficacy.

In another study [103], Zr-based MOF of UiO-66 was applied as an efficient carrier for amino-bisphosphonate of alendronate (AL) delivery. The AL is widely used for the treatment of osteoporosis, solid tumour bone metastases and myeloma bone disease. The inherent Zr-O clusters in UiO-66 serve as natural drug anchorages for effective capture of AL, leading to an enhanced loading capacity and its mediated release. Also,

the pH-sensitive drugcarrier interaction accelerates the AL release in the acidic milieu of cancer cells, resulting in increased antitumour efficiency against cell lines.

Ferey and co-workers studied the storage and release of Ibuprofen with chromium-based MIL-101, MIL-100, MIL-53 and the less toxic MIL-53(Fe) [104, 105]. MIL-101 and MIL-100 showed high Ibuprofen loading, with $0.347 \text{ g-Ibuprofen/g-MOF}$ for MIL-100 and $1.376 \text{ g-Ibuprofen/g-MOF}$ for MIL-101 while MIL-53(Cr) and MIL-53(Fe) achieved loadings of $0.220 \text{ g-Ibuprofen/g-MOF}$ and $0.210 \text{ g-Ibuprofen/g-MOF}$ respectively. The kinetics of Ibuprofen release was investigated by suspending the Ibuprofen-loaded materials in simulated body fluid at 37 °C. There was an initial release of weakly-bound drug molecules within the first 2 h for MIL-100, and the entire cargo is released within 3 days. For MIL-101, steady release is observed for the first 8 h with complete release after 6 days. In the case of MIL-53, complete drug delivery occurred in 3 weeks, a long release time attributed to the flexibility of the MIL-53 framework and the strong drug-framework interactions. However, these MOFs contain toxic chromium, and thus the use of these materials for drug delivery should be limited.

2.4.3 MOFs Toxicity Studies

Several toxicity studies of MOFs in various cell lines reported the biodegradable character of specific MOFs showing that iron and zirconium based MOFs generally show lower toxicity than cobalt, magnesium and copper based MOFs [103, 106–110].

2.5 Summary

This chapter highlighted findings from the literature review on nanoporous materials conducted as part of the first stage of the research framework. The findings supported the view of the global initiative on water quality sensing and drug delivery. However, to date, existing optical fibre chemical sensors and actuators appear to be deficient in dealing with various contaminants in the water and drug delivery respectively. To overcome the barriers, there is a need to identify new thin films (MOFs) for water quality sensing and simultaneously for drug storage and release.

Chapter 3

Experimental Instruments and Methods

Four general categories of experimental instruments and methods have been used in this thesis:

Firstly, standard chemical characterisation techniques that included: Thermo Gravitric Analysis (TGA), X-Ray Diffraction (XRD) and Gas Adsorption Analysis.

Secondly, techniques associated with thin film deposition and characterization were deployed. These included: Radio Frequency Glow Discharge (RFGD) Plasma Polymerisation, Scanning Electron Microscopy (SEM), Fourier Transform Infrared Spectroscopy (FTIR) and Energy-Dispersive X-Ray Spectroscopy (EDX).

Thirdly, for biological applications, a Microplate Photometer was used for absorbance detection of 5-Fluorouracil in a liquid.

Finally, the optical components and the experimental method to determine optical cavity lengths, obtained via FPI, and used in the detection of contaminants in water, are presented.

3.1 Standard Chemical Characterisation Techniques

3.1.1 Thermogravimetric Analysis (TGA)

Thermogravimetric analysis (TGA) is a method of thermal analysis in which changes in the physical and chemical properties of materials are measured as a function of increasing temperature.

TGA is commonly used to determine selected characteristics of materials that exhibit either mass loss or gain due to decomposition, oxidation, or loss of volatiles (such as moisture). Common applications of TGA are (1) materials characterization through analysis of characteristic decomposition patterns, (2) studies of degradation mechanisms and reaction kinetics, (3) determination of organic content in a sample, and (4) conformation of inorganic content in a sample, that could be useful to predict material structure.

Thermogravimetric analysis (TGA) relies on a high degree of precision in three measurements: mass change, temperature, and temperature change. Therefore, the basic instrumental requirements for TGA are a precision balance with a pan loaded with the sample, and a programmable furnace. The furnace can be programmed either for a constant heating rate, or for heating to acquire a constant mass loss with time.

The TGA instrument continuously weighs a sample as it is heated to temperatures of up to 700 °C. As the temperature increases, various components of the sample are decomposed and the weight percentage of each resulting mass change can be measured. Results are plotted with temperature on the X-axis and mass loss on the Y-axis. The data can be adjusted using curve smoothing and first derivatives are often also plotted to determine points of inflection for more in-depth interpretations

3.1.1.1 TGA Instrumentation

TGA analysis data were obtained with the use of a “PerkinElmer Pyris 1 TGA” shown in Figure 3.1. The temperature went up to 700 °C for all samples in order to compare weight loss in them.



FIGURE 3.1: Thermogravimetric Analysis Instrument

3.1.2 X-Ray Diffraction (XRD)

3.1.2.1 Fundamental Principles of X-ray Diffraction (XRD)

X-ray diffraction is now a common technique for the study of crystal structures and atomic spacing. X-ray diffraction is based on constructive interference of monochromatic X-rays and a crystalline sample. These X-rays are generated by a Al anode ray tube, filtered to produce monochromatic radiation, collimated to concentrate, and directed toward the sample. The interaction of the incident rays with the sample produces constructive interference (and a diffracted ray) when conditions satisfy Bragg's Law, as illustrated in Figure 3.2.

$$n\lambda = 2d\sin\theta \quad (\text{Eqn. 3.1})$$

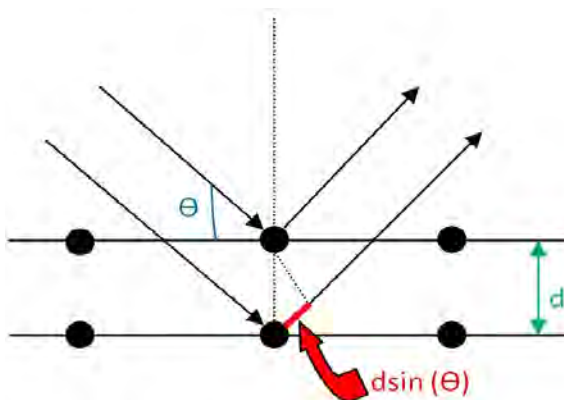


FIGURE 3.2: Crystal diffraction illustrating Bragg's Law

This law relates the wavelength of electromagnetic radiation (λ) to the diffraction angle (θ) and the lattice spacing (d) in a crystalline sample. These diffracted X-rays are then detected, processed and counted. By scanning the sample through a range of

2θ -angles, all possible diffraction directions of the lattice should be attained due to the random orientation of the powdered material.

3.1.2.2 XRD Instrumentation

Where possible, samples were back-loaded into sample holders prior to the collection of XRD traces. Where insufficient sample was provided to allow for back-loading, samples were loaded onto a zero background plate. A “Bruker D8 Advance X-Ray Diffractometer” operating under $\text{CuK}\alpha$ radiation (40 kV, 40 mA) equipped with a Lynx-Eye detector was employed to obtain the XRD patterns. The samples were scanned over the 2θ range 5° to 130° with a step size of 0.02° and a count time of 1.6 second per step. 173/192 of the sensor strips on the LynxEye detector were used, to give an equivalent count time of 276.8 seconds per step. Analyses were performed on the collected XRD data using the Bruker XRD search match program EVATM.

Pawley analyses were performed on the data using the Bruker TOPASTM V5 program. Background signals were described using a combination of Chebyshev polynomial linear interpolation function and $1/x$ function. Cell parameters, vertical sample displacement, peak full width at half maximum and peak scale factors were all refined. Error values were calculated on the basis of three estimated standard deviations.

3.1.3 Gas Adsorption Analysis

The process of adsorption is usually studied through graphs known as adsorption isotherms. It is the graph between the amounts of adsorbate (x) adsorbed on the surface of adsorbent (m) and pressure at constant temperature.

The adsorption theory put forward by Brunauer, Emmett and Teller (BET) explained that multilayer formation is the true picture of physical adsorption in mesoporous materials. One of the basic assumptions of Langmuir adsorption was that adsorbates form a monolayer. The Langmuir adsorption equation can be applicable at very low partial pressures. Under these conditions, gaseous molecules would possess high thermal energy and high escape velocity. As a result of this, fewer gaseous molecules would be available near the surface of the adsorbent. At higher partial pressures, the thermal energy of gaseous molecules decreases and more and more gaseous molecules would be available per unit surface area. Due to this, multilayer adsorption would occur. The multilayer formation was explained by BET Theory. The BET equation is given as

$$V_{Total} = \frac{V_{mono}C\left(\frac{P}{P_0}\right)}{\left(1 - \frac{P}{P_0}\right)\left(1 + C\left(\frac{P}{P_0}\right) - \frac{P}{P_0}\right)} \quad (\text{Eqn. 3.2})$$

where V_{mono} be the adsorbed volume of gas at high pressure conditions so as to cover the surface with a unilayer of gaseous molecules, $\frac{K_1}{K_L}$ is designated as C . K_1 is the equilibrium constant when single molecule adsorbed per vacant site and K_L is the equilibrium constant to the saturated vapour liquid equilibrium.

3.1.3.1 Gas Adsorption Instrumentation

Surface area and pore size distribution measurements were obtained by use of “Micromeritics ASAP 2420 Accelerated Surface Area and Porosimetry System” and is shown in Figure 3.3. Standard features include six independently operated analysis ports and a programmable and fully automated sample preparation module with twelve independently operated ports that allow users to prepare up to twelve samples simultaneously. The sample degas procedure is controlled by software and allows to specify parameters for custom degas and sample preparation. User defined evacuation rates and temperature ramps are provided to support even the most difficult-to-prepare samples. Usually non corrosive gases like nitrogen, hydrogen, argon and carbon dioxide are used as adsorbates to determine the surface area data.



FIGURE 3.3: Micromeritics ASAP 2420 Accelerated Surface Area and Porosimetry System

3.2 Thin Film Deposition and Characterization

3.2.1 Radio Frequency Glow Discharge (RFGD) Plasma Polymerisation

Radio frequency glow discharge (RFGD) plasma polymerisation is a technique that is used to deposit thin polymer layers over a surface to influence its physical and chemical properties. In this process an electrical potential difference is applied between two copper electrodes in the presence of an organic monomer vapour under low pressure. Applying a continuous radiofrequency AC voltage across the electrodes causes the monomer vapour to become a plasma which then polymerises and coats the surface. Traditionally, this technique is utilised to control the interactions and binding of proteins to surfaces without requiring the protein itself to be present in the surface modification process, but has also been shown to be able to produce a platform for secondary functionalisations. Due to the adaptable and non-destructive nature of RFGD polymerisation and its ease of application, it provides a simple and quick process by which to alter the surface chemistry of a substrate beyond its traditional applications.

3.2.1.1 RFGD Polymerisation Instrumentation

Prior to the MOF thin film deposition, a plasma polymer film produced from the monomer diethylene glycol dimethyl ether (diglyme 99.5%, Sigma-Aldrich) was deposited at the tip of conventional single mode optical fibre (SMF-28) using a Radio Frequency Glow Discharge (RFGD) plasma polymerization. Plasma treatments were performed using

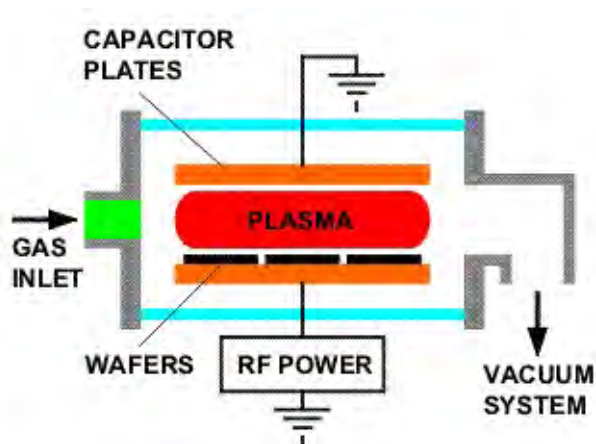


FIGURE 3.4: Schematic of RFGD polymerisation reactor

a custom-built reactor (Figure 3.5) described elsewhere. The parameters chosen for plasma polymer deposition of the diglyme film were: frequency of 200 kHz, load power of 20 W, initial monomer pressure of 20 Pa and treatment time of 30 s. The diglyme plasma polymer coating was performed in a chamber when the pressure gauge read below 0.001 mbar. The optical fibre samples were placed within the reactor on the lower electrode. After plasma treatment, optical fibres were rounded over a Teflon rod and Teflon tape was wrapped over the remaining polymer coating to avoid contact with the UiO-66 MOF solution.

3.2.2 Scanning Electron Microscopy (SEM)

A scanning electron microscope (SEM) uses a focused beam of high-energy electrons to generate a variety of signals at the surface of solid specimens. The signals that derive from electron-sample interactions reveal information about the sample including external morphology (texture), chemical composition, and crystalline structure. A scanning electron microscope (SEM) produces images of a sample by scanning it with a focused beam of electrons.



FIGURE 3.5: RFGD plasma polymerization system

3.2.2.1 SEM Instrumentation

SEM for this study was done using two different instruments: the “JCM-5000 Neo-Scope Table Top SEM (JEOL Ltd. Japan)” and “FEI/Philips XL30 FEG ESEM”. Samples were sputter-coated using a “Neo Coater MP-19090 NCTR” (Jeol Ltd. Japan), equipped with a DC magnetron for gold coating, and “SC5750 Quorum Technologies Ltd.” sputter coater for irridium coating in order to prevent problems with charging. Optical fibres and powders were mounted on the side and surface of an aluminium sample holder using carbon tape. In most cases, an electron acceleration of 10 kV was used for imaging.

3.2.3 Fourier Transform Infrared Spectroscopy (FTIR)

FTIR spectroscopy is a well-established method for the chemical identification of particles or contaminants and for visualizing the distribution of certain substances in complex compounds. For this purpose, microscopes having mirror optics have been developed that allow not just a visual viewing but also for infrared spectroscopic analysis of a sample.

3.2.3.1 FTIR Instrumentation

In this study a “Thermo Scientific Nicolet 6700 Spectrometer”, depicted in Figure 3.6, was used for determining whether 5-Fluorouracil has been successfully encapsulated in UiO-66 powder. The number of scans collected to produce a spectrum was 32.



FIGURE 3.6: FTIR Microscopy device

3.2.4 Energy-Dispersive X-Ray Spectroscopy (EDX)

Energy Dispersive X-ray Spectroscopy (EDX) is a qualitative and quantitative X-ray microanalytical technique that can provide information on the chemical composition of a sample for elements. An electron beam is focussed on the sample in a scanning electron microscope (SEM). The electrons from the primary beam penetrate the sample

and interact with the atoms from which it is made. The X-rays are detected by an Energy Dispersive detector which displays the signal as a spectrum. The energies of the characteristic X-rays allow the elements making up the sample to be identified, while the intensities of the characteristic X-ray peaks allow the concentrations of the elements to be quantified.

3.2.4.1 EDX Instrumentation

In our reserach a “FEI/Philips XL30 FEG ESEM”, with Electron Backscatter Diffraction analysis and Energy-Dispersive X-ray capability device was used for analysing the UiO-66 powder and thin film.

3.3 Biological Applications

3.3.1 Microplate Photometer

Plate readers, also known as microplate readers or microplate photometers, are instruments which are used to detect biological, chemical or physical events of samples in microtiter plates. They are widely used in research, drug discovery, bioassay validation, quality control and manufacturing processes in the pharmaceutical and biotechnological industry and academic organizations. A light source illuminates the sample using a specific wavelength (selected by an optical filter, or a monochromator), and a light detector located on the other side of the well measures how much of the initial light is

transmitted through the sample; the amount of transmitted light will typically be related to the concentration of the molecule of interest.

3.3.1.1 Microplate Photometer Instrumentation

The “FlexStation 3 Microplate Reader” (Molecular Devices, LLC.) shown in Figure 3.7 was used in this research for absorbance studies. This device features high-efficiency monochromator optics which are tunable for absorbance, fluorescence intensity, fluorescence polarization, and time-resolved fluorescence assays. Users have several choices when configuring the FlexStation 3 Microplate Reader. Users can choose from 96-well pipetting, 384-well pipetting, or both.



FIGURE 3.7: FlexStation 3 Microplate Photometer

3.3.1.2 Microplate Photometer Calibration Curve for 5-Fluorouracil

Prior to use light source, the sensitivity of Microplate Photometer was determined by making diluted solutions of 5-Fluorouracil in water at 37 °C and its calibration curve is graphed in Figure 3.8.

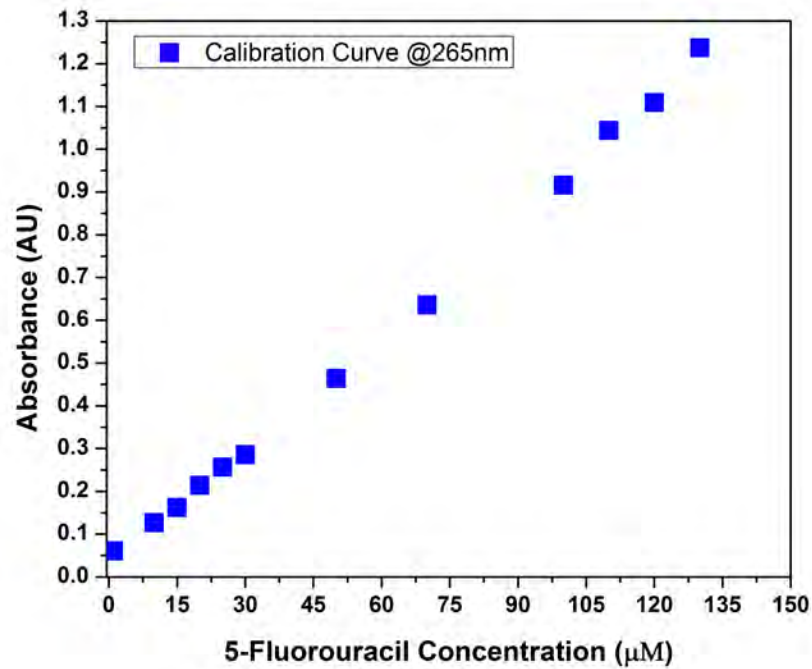


FIGURE 3.8: Microplate Photometer calibration curve for 5-Fluorouracil

3.4 Optical Components

3.4.1 Optical Fibres

Two types of silica optical fibres were used in this study. The specifications of each are as follows:

SMF-28 (Corning Optical Communications, USA): standard telecommunication fibre with core and cladding diameter of $8.2 \mu\text{m}$ and $125 \pm 0.7 \mu\text{m}$ respectively, cut-off wavelength $< 1260 \text{ nm}$ and numerical aperture of 0.14.

SM-800 (Thorlabs, Inc.): core and cladding diameter of $5.6 \mu\text{m}$ and $125 \pm 1.0 \mu\text{m}$ respectively, cut-off wavelength of 660-800 nm and numerical aperture of 0.10-0.14.

3.4.1.1 Fibre Couplers

Fibre optic couplers are optical fibre devices that divide one input between two or more outputs, or combine two or more inputs into one output. The device allows the transmission of light waves through multiple paths. Optical couplers can be specified by the number of ports used for signal transmissions going in as well as out. The coupling ratio (splitting ratio) is the distribution of power among the output fibres of a coupler. A coupling ratio of 50/50 means that there is an equal distribution of optical power; a 60/40 ratio means 60% of the power is transmitted to a primary output and 40% to the secondary output. 1×2 and 2×2 couplers are available with coupling ratios of 50/50 (3 dB) and 10/90 (10%). Wavelength choices for fibre optic couplers include 633 nm, 830 nm, 1060 nm, 1300 nm, and 1550 nm (centre wavelength) and a typical coupler is shown in Figure 3.9.

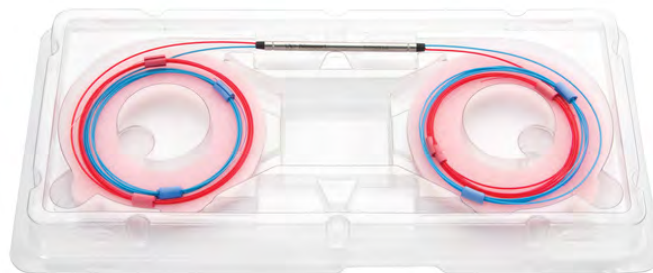


FIGURE 3.9: A 2×2 Fibre Coupler

In this study, where needed, two 2×2 single mode fibre couplers (OEMarket, Australia) with different centre wavelengths (830 and 1550 nm) have been used.

3.4.2 Light Sources

3.4.2.1 Superluminescent Light Emitting Diode (SLED)

A superluminescent light emitting diode operates very similar to a laser diode. It is composed of an electrically driven p-n junction that, when biased in the forward direction, becomes optically active and generates amplified spontaneous emission over a wide range of wavelengths. The peak wavelength and the intensity of the SLED depends on the active material composition and on the injection current level.

Two fibre coupled superluminescent diodes, “2 mW @ 790 nm: QSDM-790-2” (Figure 3.10) and “1.5 mW @ 1050nm: QSDM-1050-2” from QPhotonics, LLC. were used in this thesis where light in near and far-infrared was needed. These SLEDs are high power and have broad spectral width, flat and low-rippled spectrum.

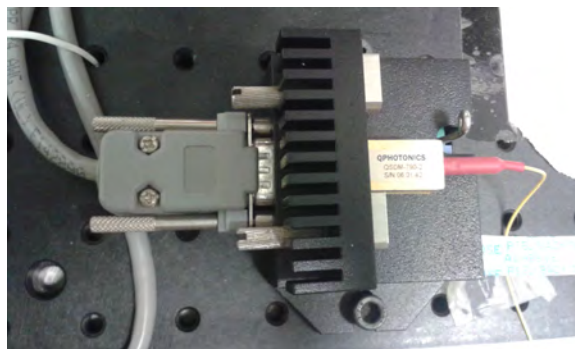


FIGURE 3.10: Fibre coupled superluminescent diode, QSDM-790-2

3.4.2.2 Erbium ASE Light Source

Amplified Spontaneous Emission (ASE) is a process where spontaneously emitted radiation (luminescence) is amplified. If a laser has a medium large gain, the luminescence

from spontaneous emission can be amplified to high power levels. In applications where light with low temporal coherence but good spatial coherence is required, this amplified luminescence can be used. The light produced is typically a hundred times stronger than an Edge-Emitting LED (ELED), and ten thousand times stronger than a white light source [111].

The “Agilent 83438A Erbium ASE” source which emits light from an erbium doped fibre over the range from 1500-1600 nm, was used in this study and is shown in Figure 3.11.



FIGURE 3.11: Erbium ASE Source

3.4.3 Optical Spectrum Analyzer (OSA)

An optical spectrum analyzer is an instrument which is designed to display the distribution of optical power over a specified wavelength window. An OSA displays power in the vertical scale and the wavelength in the horizontal scale.

The optical spectrum analyzer which has been used in this thesis is: “Ando, AQ6317B” which has high wavelength accuracy, high wavelength resolution of 0.015 nm, synchronous sweep, wide band, high sensitivity and high power measurement capabilities.



FIGURE 3.12: Ando AQ6317B OSA

3.4.4 Signal Processing Method

Experimental signals do not exist without noise; i.e. noise interferes or corrupts signals in a significant manner and these must be removed from the data in order to proceed with further data analysis. Thus signals from FPI (Fabry-Perot interference) includes Fresnel reflections [112].

The algorithm in this study for FPI is written based on the work in [48, 113–115]. The output signals collected by an OSA need to be denoised first and then demodulated to get the optical path difference. A measured sensor signal arising from a FPI depends upon the source spectrum. To eliminate the unwanted source spectrum modulation, interferograms were “normalized” using the reflection spectrum from a cleaved fibre end-face, taken prior to splicing the sensor to the system (i.e. each sensor spectrum was divided by its source spectrum), for which an example is shown as $I_1(\lambda)$ in Figure 3.13 (actual data to be presented in Chapter 5).

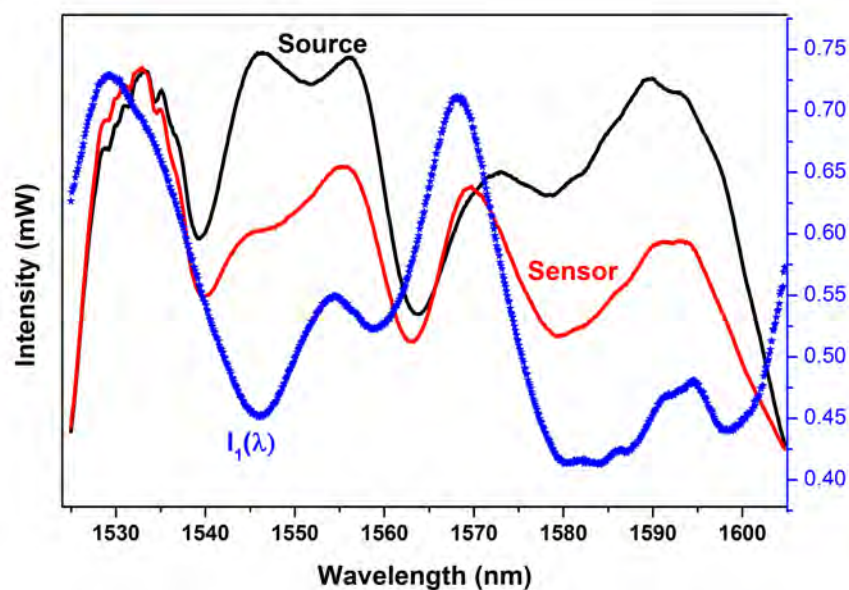


FIGURE 3.13: Example of a measured source and sensor and deduced $I_1(\lambda)$ spectra

For calculating the optical path difference, $n \times d$, an algorithm was run using Matlab software in which the first part of the program denoises the spectrum by using Daubechies Wavelet Transform (DWT) [116, 117]. The DWT filter is usually utilized as a band-pass filter and is used to decompose the spectrum signal for denoising. For the low finesse FPI sensors, the spectrum interferogram with noise has the following general form:

$$I_1(\lambda) = A(\lambda) + B(\lambda) \times \cos\left(\frac{4\pi nd}{\lambda} + \varphi\right) + N(\lambda) \quad (\text{Eqn. 3.3})$$

where λ is the scanning wavelength, $A(\lambda)$ is the low frequency background irradiance that is introduced by the light source, $B(\lambda)$ is the coherence envelope of the sensor spectrum that is relevant to the fibre bending, the coupling ratio and the contrast influenced by the reflection of the fibre ends, $N(\lambda)$ is the high frequency intensity noise of the broadband source, the constant φ is the wave loss from the reflection at the thin film interface and $n \times d$ is the optical path difference.

With running a seven level Daubechies wavelet, db-7, the sensor signal is decomposed into a set of approximations and details at different levels. The approximations are the low frequency components of the signal and the details are the high frequency components. The approximation of level seven and the detail of level one are subtracted from the sensor spectrum for eliminating $A(\lambda)$ and $N(\lambda)$ respectively. The approximation of levels 2 to 5 are also subtracted to further smooth the output spectrum ($I_2(\lambda)$ in Eqn. 3.4). Figure 3.14 shows an example of these sequences .

$$I_2(\lambda) = B(\lambda) \times \cos\left(\frac{4\pi nd}{\lambda} + \varphi\right) \quad (\text{Eqn. 3.4})$$

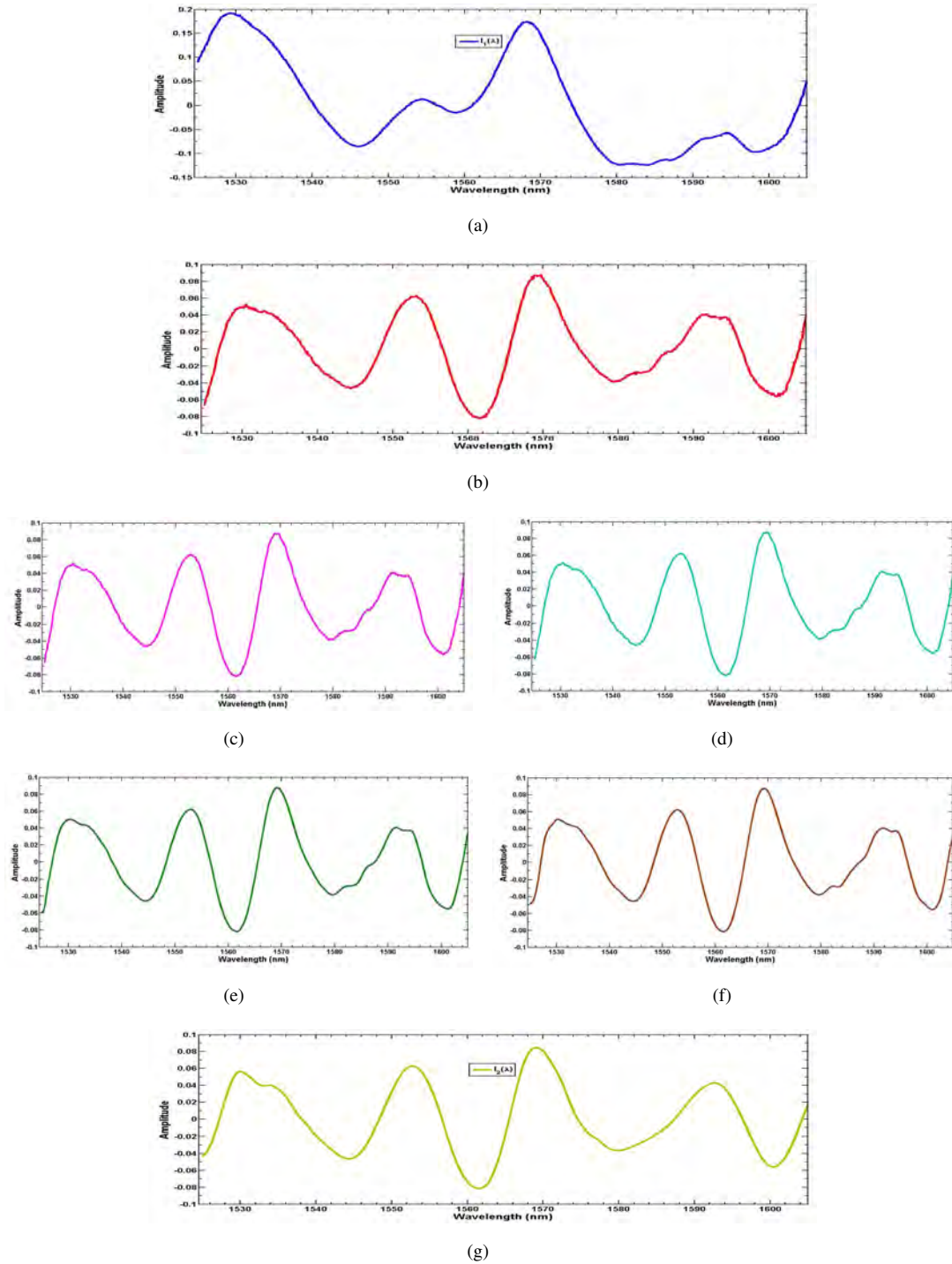


FIGURE 3.14: Example of: a) $I_1(\lambda)$ spectrum (as in Figure 3.13). b) after subtracting $A(\lambda)$ (approximation level 7). c) after subtracting $N(\lambda)$ (approximation level 1). d, e and f: after smoothing (approximation levels 2, 3 and 4), g: $I_2(\lambda)$ spectrum.

$I_2(\lambda)$ in Eqn. 3.4, can be regarded as an amplitude and frequency modulated (AM-FM) signal with $B(\lambda)$ being the instantaneous amplitude. Thus, the second part of the algorithm does a Fast Fourier Transform (FFT) [118] to first eliminate $B(\lambda)$ and then determine the optical path difference from the extracted periodicity. The resultant signal after eliminating $B(\lambda)$ is given in Eqn. 3.5 and the deduced FPI spectrum ($I_3(\lambda)$) is shown in Figure 3.15 in comparison with the initial source and sensor spectra.

$$I_3(\lambda) = \cos\left(\frac{4\pi nd}{\lambda} + \varphi\right) \quad (\text{Eqn. 3.5})$$

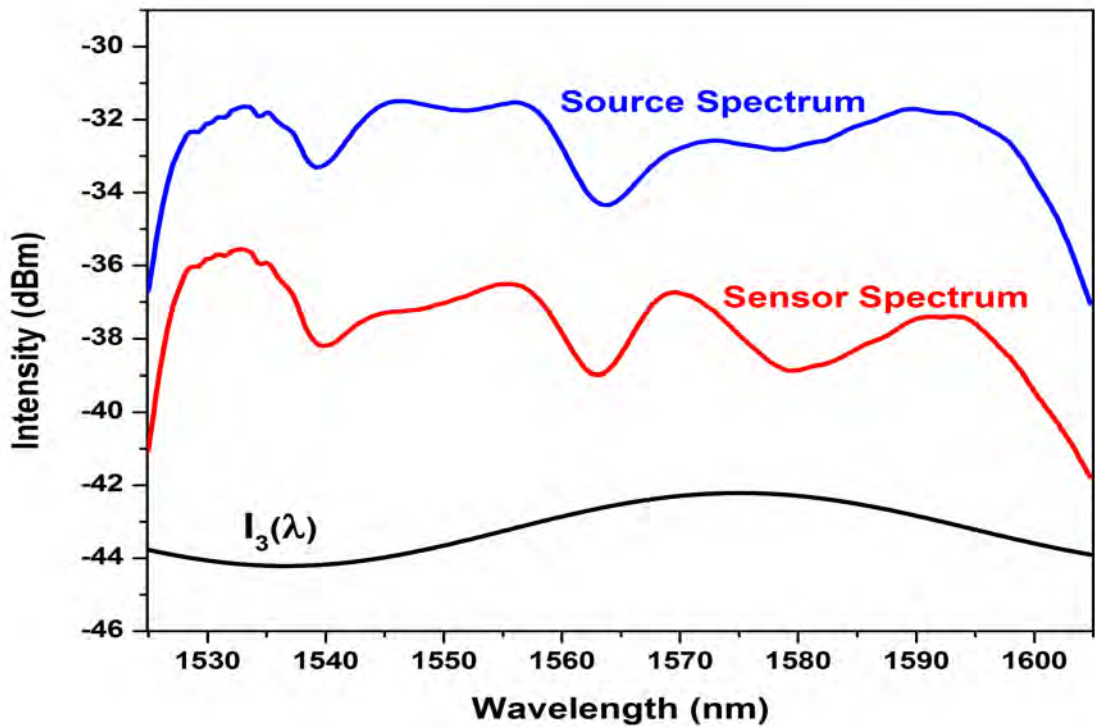


FIGURE 3.15: Example of a measured source and sensor and deduced FPI spectra ($I_3(\lambda)$).

The Matlab algorithm is provided in Appendix A.

3.5 Summary

In this chapter, the wide range of experimental equipment used in this study were described. As FPI was used for most sensors, the mathematical procedure to obtain the optical path difference was also provided. The experimental apparatus for the end-face sensor characterization is schematically shown in Figure 3.16.

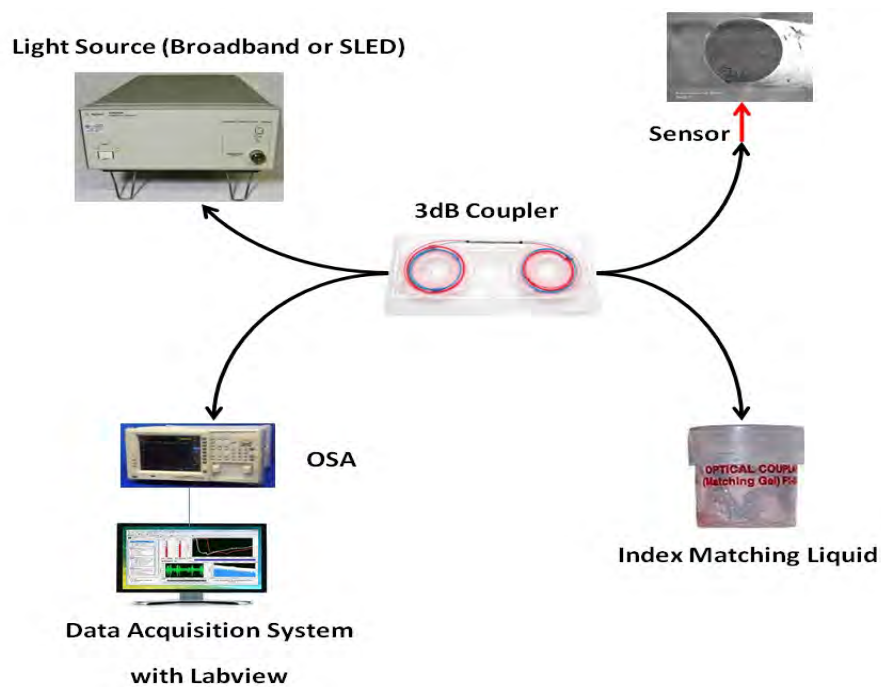


FIGURE 3.16: Schematic diagram of the optical fibre interferometric measurement system

Chapter 4

Zeolite Coated Optical Fibre for Aqueous Contaminant Detection

This chapter presents the characterization, development and optimization of the zeolite based optical fibre chemical sensor for trace contaminant detection in aqueous media. As discussed in Chapter 2, zeolite based optical fibre thin films have been used widely in water sensing area both in gas and liquid phase [69–73]. Here, a zeolite thin film optical fibre is fabricated and used to detect specific contaminants in water down to ppm and ppb levels.

4.1 The Principles of the Sensor

As discussed in Section 2.3, the zeolite film is used to control molecular transport, allowing certain molecular species to pass through while rejecting others based on the molecular size, chemical properties and chemical bonding properties with zeolite.

The working function of the sensor is based on the change of optical thickness (corresponding change in refractive index) induced within zeolite membrane. The sensor design is based on using Fabry-Perot Interferometry technique described in Section 2.2.2.

As it can be seen in Figure 4.1, the end-face coated reflective zeolite thin film will absorb contaminants from water. Then upon adsorption of these contaminants, its refractive index will change, and as explained in Section 2.2.2, an interference pattern will be generated. The optical spectrum analyzer (OSA) will record the interference pattern (Figure 3.16) and by using the signal processing method (described in Section 3.4.4), the optical path difference will be determined. This is then correlated to the amount of adsorbed contaminant which is in proportion to its presence in the sensor's environment.

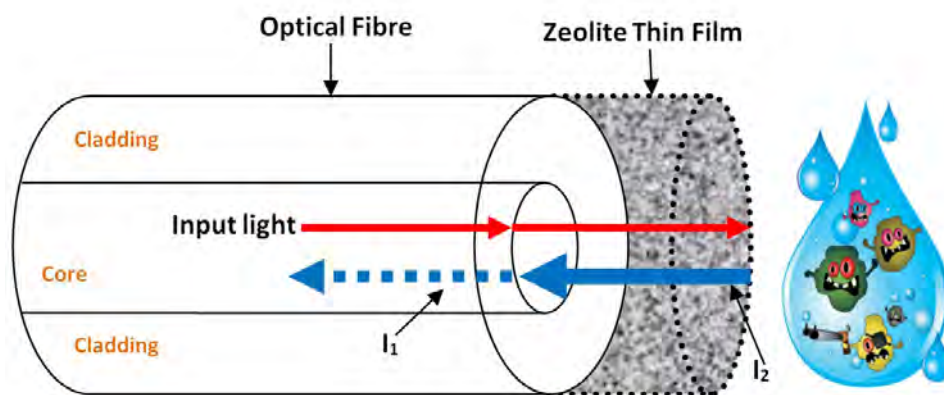


FIGURE 4.1: Structure of the end-face zeolite reflective sensor

4.2 Synthesis of Zeolite Thin Film on Optical Fibre

The procedure for zeolite film growth has been described in a paper by Zhang et al. [70], which has been adapted to coat the end-face of the optical fibre. A standard SMF-28 optical fibre with 125 μm cladding and a 9 μm core was cleaved at a right angle to its axis to

produce the end-face, and was cleaned with acetone. The fibre was mounted in a synthesis tube with its cleaved end suspended in the zeolite synthesis solution and the end-face facing upward. The synthesis solution was made by mixing 30 ml of water, 5.65 ml of tetrapropyl ammonium hydroxide (TPAOH, Sigma-Aldrich), and 10.2 ml of tetraethyl orthosilicate (TEOS, Sigma-Aldrich) (the structure directing agent, tetrapropyl ammonium (TPA)⁺, occupies the zeolite channels during crystallization). The mixture was under constant stirring at 50 °C for 2 h and then aged at room temperature for 4 hours. The thin film was first grown on the end-face of the fibre by *in situ* crystallization at 180 °C under autogenous pressure for 4 h and secondly by replacing the initial mixture with a fresh one for another 4 h to increase the membrane thickness. After the hydrothermal synthesis, the fibre was rinsed with deionized water, dried under vacuum at 80 °C overnight and calcined at 120 °C for two hours. For further analysis, the zeolite powder was rinsed in water and collected by centrifuging at 6000 rpm for 5 min.

4.3 Zeolite Material and Optical Fibre Coating Characterization

XRD and SEM were carried out on zeolite powder and zeolite coated optical fibre to check the crystallinity and morphology of the particles. XRD of the zeolite powder is shown in Figure 4.2, while SEM images of the optical fibre coating and zeolite powder are shown in Figures 4.3 and 4.4 respectively.

As shown by XRD, a single crystalline phase of the MFI (Mordenite Framework Inverted) structure was confirmed by observing the typical main Bragg peaks at 2θ of

8.03°, 8.94°, 23.24°, 24.05° and 24.52°. Also, the zeolite powder was highly crystallized and MFI-type was the only phase identified in the sample with orthorhombic system and Pnma-62 space group. The XRD pattern is similar to that of MFI-type zeolite structures reported in the scientific literature [119].

The SEM images in Figure 4.3 show that there is not a smooth coating of zeolite thin film at the end of optical fibre; causing light scattering and in turn weakening the reflection and diminishing the formation of clear interferograms. The structure of the zeolite particles is further confirmed in Figure 4.4.

Therefore, MFI-type structure was produced via the synthesis technique and successfully coated at the end-face of an optical fibre. The coated optical fibre can now be tested for water contaminant detection.

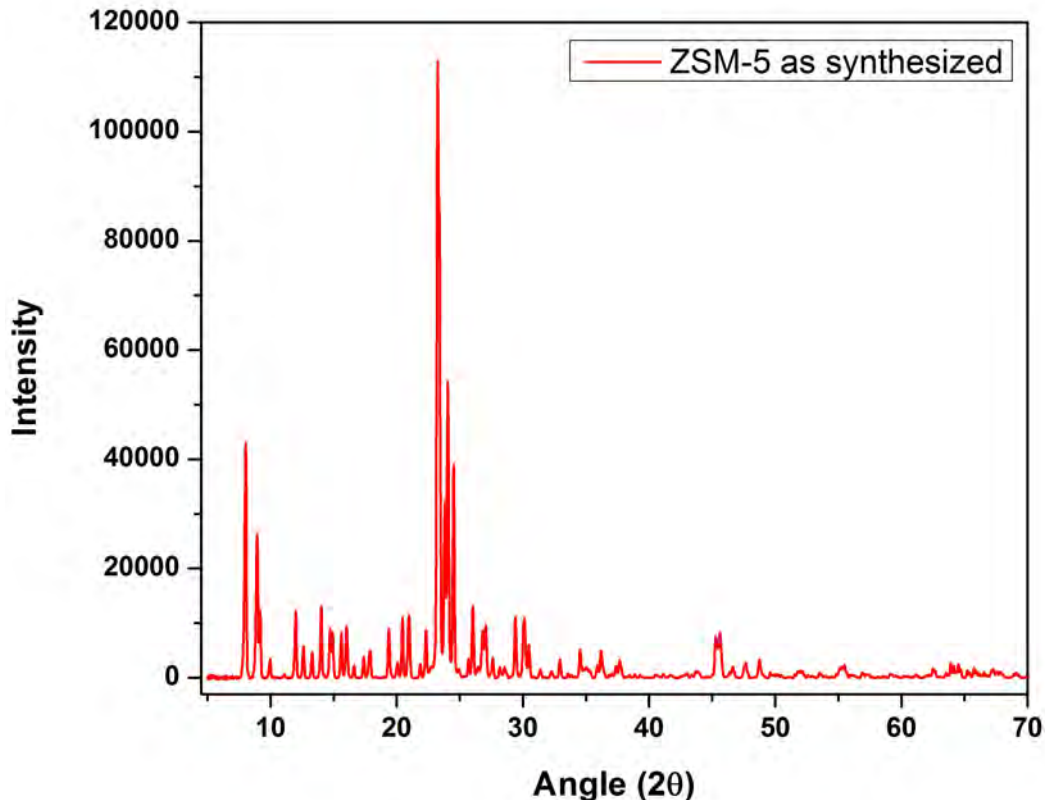


FIGURE 4.2: Zeolite powder XRD pattern

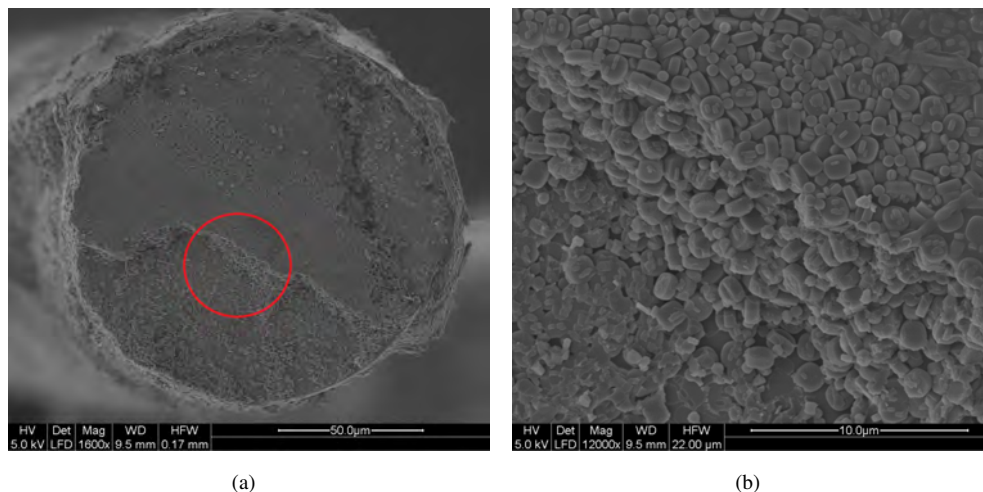


FIGURE 4.3: a) SEM image of zeolite thin film at the end-face of an optical fibre, b) close up of the region highlighted by the red circle

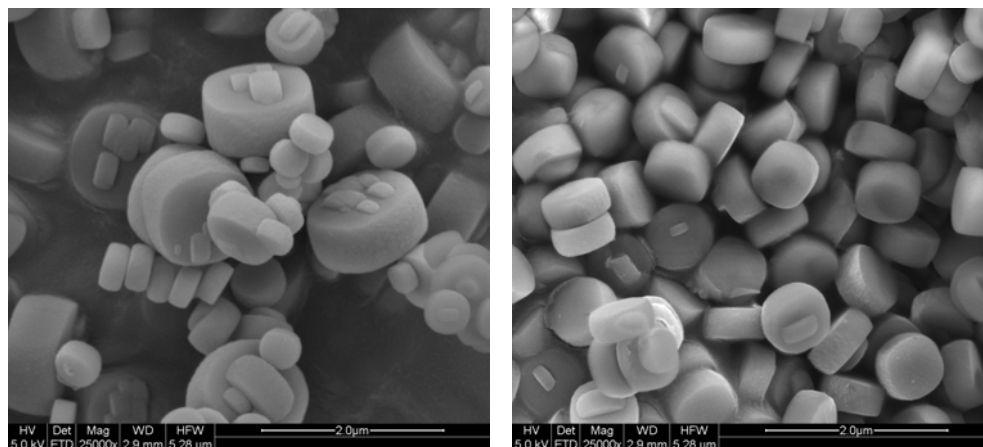


FIGURE 4.4: SEM images of zeolite powder

4.4 Contaminants Detection by Zeolite Thin Film Optical Fibre

The zeolite optical fibre thin film was used to detect contaminants (Section 2.1) in water. Different dilute solutions of ammonium, 4-aminopyridine and methanol in deionized water (DI) were prepared and the zeolite-fibre sensor was then immersed in these solutions. The interferograms did not change within 1% over 15 minutes when immersed in

these solutions. The Erbium ASE light source was used and interference spectra were obtained with OSA and the output signal was analyzed to determine the optical path differences by signal processing method described in Section 3.4.4.

4.4.1 Ammonium Detection

As it was mentioned earlier in Chapter 2, MFI-type zeolite thin films have been synthesized on LPFG optical fibres to detect trace ammonia vapour in water [120]. Here, the zeolite is coated on SMF-28 optical fibre and will be used to detect ammonium in liquid phase.

In this study, the concentration of ammonium in DI water was changed from nM to mM. For each concentration several interferograms were obtained at 10 s intervals after the sensor was dipped into the solution, and the average of these is shown in Figure 4.5; these resemble the expected curve shape shown in Figure 3.15. The sinusoidal spectral interferograms indicated that high quality interference signal was generated by the zeolite thin film. The shape of the signal changed with the increasing of ammonium concentration, indicating an increase in the refractive index of the zeolite thin film. The spectral positions of the interferogram peak and valley shifted to longer wavelengths with the increasing of ammonium concentration, indicating a solid increase in the optical thickness of the zeolite film which is shown in Figure 4.6 as a function of the ammonium concentration.

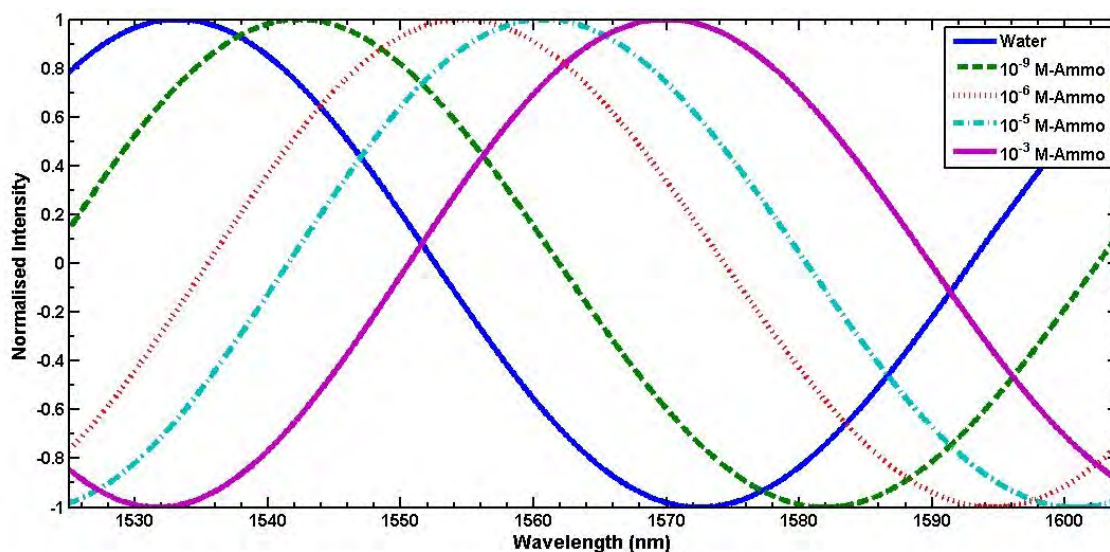


FIGURE 4.5: Interferograms in correlation with ammonium concentration in DI water

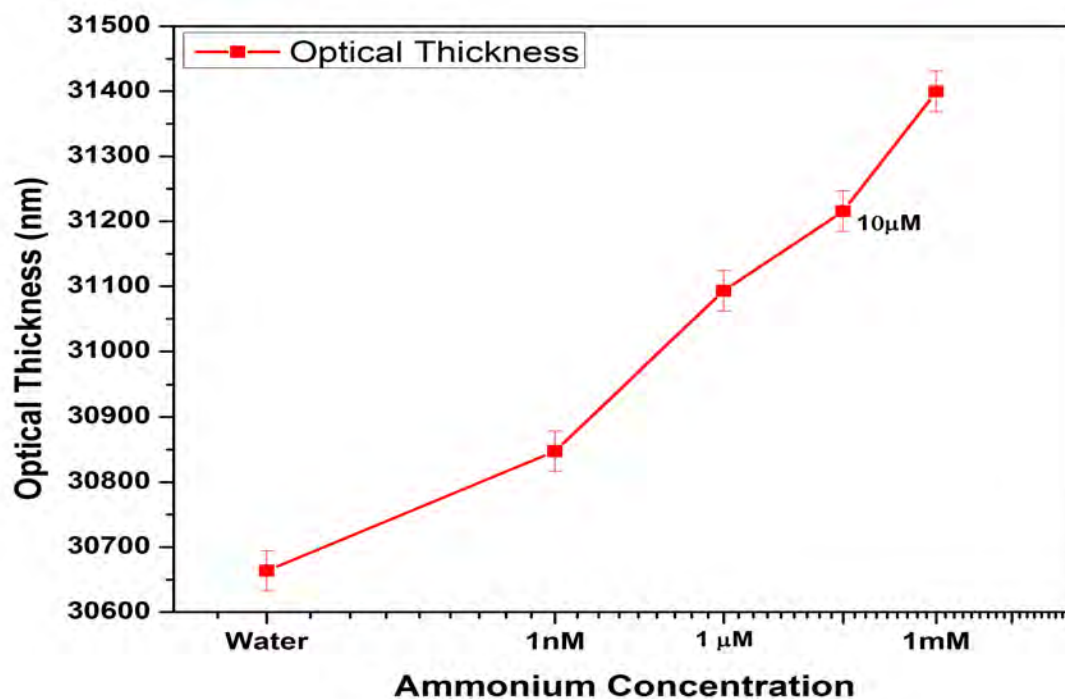


FIGURE 4.6: Optical thickness as a function of ammonium concentration in DI water

4.4.2 4-Aminopyridine Detection

4-Aminopyridine with estimated hydrodynamic (Stokes) radius of 2.5 \AA [121] is small enough to move freely in the inner surfaces of MFI-type zeolite cage with average

pore diameter of 5.3 Å [122]. Hence, it would be a good candidate to investigate the performance of zeolite as a sensor device.

The tested concentration of 4-aminopyridine in DI water ranged from pure water to 0.1 M concentrations. The interferograms in correlation with the 4-aminopyridine concentrations are shown in Figure 4.7; these resemble the expected curve shape shown in Figure 3.15. The computed optical thickness of the zeolite thin film is shown in Figure 4.8 as a function of the 4-aminopyridine concentration. The interferograms shifted towards the longer wavelength as the 4-aminopyridine concentration increased, which indicated that the optical thickness increased as more 4-aminopyridine molecules adsorbed in the zeolite and further confirmed the dependences of optical thickness on adsorption level. The sensor exhibited a detection limit of less than 1 mM (90 ppm) for 4-aminopyridine.

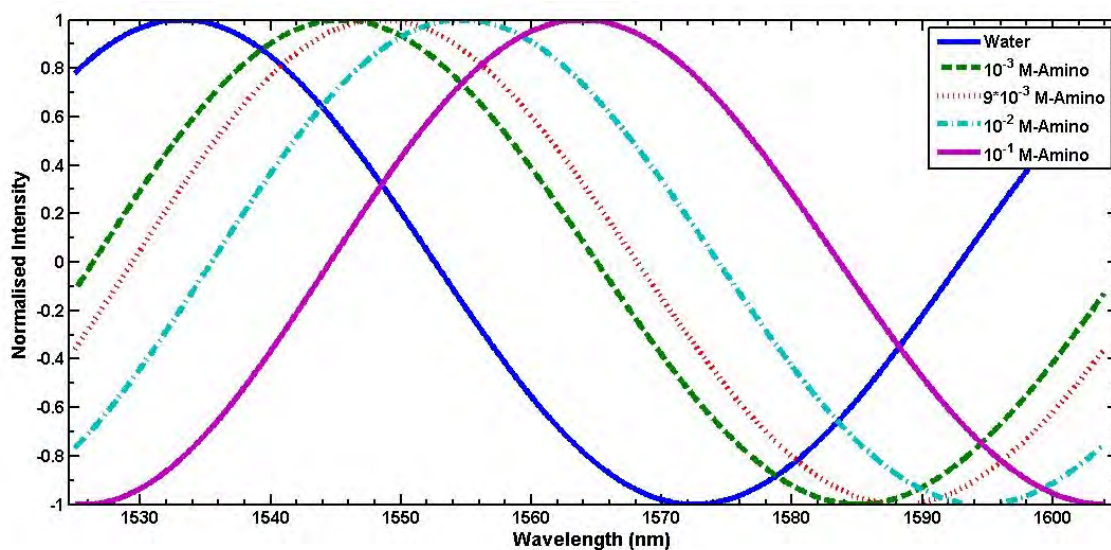


FIGURE 4.7: Interferograms in correlation with 4-aminopyridine concentration in DI water

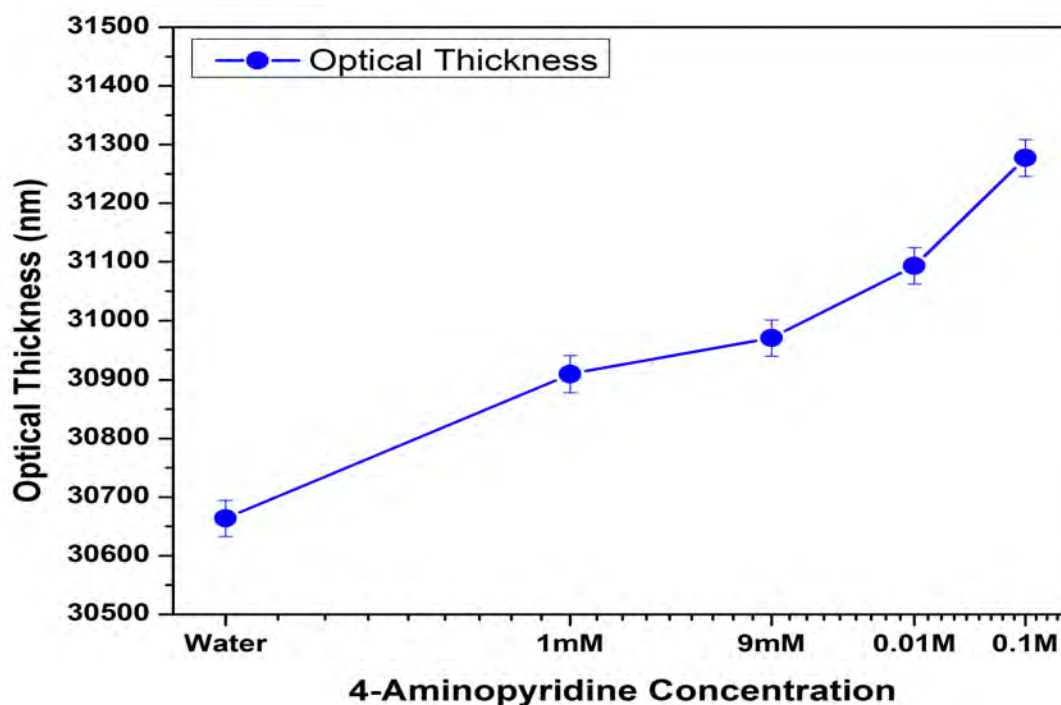


FIGURE 4.8: Optical Thickness as a function of 4-aminopyridine concentration in DI water

4.4.3 Methanol Detection Studies

In a similar way to 4-aminopyridine, the concentration of methanol in DI water ranged from pure DI water to 1 M methanol. Figure 4.9 shows several representative interferograms at different concentrations for the zeolite thin film optical fibre sensor; these resemble the expected curve shape shown in Figure 3.15. Figure 4.10 plot the optical thickness as a function of the methanol concentration for the above sensor. As can be seen, optical thickness did not change by a significant amount over the entire concentration range. There was a possible increase from water to 1 mM MeOH, which remained constant with increasing concentration up to 50 mM. However the value is the same as for water in 100 mM concentration. Consequently, there is not an indication of sensor's

positive response to increasing MeOH concentration in low ppm levels. This is at variance with the findings of other; the detection limit of methanol in water by zeolite thin film optical fibre has been reported as 1000 ppm (31 mM) [73].

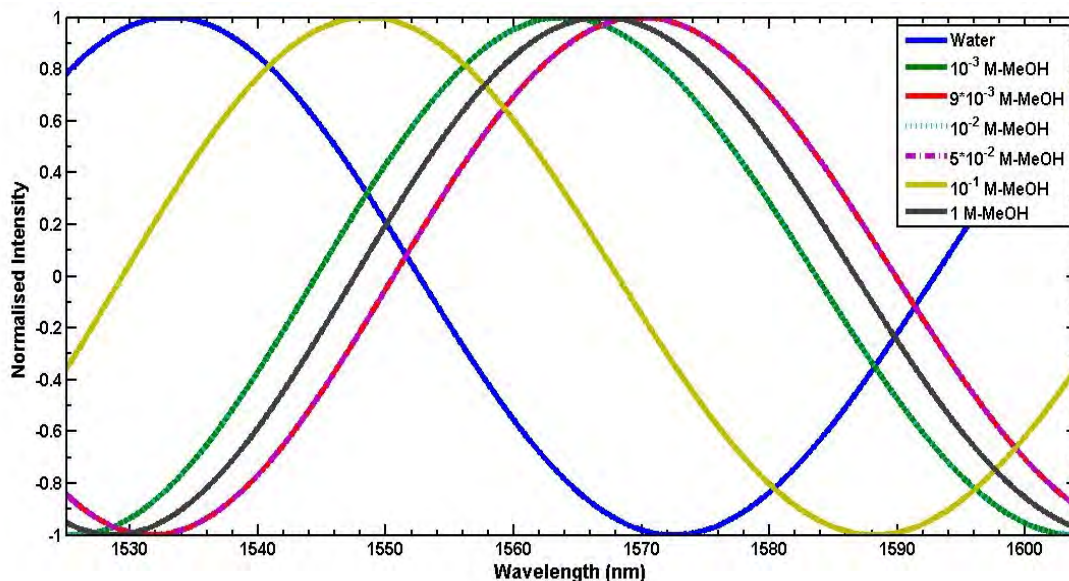


FIGURE 4.9: Interferograms in correlation with methanol concentration in DI water

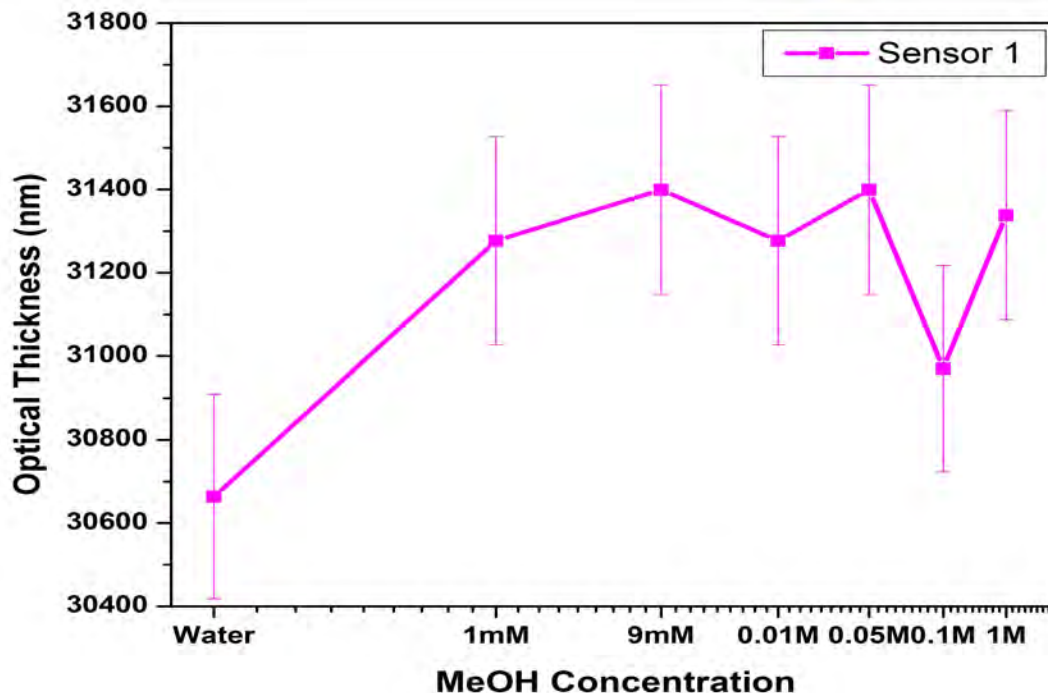


FIGURE 4.10: Optical Thickness as a function of methanol concentration in DI water

4.4.4 2-Propanol and Ethanol Adsorption Studies in Zeolite Thin Film

In this study, the coated optical fibers were immersed into solutions of ethanol and 2-propanol. The solution concentrations tested contained 20, 40, 60, 80 and 100% of the alcohol in DI water. The intensities were constant within 1% for the first 3 readings (20%, 40% and 60% of 2-propanol) over a 2 h period, whilst for the 80% 2-propanol sample, the fluctuation in intensity was around 5% over 45 minutes.

The performance of two selected sensors is shown in Figure 4.11 as a function of increasing 2-propanol and ethanol concentrations in water. As can be seen, there is decreasing trend in intensity over increasing the 2-propanol concentration in water. However, after an initial significant decline in intensity for the first ethanol concentration of 20%, there is no significant change in intensity for increasing ethanol concentration in water. However, the results are less rigorous, as they are not based on interferograms.

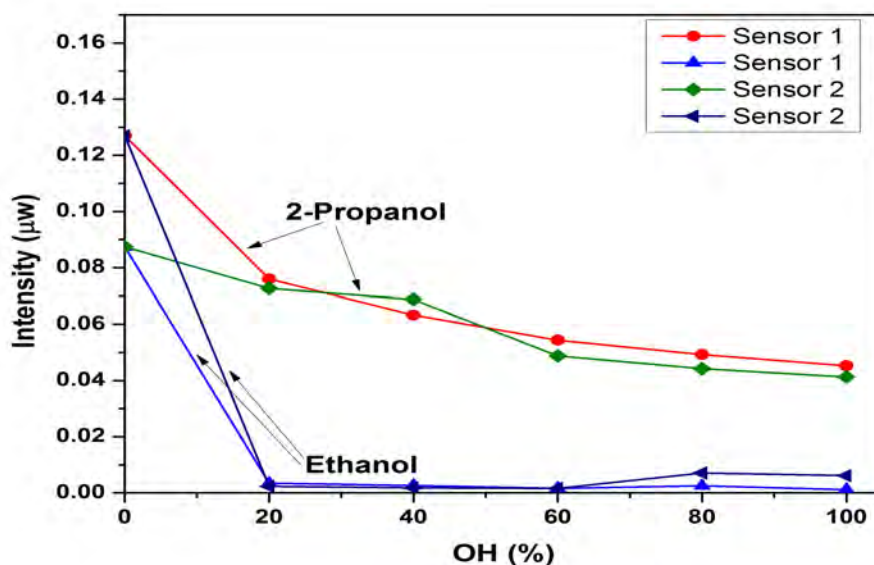


FIGURE 4.11: Performance of zeolite coated optical fibre sensors to 2-propanol and ethanol

4.5 Discussion and Summary

In this chapter, a MFI-type zeolite thin film based optical fibre sensor was successfully synthesized and used for studying the adsorption dependent optical property, optical thickness, of zeolite thin films. This sensor was used to detect ammonium, 4-aminopyridine, methanol, ethanol and 2-propanol in DI water.

The pH of ammonium in our solutions was 5, which shows that ammonium was present in ionic form (NH_4^+) rather than as free ammonia (NH_3). It has been found that the zeolite optical thickness increases with increasing the loading of ammonium molecules in the zeolite cage. Zeolites remove ammonium ions by means of ion-exchange and, at higher concentration, by adsorption [123]. While ammonium is attracted into the zeolite due to its small size and positive charge (zeolite has negative charge above its isoelectric point of around $\text{pH}=2$), it can also exchange when other cations present in solution [124]. However no other cations were added to the system. The more aluminium present in zeolite structure, the higher the capacity of the zeolite for NH_4^+ [123], but in our case no aluminium was added during synthesis implying the MFI-type structure was silicalite. Meanwhile the interaction with NH_4^+ was significant for sensing. In our study, by using zeolite thin film the ammonium detection limit is less than 1 nM (0.018 ppb) in water in liquid phase. However, by considering MFI-type's selectivity affinity order based on its Si/Al ratio and possible interfere with its ability to adsorb only ammonium, the applicability of this method in the presence of other ions must be further investigated. For instance, at high alumina content ($\text{Si/Al} = 30$), the material tends to exchange K^+ for Na^+ exhibiting little net ion uptake and decreasing the

alumina content led to a range of effects on porous properties and ion interactions [124].

4-aminopyridine has estimated hydrodynamic (Stokes) radius of 2.5 Å [121] and in comparison with elliptical cage structure [125] of MFI (pore diameters of 5.1×5.5 Å), is small enough to move freely in the inner surfaces of the zeolite's intrinsic pores. Also, 4-aminopyridine elimination from water could be directly related to the concentration of Lewis acid sites either by its decomposition on strong Lewis acid sites or by its adsorption on weak Lewis acid sites in zeolite. As FTIR investigation of pyridine adsorption/desorption in literature [126, 127] shows, mild and strong Lewis and Brønsted acid sites are present on MFI zeolites. Our study showed detection threshold of less than 90 ppm for 4-aminopyridine in water in liquid phase.

The end-face reflective sensor was demonstrated for detection of organic compounds (alcohols) dissolved in water. 2-propanol, ethanol and methanol aqueous solutions were used as model systems. The sensor exhibited low concentration (highly sensitive) quantitative measurement capability for ethanol than 2-propanol dissolved in water. The sensor signal decreased dramatically for ethanol from water to 20% concentration while was monotonically changed with the increase of 2-propanol concentration in the tested range under the same conditions. The theory behind this pattern is the permeation which molecules move through zeolite pores by surface diffusion. The organic molecules adsorb more strongly than water within the MFI framework because of its strong hydrophobicity, but nonzeolite pores and structural defects in the thin film may be a more significant disadvantage to hydrophobic membranes than hydrophilic ones because of silanol groups on the zeolite surface [125]. Also, the heats of adsorption for the alcohols increase with the number of carbons due to increased Van der Waals interactions [128].

This suggest that $-\Delta H$ of 2-propanol is greater than that of ethanol ($-\Delta H$ for ethanol: 70 ± 10 kJ/mol and $-\Delta H$ for 2-propanol: 90 ± 10 kJ/mol). Also the separation factor for the alcohols increases with increasing $-\Delta H$ of the alcohols. Considering the observed higher selectivity of ethanol in water to 2-propanol, it seems the likely explanation that ethanol more strongly penetrated into the zeolite, yielding a more reduced intensity at the lowest concentration of 20% [65]. Due to the inherent ability of zeolite to resist 2-propanol compared to ethanol, we observed a weaker reduction in intensity, but was more sensitive when increasing concentration up to 100%. The sensor did not respond to methanol because organic/water separation factors for alcohols tend to increase as carbon number increases (for methanol, ethanol and 1-propanol) and adsorption selectivity for linear alcohols/water increases as the alcohol carbon number increases because the alcohol adsorption strengths increase in this order.

4.6 Conclusion

In this chapter, the end-face zeolite coated sensor was demonstrated for detection of specific contaminants dissolved in water. Ammonium, 4-aminopyridine, ethanol, methanol and 2-propanol aqueous solutions were used as model systems. The sensor exhibited quantitative measurement capability for ammonium, 4-aminopyridine, ethanol and 2-propanol dissolved in water. The sensor's detection limit was 0.018 ppb for ammonium and 90 ppm for 4-aminopyridine. At low concentration (20% solution), the sensor's response to ethanol dissolved in water was much greater than that of 2-propanol dissolved in water, because the refractive index change induced by the substitution of water

molecules with ethanol molecules in zeolite pores was more than that induced by the substitution of water molecules with 2-propanol molecules.

Chapter 5

Metal Organic Framework Thin Film Coated on Optical Fibre End-Face for Aqueous Contaminant Detection

In chapter 4, a zeolite thin film was made at the end-face of an optical fibre and used as a sensor to detect 4-aminopyridine, ammonium, ethanol, 2-propanol and methanol in water. However, as discussed in Section 2.3.6, efficient adsorption depends upon the material's porosity, pore geometry and specific adsorption behaviour. The low porosity and small pores of the zeolite means that its use in the sensing area is limited to small molecules, i.e. it can not detect heavy organic molecules (e.g. herbicides or pesticides) in water. In this chapter, a new device of MOF thin film coated optical fibre end-face is fabricated and used as an in-fibre interferometer to study the changes to MOF refractive index as a function of chemical adsorption. For this purpose, Rhodamine-B and 4-Aminopyridine were used as specific examples.

5.1 Thin Film Role in Sensing

As noted earlier in Section 2.2, the reason a porous thin film is added is that a chemical sensor should provide the quantitative or qualitative information of the chemical species in a sample of interest. A bare optical fibre can act as a chemical sensor if it can determine the refractive index change caused by the absorption of species from a diluted solution. In other words, a bare optical fibre is able to give indication of changing the refractive index in various diluted solutions based on Fresnel reflection, but it does not recognize the solution composition (e.g. ethanol or methanol) and hence there will not be any selectivity with a bare optical fibre.

In chemical detection with a thin film based optical fibre, the thin film (optical material) can interact selectively with the analyte species that change the materials' optical properties. Such changes in optical properties are examined by the light propagating inside the optical fibre. The reflected light carrying the chemical information is then collected directly from the fibre to report the sensing results. Therefore a porous thin film increases the sensitivity and selectivity of an optical fibre sensor.

5.2 Optical Detection Method

The optical detection method is based on using Fabry-Perot Interferometry technique described in Section 2.2.2. Figure 5.1 shows the proposed end-face coated reflective sensor structure, which will be obtained by synthesizing a UiO-66 thin film on a perpendicularly cleaved end-face of an optical fibre. The input light will first be partially

reflected back (I_1) from the fibre-MOF interface. The rest of the light is transmitted through the MOF thin film and again be partially reflected back (I_2) from the MOF - water interface. The interference of the two reflected beams (sensor signal) is recorded by OSA for signal processing and calculation of the thin film optical thickness.

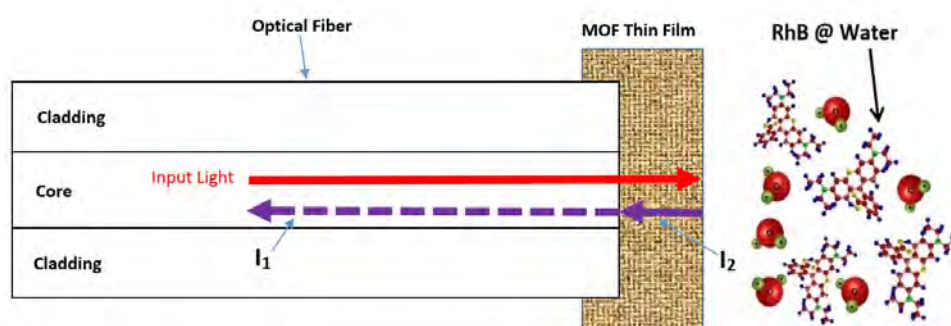


FIGURE 5.1: Structure of the end-face MOF reflective sensor

5.3 MOF Water Stability

MOFs with metal-carboxylate bonds have been shown to have varying degrees of water stability. Usually each MOF degrades under various temperature and humidity conditions measured over experiments lasting 28 days. An example is given by Cu-BTC (HKUST-1)(Hong Kong University of Science and Technology) is a MOF made of copper nodes with 1,3,5-benzenetricarboxylic acid struts between them. At conditions of 90% relative humidity (RH) and 25 °C, water uptake for Cu-BTC is shown to be higher than at 90% RH and 40 °C. This is due to the degradation of the inner structure of Cu-BTC as measured by XRD which occurs more readily at lower temperatures [129, 130]. However the external surfaces of Cu-BTC degrade more readily at conditions of 90% RH and 40 °C. Mg-MOF-74 (Mg/DOBDC) has a nearly complete loss of surface area after just one day of exposure to each of the conditions studied above; however the

PXRD patterns show only a change in the [1 0 0] peak [129]. Furthermore, UiO-66 (Zr-BDC) (Universitetet i Oslo), a MOF made up of $[\text{Zr}_6\text{O}_4(\text{OH})_4]$ clusters with 1,4-benzodicarboxylic acid struts, was stable to each of the aging conditions for the full 28 days of study. Therefore, a promising material for chemical sensing in aqueous systems appears to be the UiO-66 MOF structure [129, 131]. Figure 5.2 and Figure 5.3 show the structure of UiO-66 and Cu-BTC MOFs [129]. The spheres represent the pore sizes within the framework which can be used for storage purposes. Figure 5.4 illustrates the structure change after water uptake.

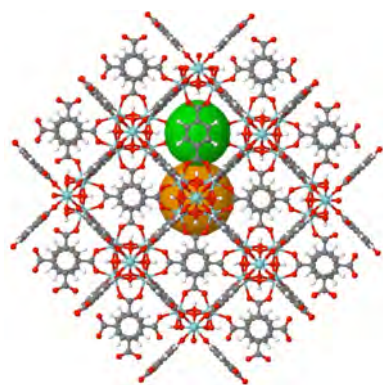


FIGURE 5.2: UiO-66 MOF Structure

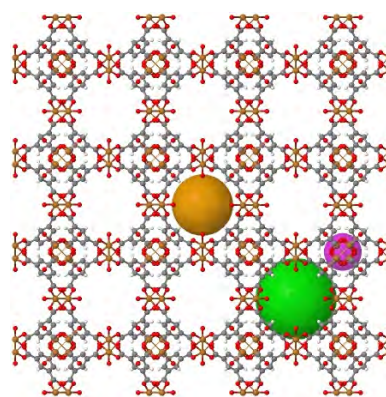


FIGURE 5.3: Cu-BTC (HKUST-1) MOF Structure

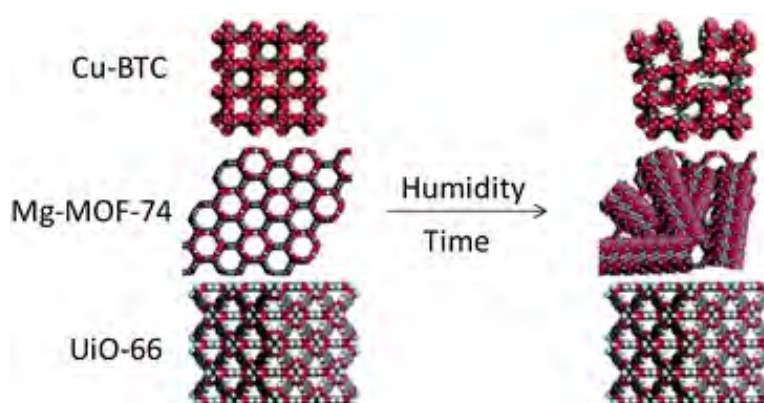


FIGURE 5.4: Cu-BTC, Mg-MOF-74 and UiO-66 structure change after water uptake [129]

5.4 Optical Fibre UiO-66 Thin Film Synthesis

5.4.1 Synthesis of UiO-66

UiO-66 was synthesized according to the recipe described in previous work by Lau et al. and Schaate et al. [3, 132]. 0.60 g (2.68 mmol) of $ZrCl_4$, 0.43 g (2.68 mmol) of 1,4-benzenedicarboxylic acid (BDC) and 5.00 g (40.96 mmol) of benzoic acid were dissolved in 100 mL of dimethylformamide (DMF) and 5 mL of deionized (DI) water under constant stirring for 2 hours. The mixture was left at 120 °C for 24 hours in the pre-heated oven. After cooling down to room temperature, a clear phase separation could be observed between the solids and the solvents. The nanoparticles were centrifuged at 20000 rpm for 15 minutes and washed first with fresh DMF (at least 3 times) and second with methanol overnight. They were dried at 80 °C under vacuum overnight.

The SEM images of the UiO-66 powder material shown in Figure 5.5, show distinct particles with a particle size distribution between 60 and 200 nm.

Further confirmation of the formation of UiO-66 material was obtained from powders using XRD, TGA and nitrogen adsorption isotherm. XRD result of UiO-66 has a main peak at 2θ angles of 7.4° and some characteristic peaks at 2θ of 8.5° , 25.9° , and 30.8° as shown in Figure 5.6 and proves that as-synthesized UiO-66 has exactly the same crystal pattern as a standard UiO-66 powder (the Crystallographic Information File (CIF)) [133]. The TGA result shown in Figure 5.7 exhibits an slow initial weight

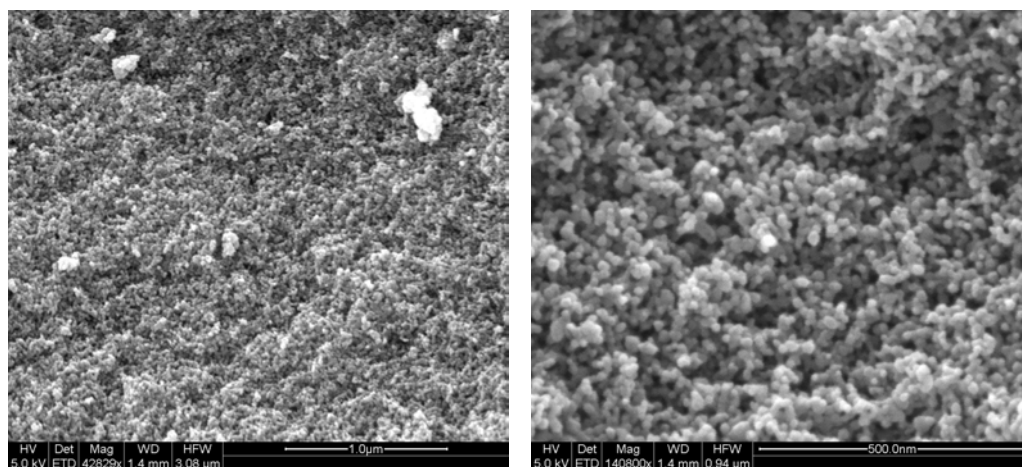


FIGURE 5.5: SEM images of UiO-66 powder

loss up to 300 °C (DMF molecule removal), with a clear shoulder around 100 °C (loosening physisorbed water). The weight became stabilized at 518 °C and the sample was left with the 36.65% of the starting weight. The residual material at the end of the TGA experiment is simply ZrO_2 . The TGA result confirms the UiO-66 weight loss pattern in agreement with the literature [134]. The porous feature of the UiO-66 was also analysed by N_2 porosimetry at 77 K. The isotherms, shown in Figure 5.8, show an indication of a microporous material and the shape of the isotherms are the same as reported for standard UiO-66 [134] with the rise of the isotherm in the $p/p_o > 0.6$ region. Calculated BET surface area of the as-synthesized UiO-66 is 1304 m^2/g with a micropore volume of 1.38 cm^3/g .

Therefore, the characterization of the UiO-66 material confirms the correct structure and porous properties suitable for capture of organic contaminants that can be detected when it is coated on an optical fibre end-face.

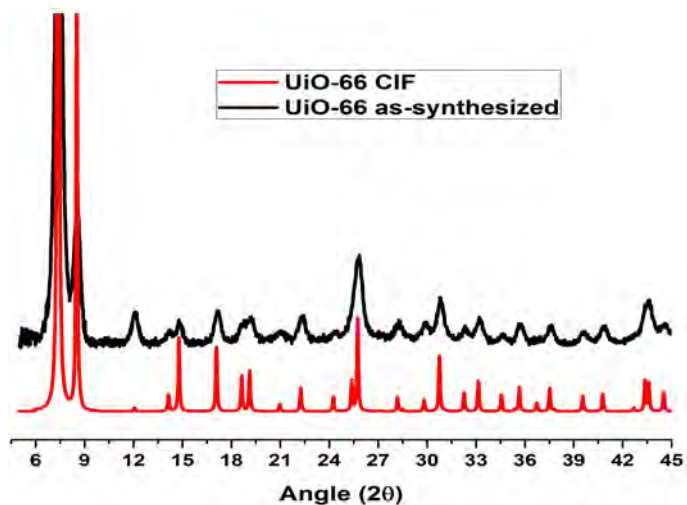


FIGURE 5.6: UiO-66 powder XRD

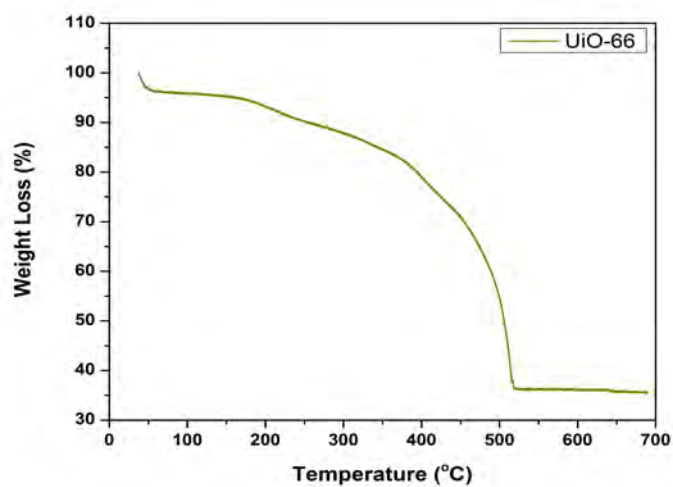


FIGURE 5.7: TGA curve for UiO-66 powder (in air at 3°/min)

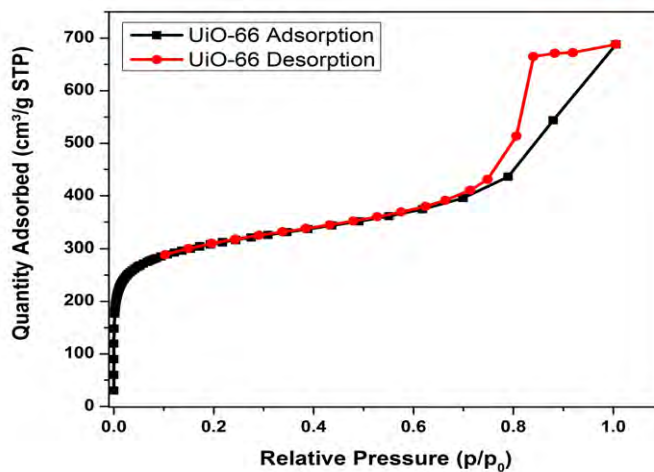


FIGURE 5.8: UiO-66 nitrogen adsorption isotherm

5.4.2 Synthesis of Optical Fibre UiO-66 Thin Film

Most commonly, MOF films have been synthesized directly on the surface of interest from the appropriate molecular and ionic precursors. Typically the surface is a metal, metal oxide [135, 136] and glass or silicon [137]. Film formation can sometimes be accomplished by simply placing a platform in a reactor/oven with the MOF precursors. These direct growth approaches often require functionalization of the surface with a self-assembled monolayer to nucleate film formation and exceed the growth rate [138].

In this study, Radio Frequency Glow Discharge (RFGD) plasma polymerization (Section 3.2.1) was used with the same conditions described in Section 3.2.1.1 to deposit a layer of diethylene glycol dimethyl ether (diglyme) on the optical fibre right cleaved end-face surface. After monomer deposition, the prepared optical fibres were placed in an untreated precursor solution of UiO-66, were then heated at 120 °C for 24 h to allow the MOF thin film to grow on the exposed surface of the optical fibre. After 24 hours, the fibres were taken out and washed gently as above procedure with DMF and methanol to remove unreacted starting reagents.

The SEM image in Figure 5.9-b from optical fibre end-face shows formation of a thin layer of UiO-66 for comparison with a bare optical fibre in Figure 5.9-a. As can be seen, the thin film has some cracks which could be due to exposing it to air just after taking it out of the precursor solution. These cracks would not have an impact on sensor results if they are not located at the centre of the optical fibre (core area with 8.2 μm diameter coloured in yellow in Figure 5.9-b). Further production of optical fibres with MOF thin films confirmed a smooth thin film layer (the film thickness and surface

smoothness are important factors affecting the optical signal quality) deposition at the end-face without any cracks (Figure 5.9-c). The final layer's thickness is 1.6-1.9 μm , from Figure 5.9-d and -e, and since there are 10-12 layers present (Figure 5.9-f), the estimated thin film thickness is 17-22 μm .

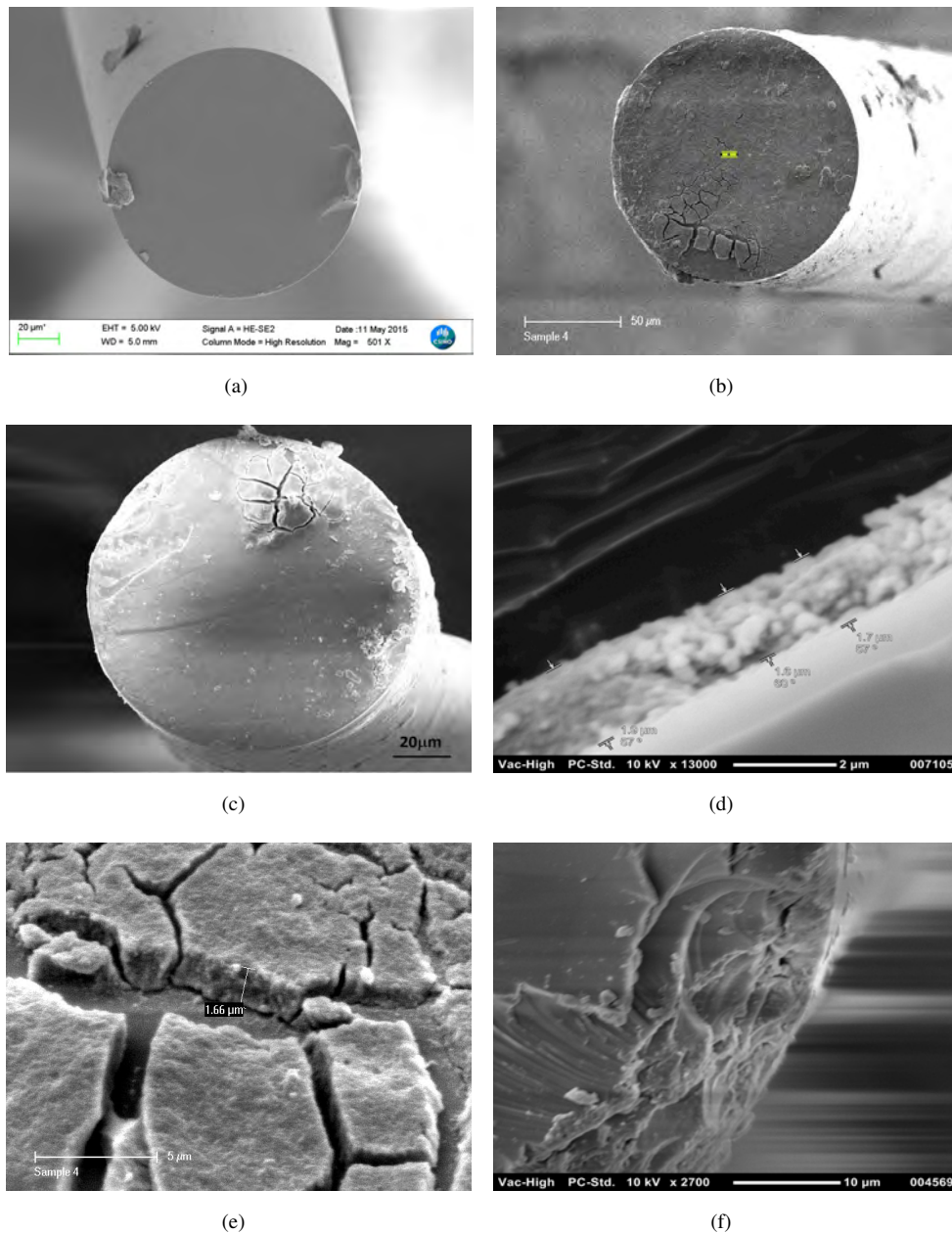


FIGURE 5.9: SEM images: a) A bare optical fibre, b) UiO-66 optical fibre thin film top view, first sample, c) UiO-66 optical fibre thin film, second sample, d) side view at x13000 of UiO-66 optical fibre thin film, e) view of another UiO-66 optical fibre thin film, f) accumulation of layers

5.5 Contaminants Detection by UiO-66 Optical Fibre Thin Film

In order to evaluate the UiO-66 thin film coated optical fiber as a sensor, two different contaminants (Section 2.1), Rhodamine-B (RhB) and 4-Aminopyridine (4-AP) were tested. Figure 5.10 shows the two different cages structures of UiO-66: a tetrahedron (6 Å) and an octahedron (9 Å), RhB molecule with 15.6 Å × 13.5 Å × 4.2 Å dimensions and 4-AP molecule with 5.6 Å × 4.4 Å size.

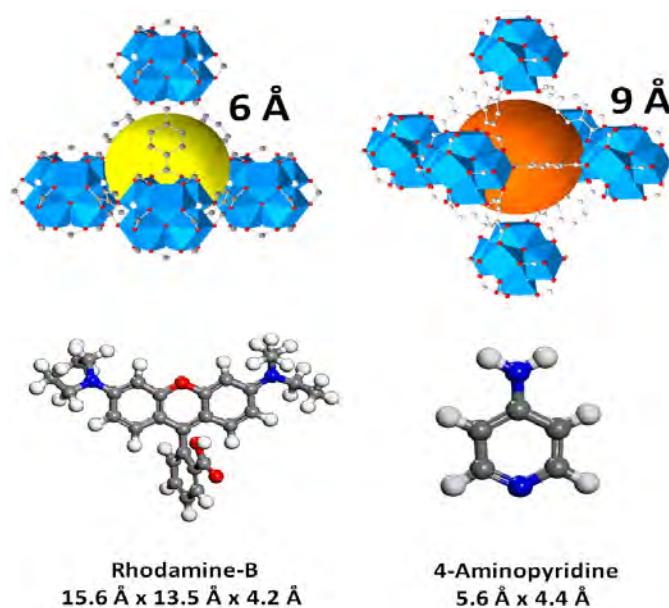


FIGURE 5.10: An illustration of two cages structures of UiO-66, RhB and 4-AP molecules

The Erbium ASE light source was used and interference spectra were obtained with OSA and the output signal was analyzed to determine the optical path differences by signal processing method described in Section 3.4.4.

5.5.1 Rhodamine-B Detection

RhB is a good candidate to investigate the performance of UiO-66 as a sensor device, and previous work has shown its absorption into the surface of UiO-66 framework is due to electrostatic interaction between RhB (a hydrophilic cationic dye [139, 140]) and UiO-66 MOF (anionic material) as it is shown in Figure 5.11 with the maximum dye adsorption capacities of dried UiO-66 (dye concentration = 20 ppm and pH = 7) of 53.307, 70.679 and 75.850 mg.g⁻¹ at 273, 303 and 323 K respectively [141].

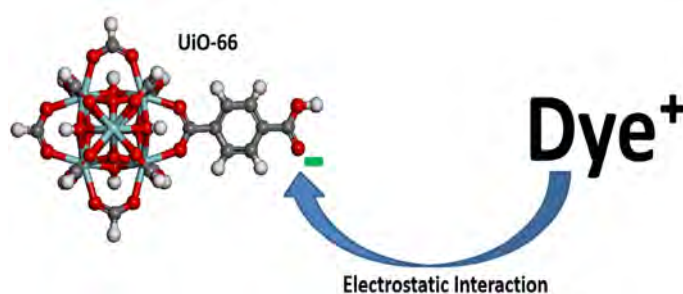


FIGURE 5.11: Mechanism diagram of RhB adsorption on UiO-66 surface

Diluted solutions of 0.1 mM (48 ppm), 1 mM (480 ppm), 9 mM (4311 ppm) and 15 mM (7185 ppm) of RhB in DI water were tested with the optical fibre thin film. The spectral interferograms generated by the UiO-66 thin film at these concentrations are shown in Figure 5.12; their sinusoidal shape shows that the thin film indeed generated interference signals; these resemble the expected curve shape shown in Figure 3.15. The interferograms did not change within 1% over 15 minutes when immersed in 50 ppm or 100 ppm RhB solutions. The spectral positions of the interferogram peak and valley shifted to longer wavelength with an increasing RhB concentration, with the tracked maximum/minimum of the interferogram moves out from the investigated wavelength range at large concentrations, indicating that there is an increase in the optical thickness

of the UiO-66 film, as is clear from Figure 5.13. So it can be concluded that RhB is absorbing within the UiO-66 MOF thin film and the obtained limit of detection demonstrated by this method is 48 ppm.

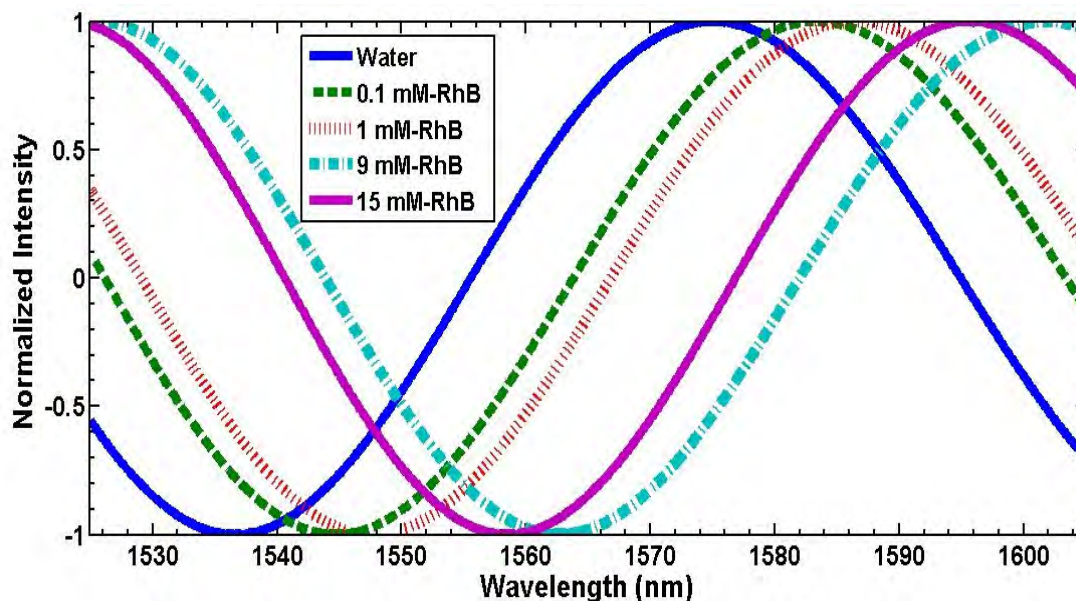


FIGURE 5.12: Interferograms in correlation with RhB concentration in DI water

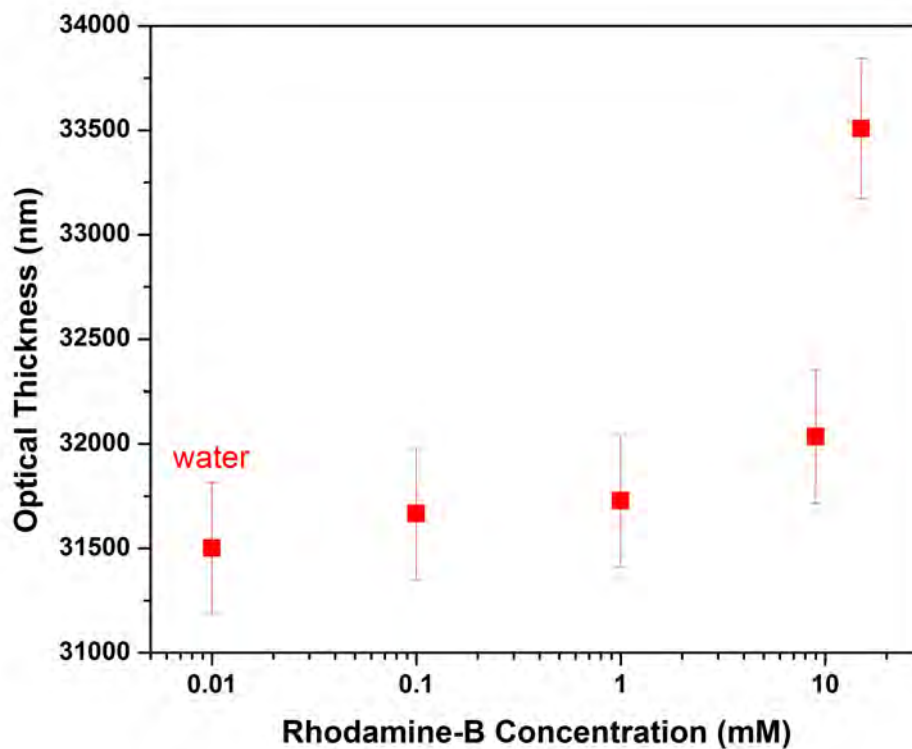


FIGURE 5.13: Optical thickness as a function of RhB concentration in DI water, point labelled “water” included for reference

To further confirm adsorption of RhB in UiO-66, 10 mg of UiO-66 activated/dehydroxylated powder (the powder was heated up to 120 °C for 2 h under dynamic vacuum) was added to a 5 ml solution containing 20 ppm RhB under constant stirring. Before taking a sample from the middle of the vial, the mixture was left at rest for 5 minutes in order to precipitate UiO-66 powder to the bottom of the vial. Aliquots were taken after 10 min, 30 min, 60 min and 1 day of stirring the mixture. Figure 5.14 shows the peak of corresponding to RhB at 554 nm and after the addition of UiO-66, the peak reduced in intensity over time which shows that RhB is absorbed from 20 ppm aqueous solution into the UiO-66 surface and is a further confirmation of our Fabry-Perot interferometry method.

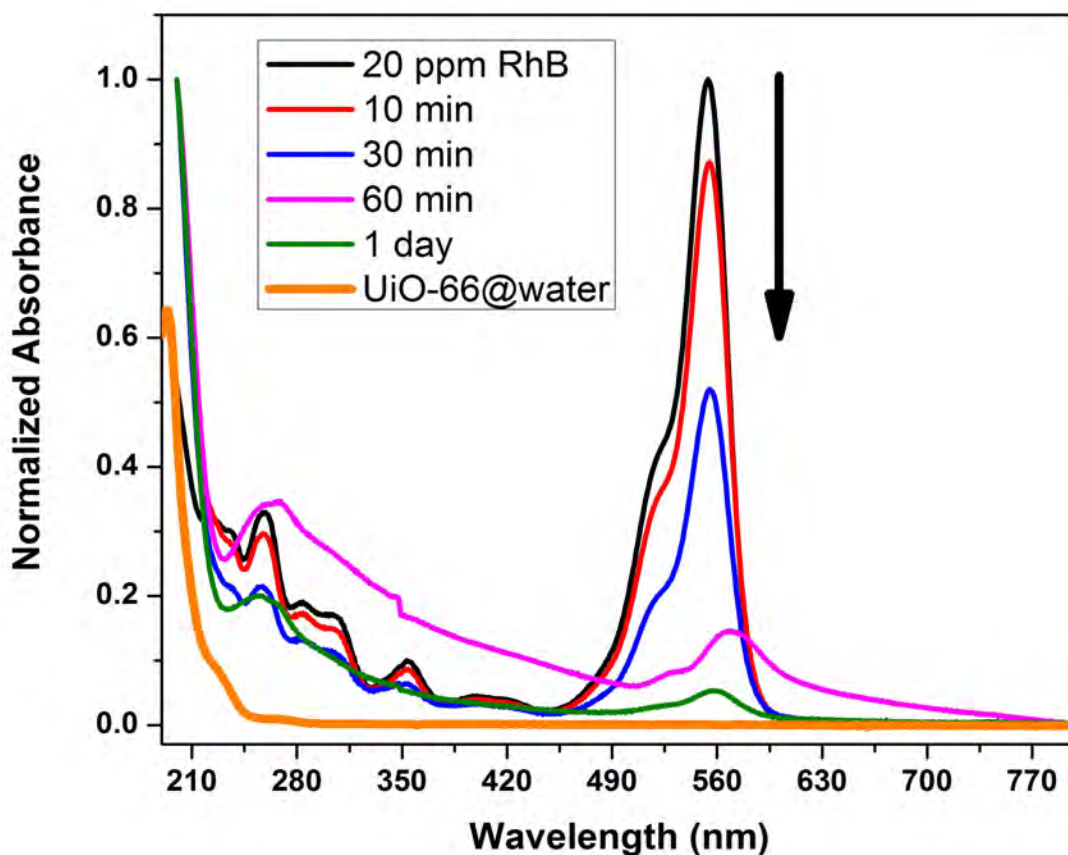


FIGURE 5.14: UV-Vis absorption pattern of a solution containing RhB and UiO-66 powder

5.5.1.1 RhB Adsorption Mechanism

Owing to the big molecular size of RhB (Figure 5.10), it can only adsorb on the external surface of the UiO-66 but not inside its micropore. As explained by He et al. [141], the increasing RhB uptake at UiO-66 by increasing its concentration, could be attributed to the increase in the driving force from the concentration gradient. In other words, under the same condition, with higher concentration of RhB, the active sites of MOF are surrounded by many more RhB molecules and the adsorption will proceed more sufficiently. Their calculated negative Gibbs free energy (ΔG_0) confirmed the feasibility of the adsorption process and spontaneous nature of it. Since their calculated value of enthalpy change (ΔH_0) was $15.096 \text{ kJ.mol}^{-1}$, it indicated that the adsorption is endothermic and may involve chemical and physical processes, based on the suggestion of Kara et al. [142] that the value of ΔH_0 for chemical adsorption is more than 40 kJ.mol^{-1} [141].

5.5.2 4-Aminopyridine Detection

Diluted solutions of 1 mM (94 ppm), 9 mM (846 ppm), 10 mM (940 ppm), 50 mM (4700 ppm) and 100 mM (9400 ppm) of 4-AP in DI water were tested with the optical fibre thin film. The spectral interferograms generated by the UiO-66 thin film at different 4-AP concentrations is shown in Figure 5.15. The sinusoidal spectral interferograms indicated that an interference signal was generated by the thin film; these resemble the expected curve shape shown in Figure 3.15. As can be seen, the spectral positions of

the interferogram peak and valley did not shift to longer wavelength in order of increasing the 4-AP concentration in water. Further data signal processing showed that by increasing the 4-AP concentration, the optical thickness started to fluctuate and it did not follow any specific pattern (Figure 5.16). Therefore, it concluded that 4-AP was not loading into UiO-66 pores and instead was attaching to its surface, blocking the accessible pores and resulting the initial increase of optical thickness.

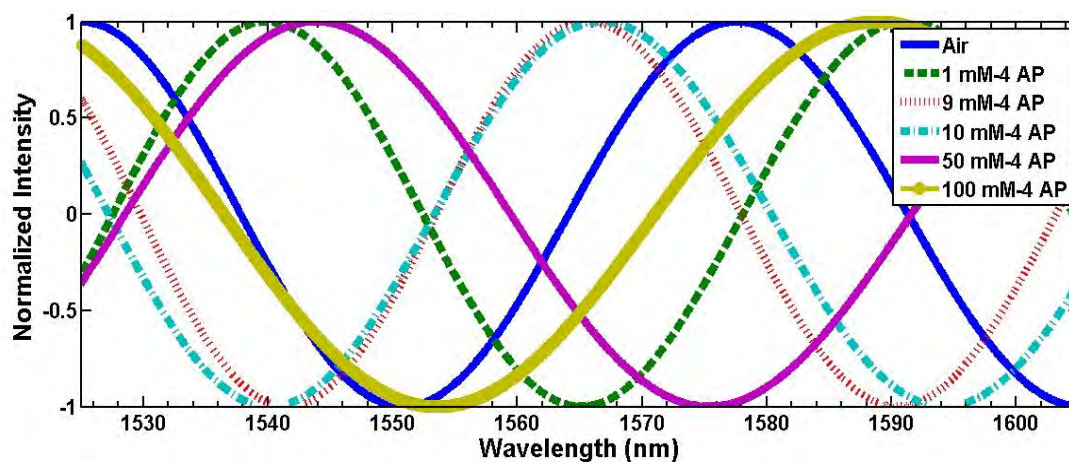


FIGURE 5.15: Interferograms in correlation with 4-AP concentration in DI water

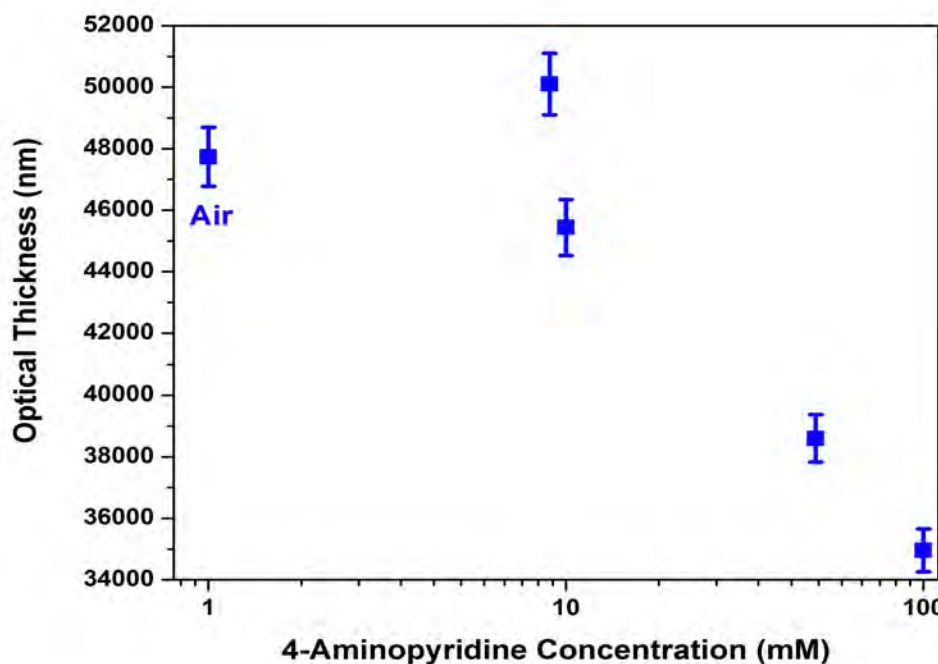


FIGURE 5.16: Optical thickness as a function of 4-AP concentration in DI water, point labelled “water” included for reference

In a similar way to RhB, to further confirm the adsorption of 4-AP on UiO-66 surface, 10 mg of UiO-66 activated/dehydroxylated powder (the powder was heated up to 120 °C for 2 h under dynamic vacuum) was added to a 5 ml solution containing 20 ppm 4-AP under constant stirring. Figure 5.17 shows the UV-Vis adsorption pattern of 4-AP after the addition of UiO-66 in which the 4-AP peak at 243 nm shifted to 262 nm after 2 minutes of adding UiO-66 that corresponds to characteristic peak of deprotonated 4-AP [143] and remained the same for longer impregnation times. The new 262 nm peak intensity did not change considerably for longer times which could be an indication of 4-AP adsorption on UiO-66 surface rather than inside its cage during the first 2 minutes.

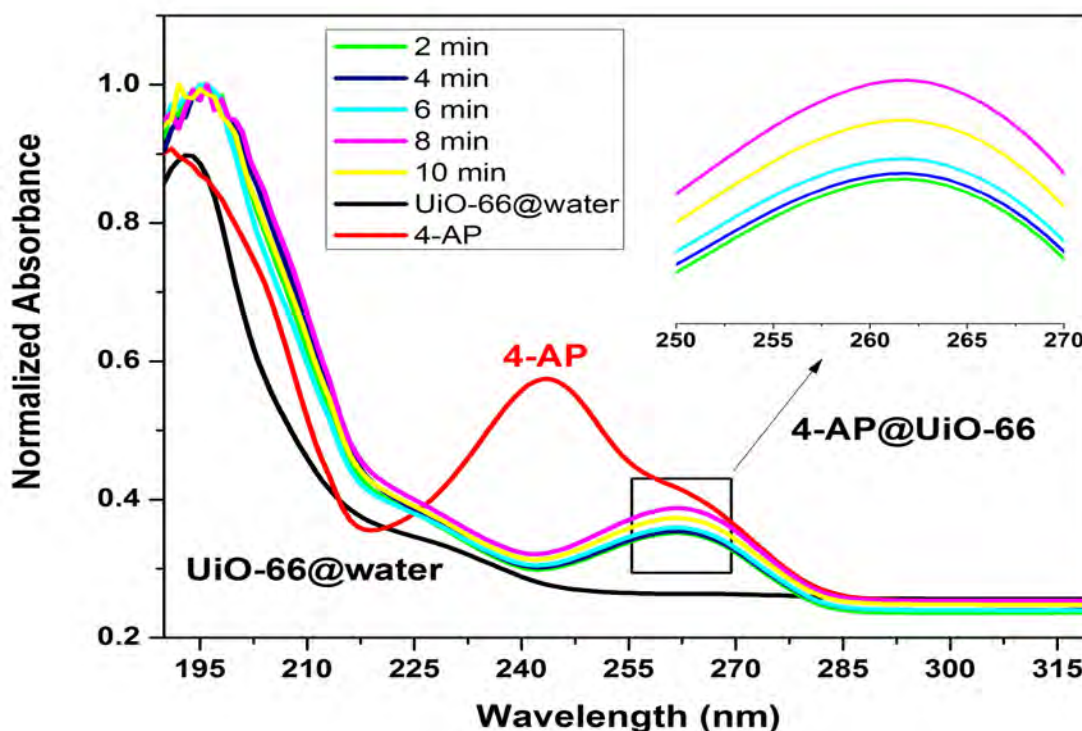


FIGURE 5.17: UV-Vis absorption pattern of a solution containing 4-AP and UiO-66 powder

Further experiment with increased amount of UiO-66 in 5 ml solution of 20 ppm 4-AP revealed the dependence of 4-AP water removal to UiO-66 mass increase during the first 2 minutes of their impregnation (Figure 5.18).

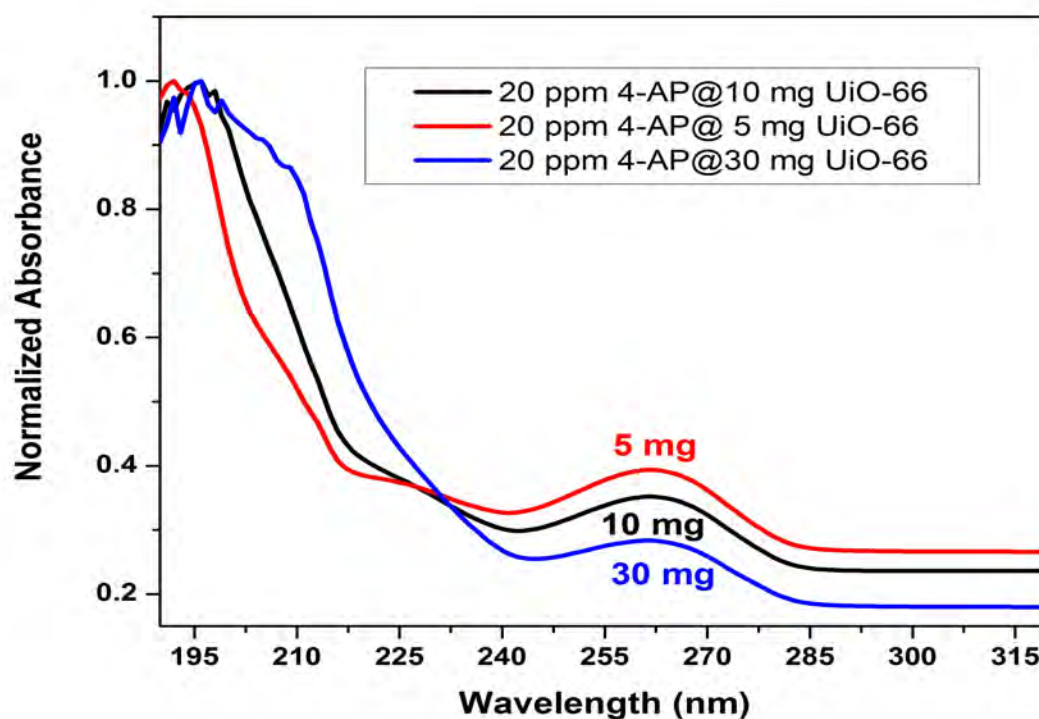


FIGURE 5.18: UV-Vis absorption pattern of a solution containing 20 ppm 4-AP and UiO-66 powder at different amounts

5.5.2.1 4-AP Adsorption Mechanism

UiO-66 (Zr-BDC) MOF is made up of $[\text{Zr}_6\text{O}_4(\text{OH})_4]$ clusters with 1,4-benzodicycarboxylic acid (BDC) struts bound to 12 terephthalate anions and is assembled by two different cages structures: a super tetrahedron and a super octahedron consisting of zirconium, oxygen, carbon and hydrogen in which all of the $\mu_3\text{-O}$ or $\mu_3\text{-OH}$ groups in the $\text{Zr}_6\text{O}_4(\text{OH})_4$ cluster point toward the tetrahedral cages. Deprotonated 4-AP is attached to the carboxylic group of $\text{Zr}_6\text{O}_4(\text{OH})_4\text{-(COO)-BDC}$ forming an amide bond.

To confirm the above mechanism, FTIR spectrum of 4-AP@UiO-66 in Figure 5.19 was analyzed, showing appearance of significant new bands centered at 1255 cm^{-1} , 1663 cm^{-1} and 1702 cm^{-1} . The 1255 cm^{-1} peak corresponding to the C-N group proves the binding of nitrogen onto UiO-66 adsorbents. Moreover, the peaks rising at 1663

and 1702 cm^{-1} are related to the vibrations of the N-H and C=O bonds respectively, indicating the formation of amide group. In addition, the small peak at 3674 cm^{-1} in UiO-66 powder is assigned to a triply-bridged OH in the inner core of $\text{Zr}_6(\mu_3\text{-O})_4(\mu_3\text{-OH})_4$ being disappeared in 4-AP@UiO-66.

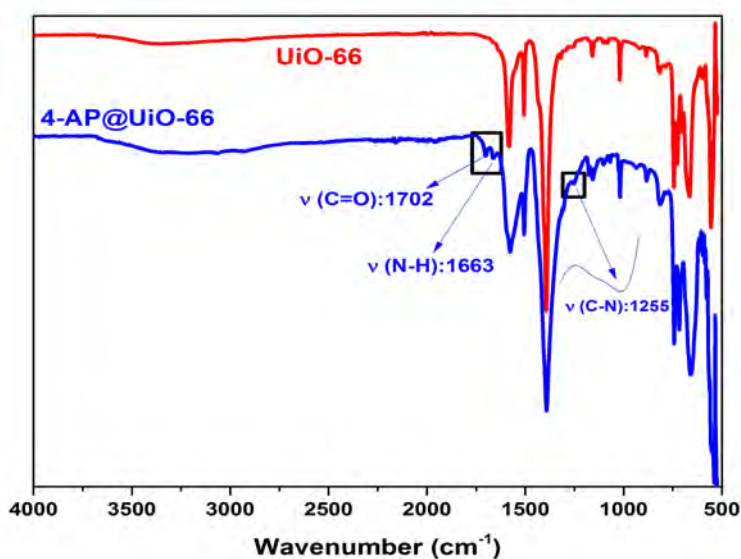


FIGURE 5.19: FTIR spectrum of 4-AP@UiO-66 sample

5.6 Conclusion and Future Work

In this chapter, UiO-66 thin film has been deposited successfully at the end-face of an optical fibre and was used for detection of specific contaminants dissolved in water, Rhodamine-B and 4-Aminopyridine. The wavelength shift of the FPI spectra has been shown to be dependent upon the change in optical thickness of UiO-66 thin film via loading the RhB molecules with sensor threshold operating limit of 47 ppm. This can be explained by the fact that the size of the UiO-66 pores matched well the size of the RhB molecule. While, due to the strong interaction between hydroxide ligand of UiO-66 and the deprotonated 4-AP, all the accessible pores of UiO-66 were blocked by formation of

amide bond between the carboxylic group of the UiO-66 framework and the amino group of the 4-AP and the measurement of the sensor response towards 4-AP concentration change in water by means of optical fibre was not successful. However, the concept of the MOF integrated optical fibre based sensor has been proved and represents the new strategy in the field of chemical sensing. The cross-sensitivity and the response of the sensor to the mixtures of contaminants is planned to be examined in our further work. In order to increase the sensor sensitivity, a number of optimization procedures are planned, including functionalization of the UiO-66 thin film by ligand exchange along with enhanced approaches to use Bragg gratings in optical fibres (FBGs).

Chapter 6

Triggered Release of 5-Fluorouracil from Optical Fibre Thin Film

After successfully producing a UiO-66 thin film at the end-face of the optical fibre and validating its capability to capture specific contaminants from water (Rhodamine-B) in Chapter 5, in this chapter, the new UiO-66 MOF thin film was utilized for 5-Fluorouracil (5-FU) anti-cancer medicine encapsulation. As illustrated in Figure 6.1, the aim is to investigate whether the drug can be released by delivering light *via* the optical fibre, and this included measurements at several incident wavelengths. Additionally, for the drug encapsulation, both impregnation and sublimation were tested.

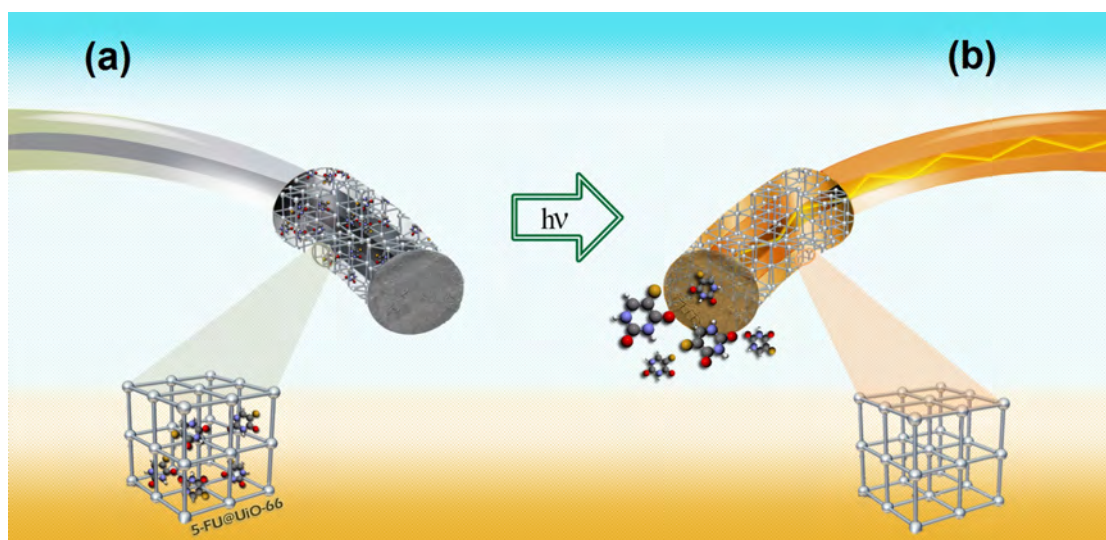


FIGURE 6.1: Schematic illustration describing a): the encapsulation of 5-FU into the UiO-66 thin film optical fibre and b): the novel drug delivery system achieved using light

6.1 Potential for Triggered Release as an Alternative to Chemotherapy

Zr-MOF UiO-66 is based on the $Zr_6O_4(OH)_4$ SBU (Secondary Building Unit) bound to 12 terephthalate anions and is assembled by two cages structures: a super tetrahedron and a super octahedron consisting of zirconium, oxygen, carbon and hydrogen. The combination of one octahedral cage and two adjacent tetrahedral cages form a cubic unit consisting of eight inorganic bricks (Figure 6.2). When all the linkers are present, there is a well-defined pore at 7.5 Å and when about 4 linkers per node are missing, then this pore size increases to 12 Å. The pores are accessible through microporous triangular windows of around 5-7 Å [144].

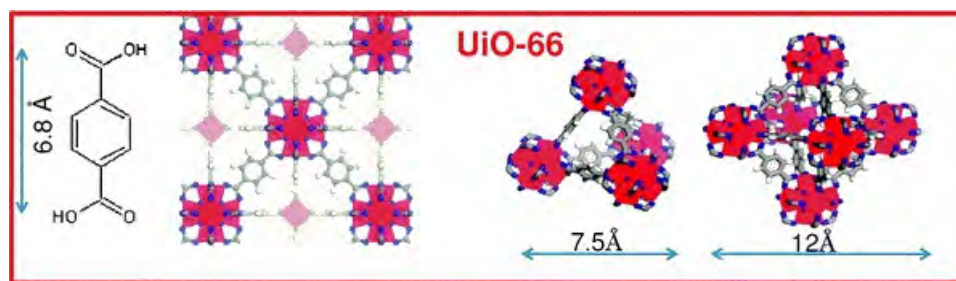


FIGURE 6.2: UiO-66 MOF structure showing internal cage pore size [144]

As discussed in Section 2.4.2, various types of MOFs have been successfully used for drug delivery studies [5–7, 102–105].

In our study, 5-Fluorouracil (5-FU) was chosen as a model guest molecule due to its simple structure and common usage in cancer treatments. Although standard chemotherapy is the most efficient method to deliver an anti-cancer drug into the body, because the chemicals are delivered through the blood circulation system of the body,

this process might kill healthy cells as well as the cancerous cells. The normal cells affected by this intravenous method might be blood cells, the cells in the mouth, stomach, bowel, and the hair follicles, resulting in low blood counts (anaemia, bleeding, infections), mouth sores, nausea, diarrhea or hair loss [145–147]. Alternatively, if physical control of the location of drug delivery were possible, these problems could be addressed.

6.2 Simulation Methodology

In order to understand how 5-FU could be encapsulated into the UiO-66 and how light interacts with this system, a set of simulations were performed (by Dr. Ravichandar Babarao). Simulations similar to this have been reported for CO₂ uptake and xylene adsorption at UiO-66 before [3, 78].

All calculations were performed using Vienna initio simulation package (VASP with a plane-wave energy cut-off of 600 eV and k-point sampling at the gamma-point). The interaction between core and valence electrons were described by the projector-augmented-wave (PAW) method and the generalized gradient approximation (GGA) of Perdew-Burke-Ernzerhof (PBE) was used to parameterize the exchange-correlation functional. The initial location of the drug in the primitive cell was obtained from classical simulated annealing technique. In the simulated annealing method, the temperature was lowered in accordance with a sequence of moves that allowed the gas molecule to reach a desirable configuration based on rotation, translation and repositioning with preset probabilities of occurrence. This process of heating and cooling the

system was repeated in several heating cycles to find the local minima. Forty heating cycles were performed where the maximum and final temperatures were 105 K and 100 K, respectively. The maximum loadings of 5-FU in perfect UiO-66 were estimated by grand canonical MC simulations using Materials Studio [148]. The configurational-bias algorithm was used rather than the conventional Metropolis technique, which is prohibitively expensive in sampling the phase space of big molecules. In configurational-bias algorithm, a molecule is grown atom-by-atom biasing energetically favorable configurations while avoiding overlap with other atoms [149–151]. The simulation box contained eight (2×2×2) unit cells for UiO-66, and the periodic boundary conditions were exerted in all three dimensions. The Lennard-Jones (LJ) interactions were evaluated using a spherical cut-off of 15 Å and the Coulombic interactions were calculated using the Ewald summation with a precision of 10^{-5} . The number of steps in the MC simulation was 10^7 steps for equilibration and subsequent 10^7 steps for production. Five types of trial moves were randomly attempted in the MC simulation, namely, translation, rotation, twist, regrowth, and exchange including creation and deletion with equal probability [152, 153].

The LJ parameters were adopted from the Universal Force Field (UFF) [154]. The Lorentz-Berthelot combining rules were used to calculate the cross LJ interaction parameters. For the Coulombic interaction, the atomic charges of 5-FU and UiO-66 were calculated based on the Qeq method as implemented in Material Studio (Figure 6.3) [155].

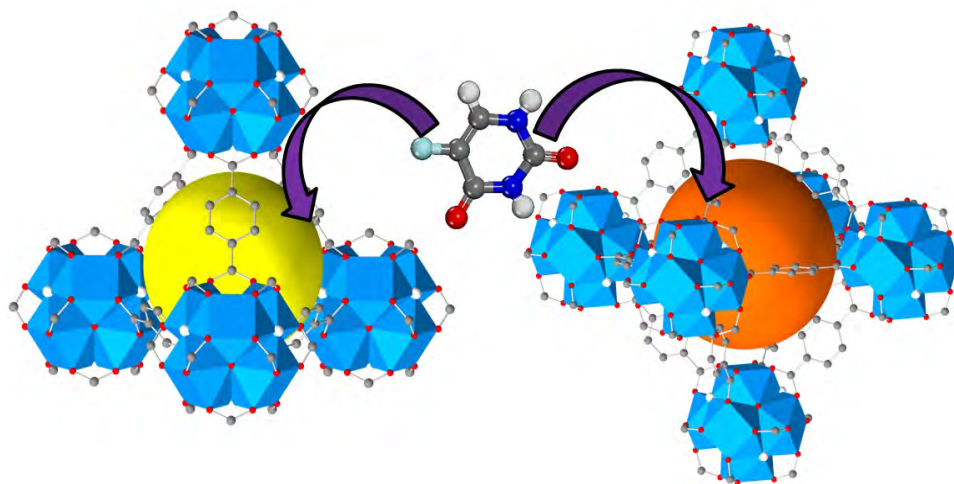


FIGURE 6.3: 5-FU loading @ UiO-66

Using dispersion-corrected semi-empirical DFT-D2 modelling/calculations, we were able to determine the optimized location of the drug confined within UiO-66, with preferential positioning near the triangular pore window of the tetrahedral cage (Figure 2-a) [156–158]. The predominant intramolecular interaction found between 5-FU and UiO-66 involved hydrogen bonding between the oxygen atom of the carbonyl group and the hydroxyl group present in the metal-oxide clusters ($\text{O-H}\dots\text{O}=\text{C}$) with a distance of ~ 1.82 Å. In addition, π - π interactions were found between 5-FU and the organic linkers of the UiO-66 framework. The simulation indicated the tetrahedral cages were the strong adsorption sites which filled first, followed by the octahedral cages present in the UiO-66 framework.

However, XRD results (*vide infra*) confirm that 5-FU does not have a regularised location within the pores. Figure 6.4 (Left) shows the DFT-D2 [159] optimized location of drug inside the tetrahedral cage of UiO-66 structure and Figure 6.4 (Right) with triangular pore windows show the characteristic drug/UiO-66 interacting distances reported in angstroms.

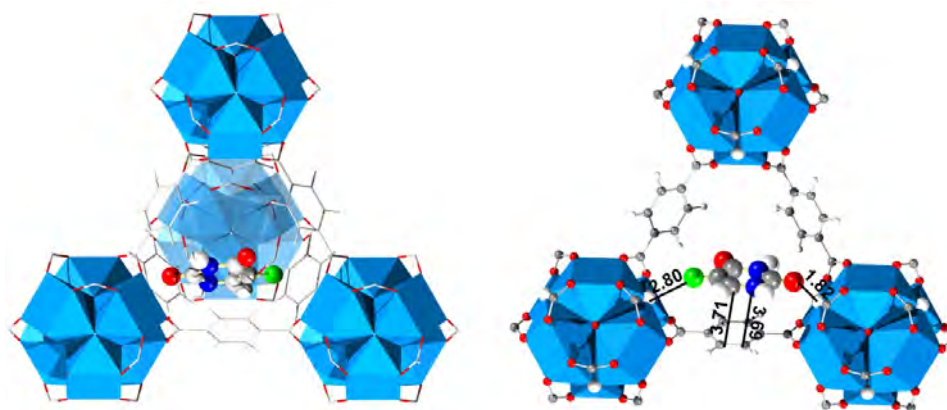


FIGURE 6.4: **Left** : Energy minimised incorporation of 5-FU, showing that it can fit within the pores, **Right**: Interacting distances in angstroms

6.3 5-FU Encapsulation into UiO-66 MOF

The UiO-66 MOF thin film synthesis method was described in Section 5.4.2. Here we used two methods for encapsulation of 5-FU into the MOF. 1- Impregnation and 2- Sublimation. For each method, a set of characterization techniques have been used to quantify if the drug is encapsulated in the UiO-66 successfully.

6.3.1 Encapsulation *via* Impregnation

It is reported in literature [160] that 5-FU is soluble in Dimethyl Sulfoxide (DMSO) in 5 mg/mL, Dimethyl Formamide (DMF) in 5 mg/mL, methanol in 1 mg/mL or hot water in 1 mg/mL.

In this study, solubility of 5-FU at different temperatures and in different solvents was tested. The highest solubility measured was 56 mg of 5-FU in 1.5 ml water at 56 °C. As Figure 6.5 shows, when using water as a solvent, distinct particles ranging from 500 nm to several μm can be seen. However in the case of ethanol as a solvent, no

particles can be seen and the material instead resembles a porous solid under the SEM conditions used.

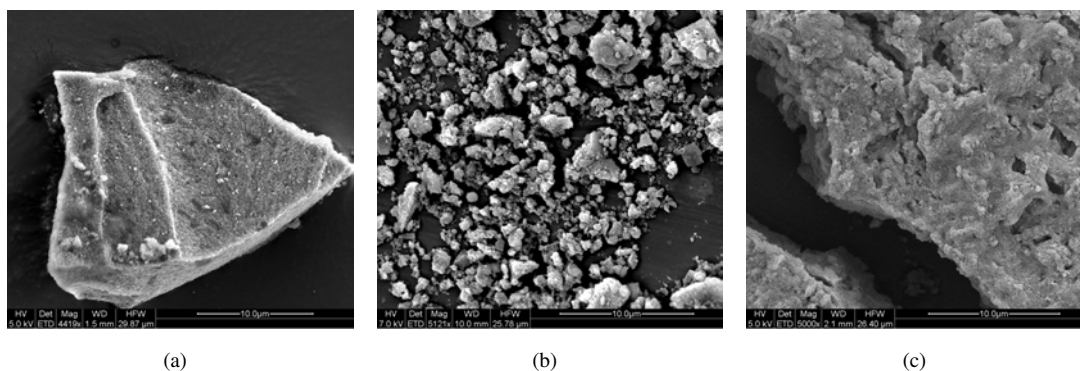


FIGURE 6.5: SEM images: a) Pure UiO-66 powder before impregnation, b) Impregnation of 5-FU in UiO-66 using water as a solvent, c) Impregnation of 5-FU in UiO-66 using ethanol as a solvent

Based on the finding, water is a suitable solvent to carry 5-FU, and so impregnation into UiO-66 MOF was commenced with water as a solvent. 650 mg of 5-FU was mixed with 15 ml of water and 500 mg of UiO-66 under constant stirring at 56 °C for 6 hours. The samples were then analyzed by FTIR as shown in Figure 6.6. The position of peaks in FTIR spectra of pure 5-FU and pure UiO-66 were compared with those in the FTIR spectra of impregnated sample. It was observed that all peaks specifically related to 5-FU were present in the 6 h sample. The data are summarized in Table 6.1 [134, 161, 162].

In order to confirm the quantity of compound in the 6 hours impregnated sample, TGA and XRD were carried out. The TGA result is shown in Figure 6.7 and XRD shown in Figure 6.8. The TGA pattern of 6 h sample is similar to UiO-66 pattern and there is no evidence of specific 5-FU weight loss at 270 °C in the 6 h sample pattern. Also, XRD pattern proves that 5-FU is not present in a crystalline form in the 6 h impregnated sample and UiO-66 main peak at 2θ angle of 7.4° has lost its sharp peak

intensity. Therefore it appears that impregnation by immersion of the UiO-66 in water dissolved 5-FU was not a suitable method for drug loading.

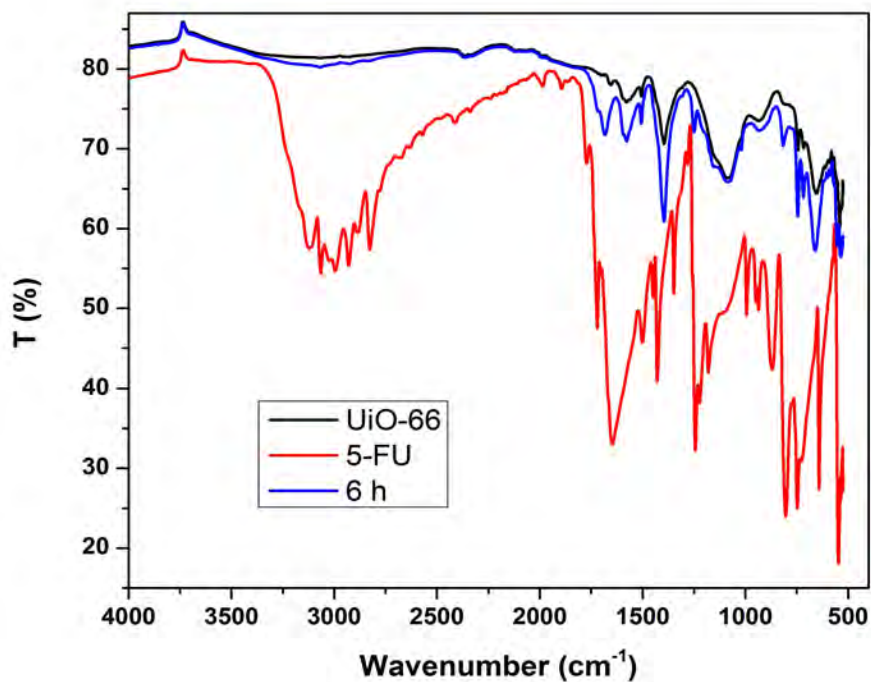


FIGURE 6.6: FTIR data for 6 hours impregnation sample

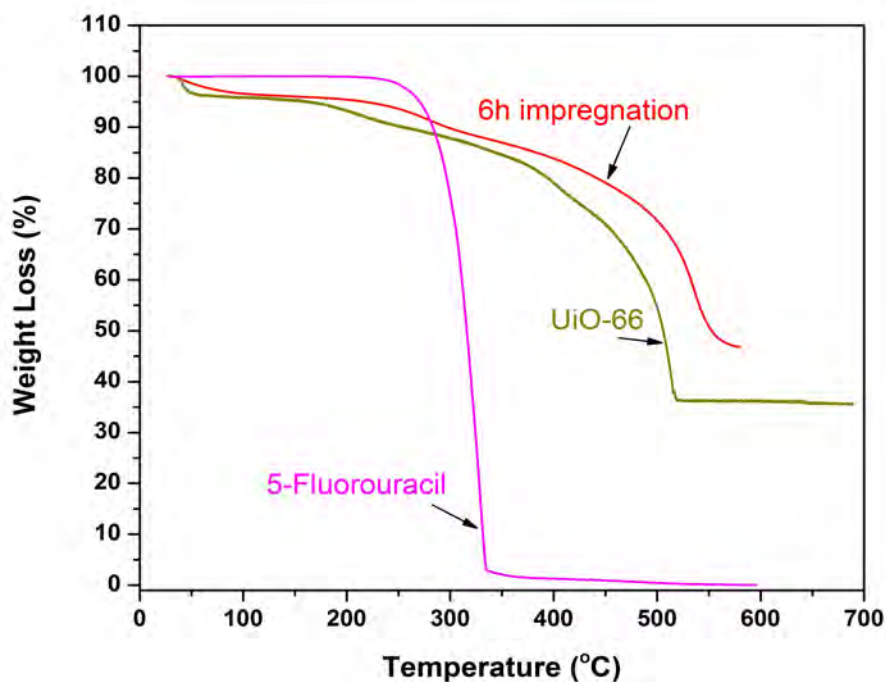


FIGURE 6.7: TGA curves for UiO-66, pure 5-FU and 6 h impregnation sample

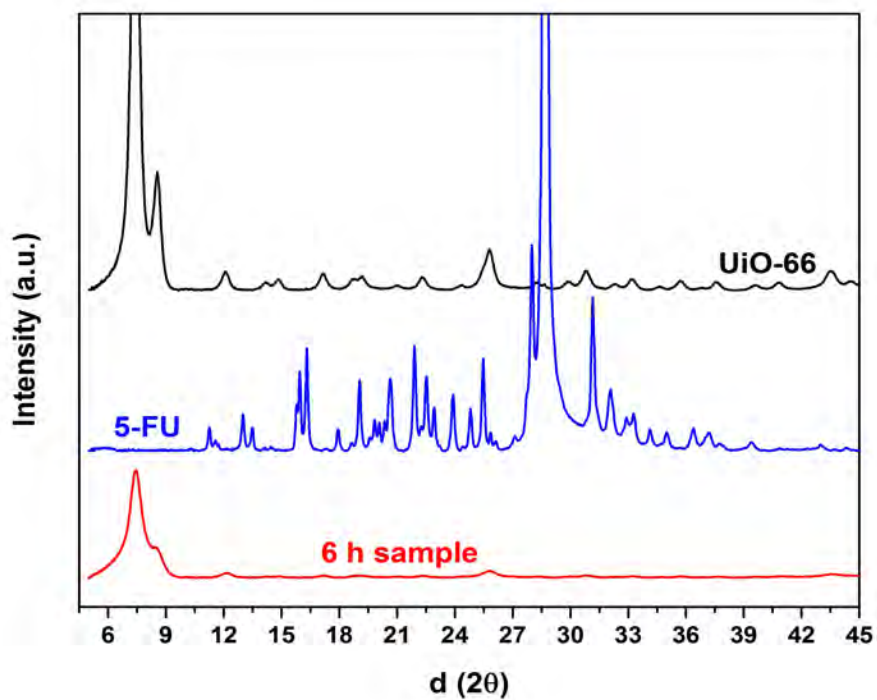


FIGURE 6.8: XRD for 6h sample in comparison with pure 5-FU and UiO-66

TABLE 6.1: FTIR spectra data

Group	5-FU (cm^{-1})	UiO-66 (cm^{-1})	6 h (cm^{-1})	Literature [134, 161, 162] (cm^{-1})
N-H (Stretching) Free	3172	-	-	3173
C=O(Stretch)	1720	-	1717	1721
C-N(stretch)	1646	-	-	1649
OCO asymmetric stretching (in- phase/antiphase)	-	1577, 1632	1577, 1631	1568, 1627, 1648
C-O	-	1395	1395	1400
νC_5F_{11}	1244	-	1249	1247
νN_3C_4 , νN_1C_6 , δC_6H , δN_1H	1180	-	1085	1182
νN_1C_2 , νC_2N_3	994	-	-	1000
νC_5F_{11} , $\delta N_1C_2N_3$	804	-	816	807
μ_3 -O stretching	-	744	745	730
Zr-(OC) symmetric stretching	-	662	661	622
νC_2N_1 , νC_2N_3 , νC_4C_5 , νC_6N_1	642	-	-	640
Zr-(OC) asymmetric stretching	-	574	554	560
$\delta C_2N_1C_6$	535	-	534	539

6.3.2 Encapsulation *via* Sublimation

5-FU loading into the UiO-66 MOF via sublimation was also investigated (as the sublimation process is simple and has the potential to lead to a high filling yield due to drug encapsulation in the gas phase and being free from any solvent molecules). As described in Chapter 3, this was carried out using a vacuum line and vacuum pump to sublime 5-FU. The sublimation temperature was set at 230 °C under 0.001 mbar pressure. The sublimation time was 30 minutes. 200 mg of 5-FU was placed at the closed end of a Pyrex tube with a 10 mm internal diameter with 100 mg of UiO-66 powder in an aluminium foil at the open end of the Pyrex tube. The tube was inserted into a furnace and heated up gradually to 230 °C (from room temperature to 120 °C at 5 °C/min, remaining at 120 °C for two hours in order to activate the UiO-66 MOF and then up to 230 °C at 9 °C/min). Figure 6.9 shows the sublimed 5-FU on the wall of the tube.

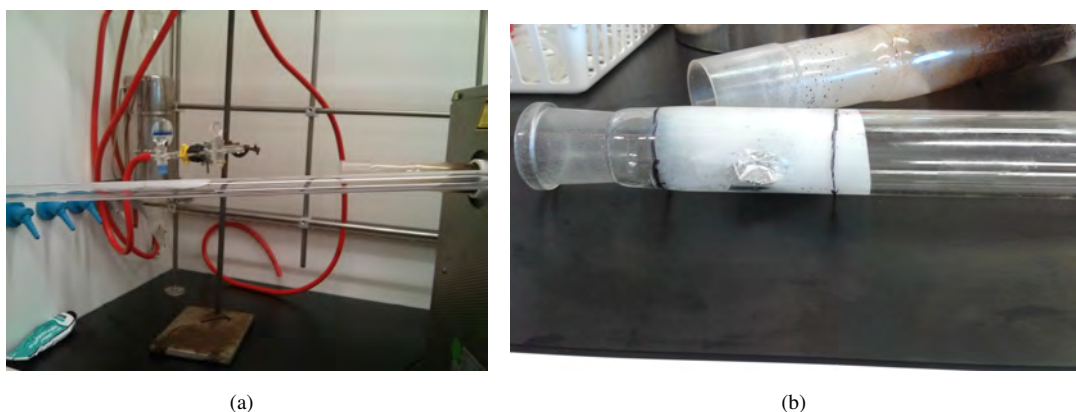


FIGURE 6.9: a) Sublimed 5-FU on the wall of the pyrex tube, b) 5-FU is sublimed at the wall of the tube, inside the aluminium foil boat is UiO-66 powder

Characterization methods were run to investigate successful sublimation of 5-FU in UiO-66 using the powder which was collected from the aluminium foil. The XRD

pattern in Figure 6.10 displays the characteristic peak at $2\theta = 28.6^\circ$ of the drug 5-FU, following its sublimation. This indicates the drug is present in significant quantities.

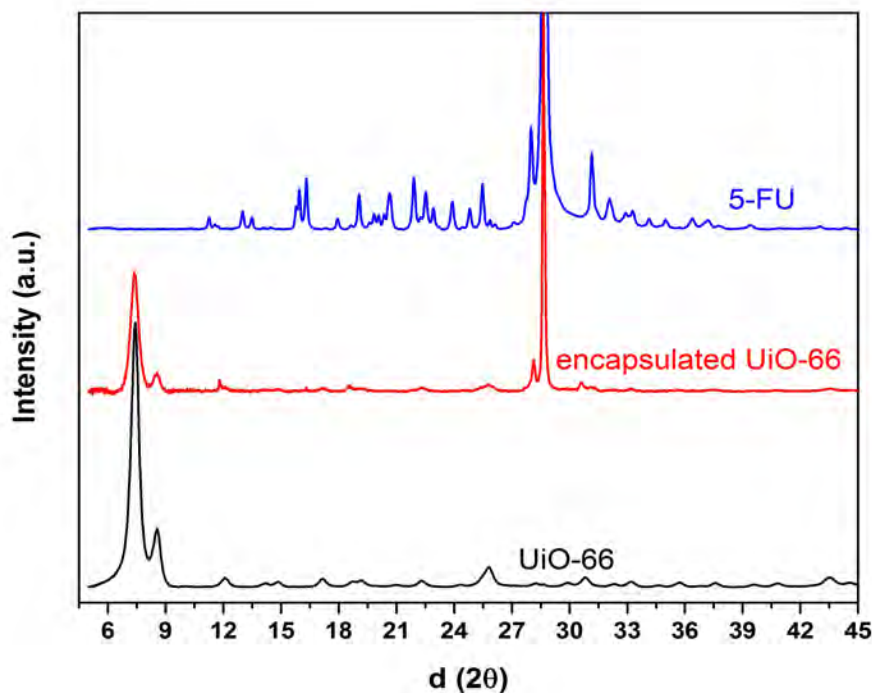


FIGURE 6.10: XRD for encapsulated 5-FU @ UiO-66 powder in comparison with pure 5-FU and UiO-66

Moreover, EDX analysis in Figure 6.11 shows the presence of fluorine from 5-FU and the corresponding zirconium of the framework. The TGA curve for the sublimed one in Figure 6.12 indicates that the pattern is similar to 5-FU with evidence of specific 5-FU weight loss at 260 °C, following the pattern of UiO-66 after 300 °C up to weight stabilization at 540 °C. Also, the drug incorporation has led to a lower percentage residue (4% of the starting weight).

Figure 6.13 shows the unmodified and encapsulated UiO-66 pore size distribution, revealing the appearance of a smaller pore which indicates that the drug is encapsulated mostly in the tetrahedral cage, but also in the octahedral cage, which in turn reduced the large peak at 12.7 Å upon loading with 5-FU. There was an observed shift in the smaller

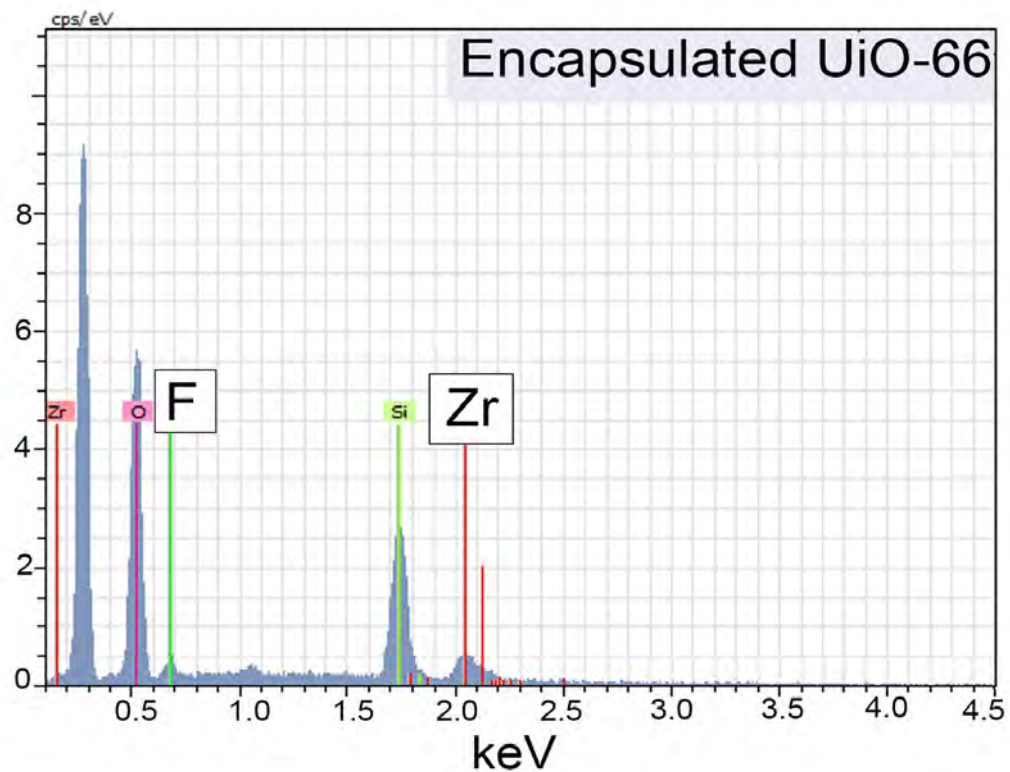


FIGURE 6.11: EDX spectra on UiO-66 powder after 5-FU encapsulation

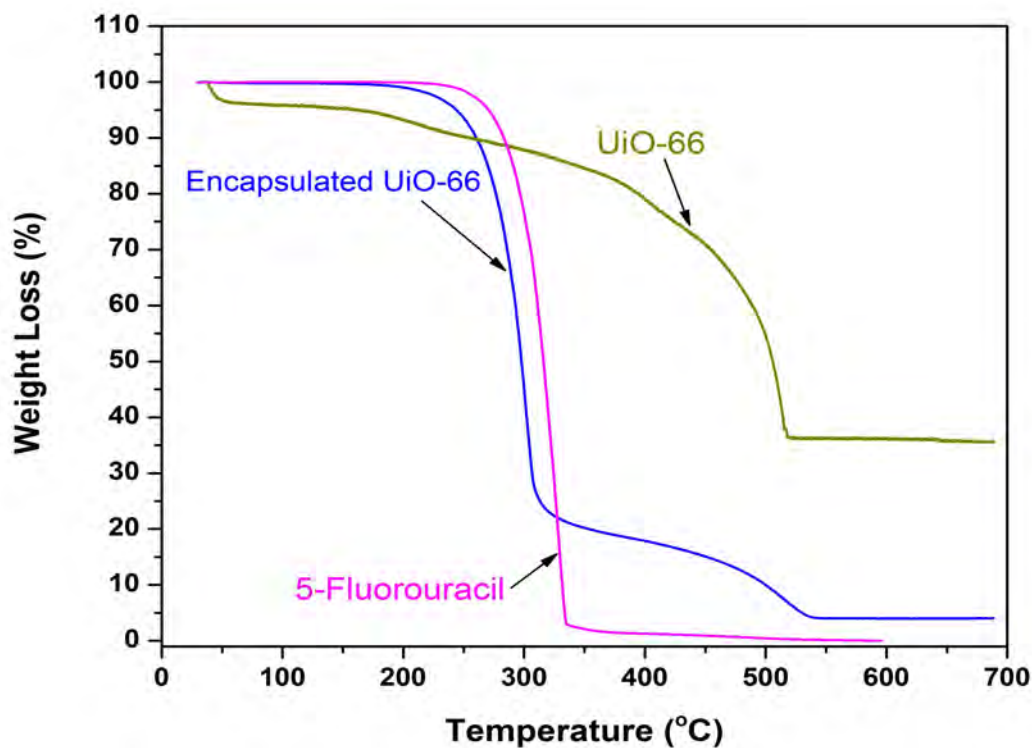


FIGURE 6.12: TGA curves for UiO-66, pure 5-FU and encapsulated 5-FU @ UiO-66 powder

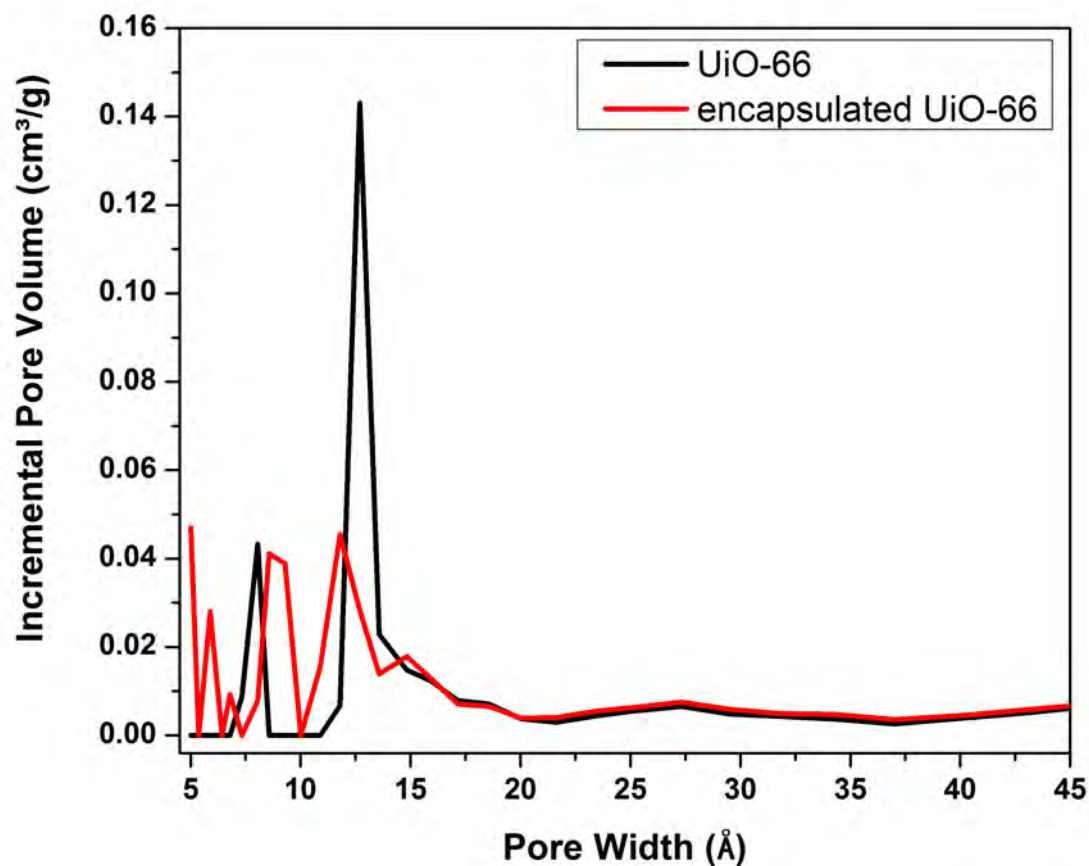


FIGURE 6.13: Pore size distribution of encapsulated 5-FU @ UiO-66

peak at 8 Å to 8.6 Å as a result of loading, which may be attributed to slight expansion of the smaller cages upon the uptake of the 5-FU into the larger pores found at 12.7 Å.

BET surface areas, calculated from Figures 6.14 and 6.15, shown in Table 6.2 illustrate that the sublimation process reduced the surface area as compared to the pure UiO-66.

TABLE 6.2: BET surface areas

Material	BET Surface Area ($\frac{m^2}{g}$)
UiO-66	1304
Encapsulated UiO-66	1057

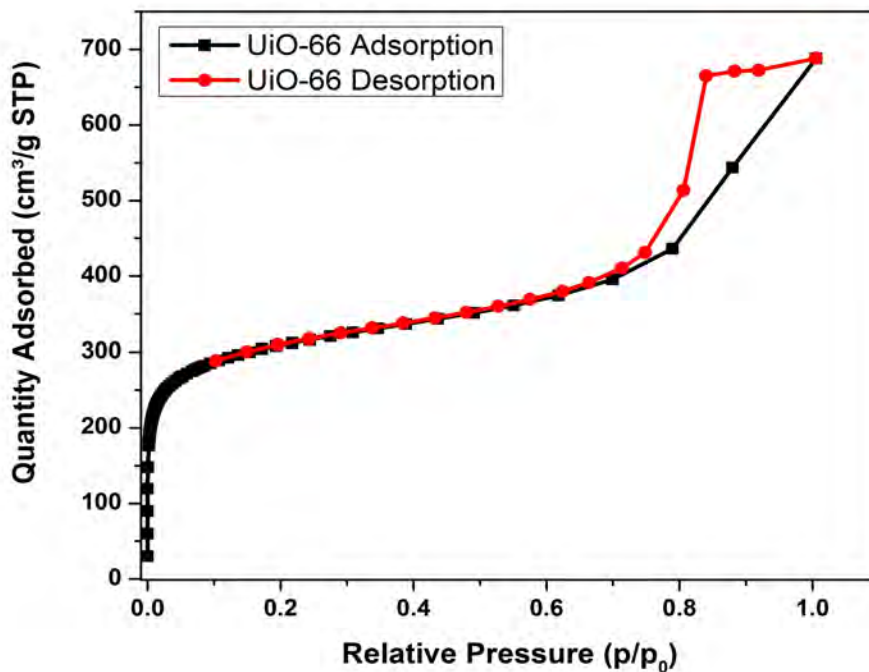


FIGURE 6.14: Pore size distribution of encapsulated 5-FU @ UiO-66

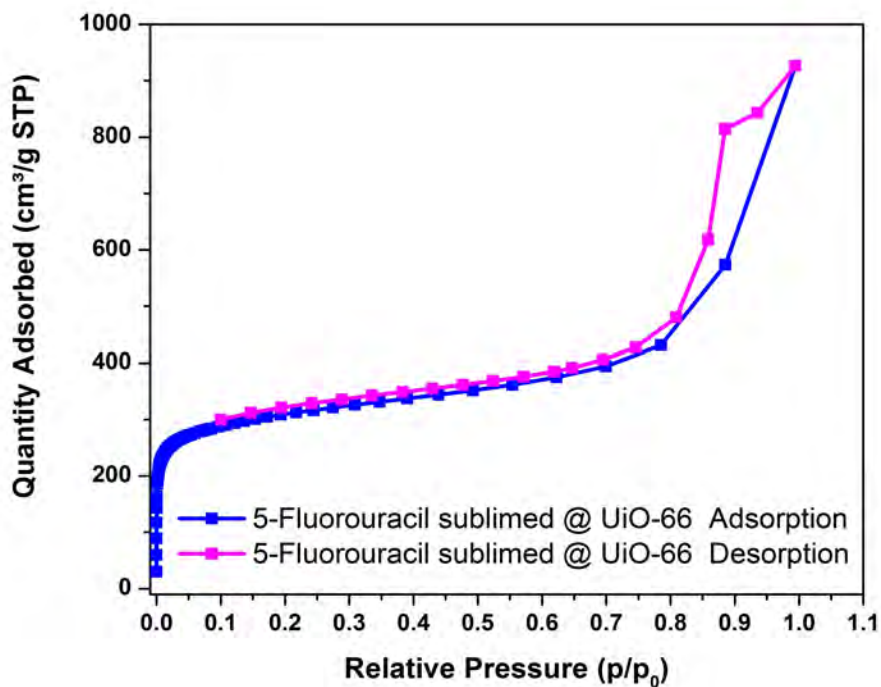


FIGURE 6.15: Encapsulated 5-FU @ UiO-66 nitrogen adsorption isotherm

In order to correlate the decrease in surface area to the amount of encapsulated 5-FU, we compared the theoretical and measured surface areas to identify how much drug is loaded inside the system. Since the incorporation of the drug in UiO-66 was done using sublimation method, it is hard to determine the amount of drug loaded inside the MOF. For this reason, we theoretically calculated the maximum amount of drug that can be loaded inside UiO-66. The maximum loading of drug calculated based on MC simulation is around 0.37 g of drug/g of material, equivalent to roughly 19 drug molecule per unit cell of UiO-66. The theoretical BET surface area for a perfect UiO-66 crystal is around $1000 \text{ m}^2/\text{g}$ based on N_2 as a probe molecule. To calculate the surface area upon encapsulation, we assume three drug molecules per unit cell of UiO-66. Further the surface area is predicted with drug encapsulated inside the MOF which is estimated to be around $822 \text{ m}^2/\text{g}$. The decrease in surface area is around 18.6%, which is close to the experimentally measured decrease in BET surface area, 19%, that is calculated based on the BET surface areas in Table 6.2. Based on this, we have 0.04 g of drug/g of material.

In summary, based on the observations of lost surface area, the identification of the 5-FU by XRD, EDX and TGA curves, it can be concluded that sublimation effectively loaded the drug inside the pores as desired, instead of depositing simply on the surfaces surrounding the particles.

6.3.2.1 Unit Cell Dimension Calculation

Unit cell dimension calculations were performed to further confirm successful encapsulation of 5-FU at UiO-66. The result is shown in Table 6.3. Based on this calculation, it

is concluded that the 5-FU can fit in the UiO-66 pores.

TABLE 6.3: Crystallographic data and important interatomic distances for encapsulated UiO-66

Material	a (Å)	b (Å)	c (Å)	α°	β°	γ°
UiO-66	20.770 \pm 0.05	-	-	-	-	-
5-FU	9.211 \pm 0.004	12.643 \pm 0.007	8.783 \pm 0.004	80.682 \pm 0.022	90.800 \pm 0.022	98.717 \pm 0.025
Encapsulated UiO-66	20.900 \pm 0.04 and 9.218 \pm 0.007	12.665 \pm 0.005	8.791 \pm 0.008	80.757 \pm 0.061	90.837 \pm 0.049	98.605 \pm 0.064

6.4 Determining UiO-66 Stability in Different Biological Media

In order to work in applications such as drug delivery, UiO-66 needs to be stable in different solutions relevant to biological media. As described in Chapter 3, this was carried out by testing UiO-66 in the presence of water, bovine serum albumin (BSA) with pH = 7.4, phosphate buffer solution (PBS) with pH = 7.4 and acetate buffer with pH = 5 for 24 hours under constant stirring at 37 °C (body temperature). After centrifuge, samples were analyzed by XRD to observe the crystallinity of the UiO-66. The XRD result in Figure 6.16 shows patterns for the UiO-66 in the various environments. The peaks of the MOF remain unchanged indicating no breakdown in the crystallinity of the UiO-66. However this is not the case of PBS which a sharp decline in the peak

height was observed showing that there was not enough UiO-66 crystal compared to the original UiO-66 due to high affinity order between Zr and phosphate [163].

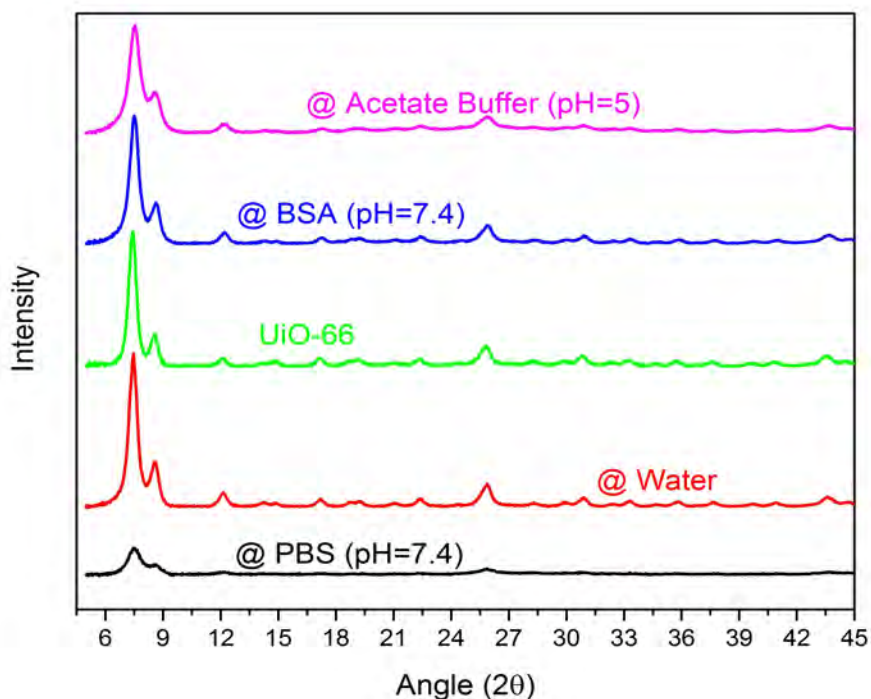


FIGURE 6.16: XRD data for UiO-66 in different biological media

6.5 Light Triggered Release of 5-FU from UiO-66 Thin Film

After successfully validating the sublimation technique to encapsulate the 5-FU into UiO-66, experiments were designed to investigate light triggered release from the coated optical fibres. UiO-66 was coated at the end-face of optical fibre followed by the encapsulation of 5-FU via the sublimation approach. Figure 6.17 shows a bare optical fibre sample in which 5-FU is sublimed on and around the end-face.

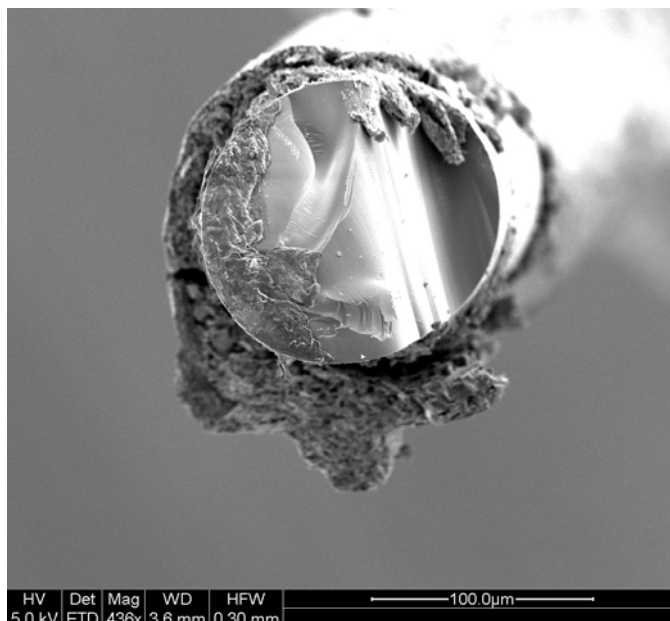


FIGURE 6.17: SEM image of a bare optical fibre after 5-FU sublimation

During the sublimation process for the sample with UiO-66 thin film, 5-FU molecules were sublimed on the surface of the UiO-66 film and also on the adjacent surface of the optical fibre (as shown for the bare optical fibre in Figure 6.17). So after encapsulation and before turning on the light source, the optical fibre was immersed for 12 minutes in water/BSA solution at 37 °C in order to wash away excess 5-FU from the surface and surrounding area of the optical fibre tip. The release samples were taken every minute, where in each case the removed sample vial was replaced with a fresh one. Figure 6.18 shows the large peak observed immediately after contact with the water reveals the release of excess 5-FU attached on the surface of the optical fibre.

As shown in Figure 6.19, after 12 minutes of initial washing and initial release of 5-FU from the surface of the optical fibre, no 5-FU was detectable in the surrounding liquid as indicated by light absorbance at 265 nm. Upon confirming no further loss from the material, at 13-15 minutes the 800 nm, 1050 nm and 1550 nm light sources were used to observe whether light triggered release of 5-FU into the surrounding liquid

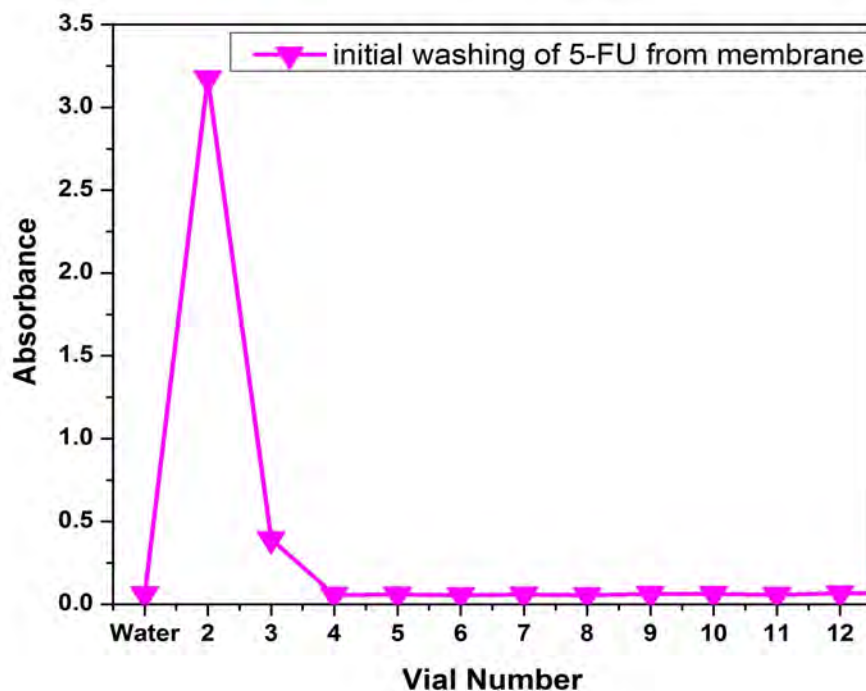


FIGURE 6.18: Light absorbance at 265 nm of the samples collected from immersing the encapsulated UiO-66 optical fibres in water/BSA

solution was possible. Upon initiating this light via the optical fibre, 5-FU was detected in the solution, but only with the 1050 nm source. The controlled release of 5-FU captured inside the UiO-66 cage structure was confirmed. This release is wavelength dependent and there is no release for 800 nm and 1550 nm wavelengths.

After turning the light on in vials 13-15 minutes, the light source was turned off for another 12 minutes and was turned on again for vials 26-28 minutes. As it can be seen in Figure 6.19 no more release was observed. This indicates that 5-FU was completely released upon the initial light exposure.

Based on density functional theory calculations, the binding energy of one drug molecule with UiO-66 is estimated to be around 100 kJ/mol which is equivalent to 1197 nm. By tuning the wavelength to 1050 nm, UiO-66 was sufficiently activated to overcome the enthalpy of adsorption for 5-FU, allowing the in situ release.

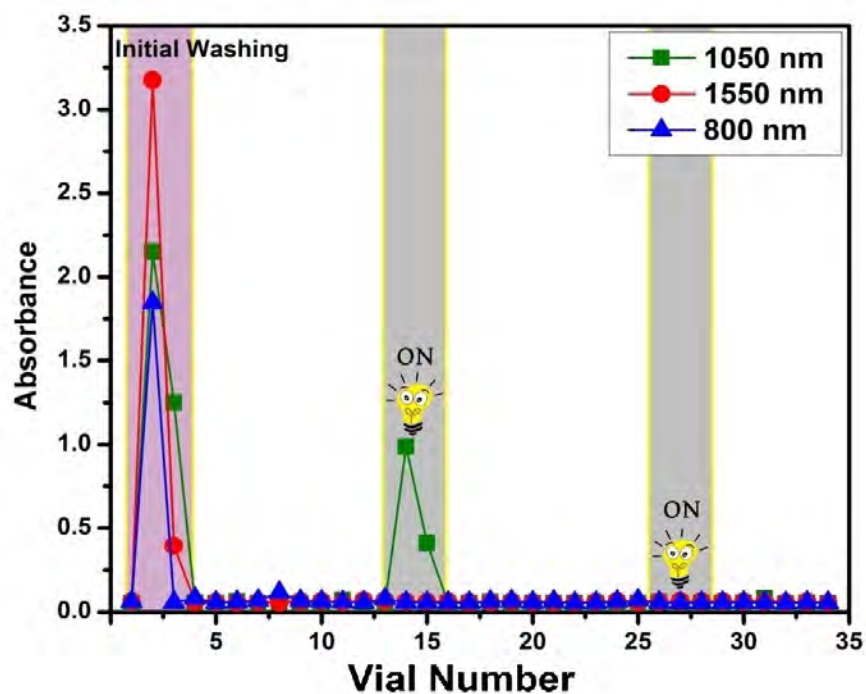


FIGURE 6.19: Light absorbance at 265 nm of solutions surrounding the optical fibre triggered at various light wavelengths

6.5.1 Release Amount

In order to calculate the amount of drug which is released due to light, the peak intensity in Figure 6.19 was compared with the calibration curve in Figure 3.8. Figure 6.20 shows the amount of drug released (star icons) due to the light triggered effect at 1050 nm using a 5-FU calibration curve with r-squared fit of 99.8%. The released peak intensities from a microplate photometer were determined to be 106, 110 and 115 μM for each repeat sample.

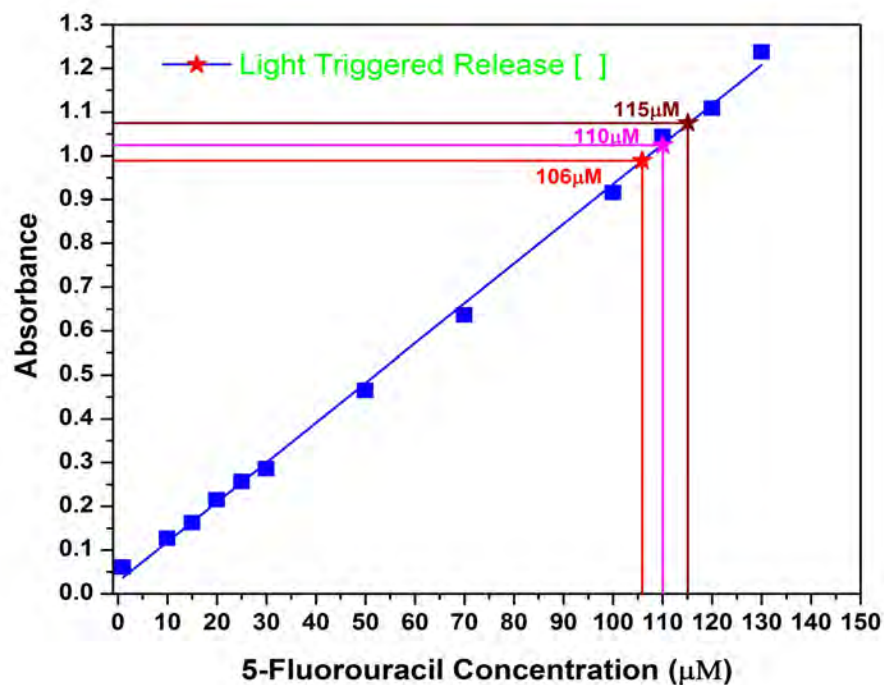


FIGURE 6.20: Interpolating release concentration with line of best fit

6.6 Efficiency of the Process

After successful validation of the triggered release of 5-FU from the optical fibre, the efficiency of this method can now be assessed for intravenous infusion for chemotherapy. It should be noted that this release rate is only for one optical fibre, it is possible to make an array of drug-loaded optical fibres for their intended application [164, 165]. Figure 6.21 shows a schematic illustration of an optical fibre array. The fibre bundle can be inserted into a specialized catheter (tube) for protection and then placed in proximity to the specified tumorous area in the body [18–20, 166–169].

However, maximum 5-FU administration dose depends on the patient's age, weight, general health, type/stage of cancer, comorbidity and kidney function [170] and the

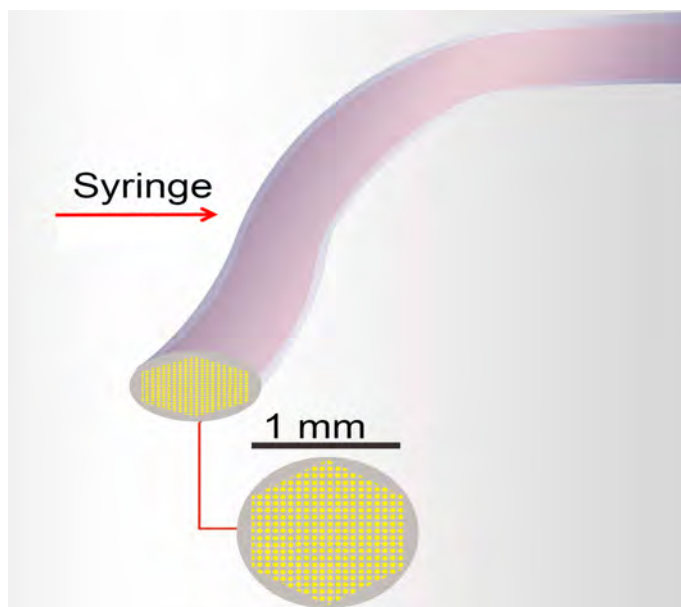


FIGURE 6.21: A schematic illustration of an optical fibre array

standard duration of treatment is based on 5-FU treatment regime (5-FU as a sole treatment or in combination with other medications) [171]. For instance, in intravenous infusion of 5-FU to adult patients, the maximum recommended daily dose [172, 173] is 800 mg in 300-500 ml of 5% glucose solution and is administered over 4 hours. This dose is equivalent to $12.3 \text{ mM} < [5\text{-FU}] < 20.5 \text{ mM}$ and in comparison with the above average release rate of $110 \mu\text{M}$ for one optical fibre in a vial volume of $300 \mu\text{L}$, we need approximately 111 to 186 separate SMF-28 optical fibres to get the same effect in one minute as above from intravenous infusion.

6.7 Conclusion and Future Work

In this chapter a new method of delivering medicine with controllable release was discussed. Mathematical simulation was run to investigate the location of 5-FU at UiO-66 cage and their possible chemical interactions. Moreover, it was noted that impregnation

is not a suitable method for encapsulation; however, the sublimation method demonstrated a good uptake of the drug with reasonable agreement between experiment and simulation. By tuning the light wavelength, one can trigger release of a medicine from the UiO-66 material into the surrounding medium, albeit that there are significant limitations on when this approach can be used.

Considering this proof-of-concept work, the large number of fibres or frequency of use could be reduced with further improvement, for example by using larger core diameter optical fibres (e.g. multimode step-index fibres with 1500 μm of core diameter) or further explore opportunities to increase the load quantity. However, other types of MOFs with larger pore sizes could be used. These new MOFs can store larger molecules in their pores (e.g. Doxorubicin) which was impossible in this project to encapsulate in UiO-66 due to its small pore size. Also, there is another option of functionalising the MOFs with choosing different ligands and/or ligand exchange. In this case, specific molecules could be attached/encapsulated to these MOFs and then released by a right light wavelength.

Chapter 7

Conclusions and Future Work

7.1 Summary of the Thesis Outcome

An effective approach to developing optical fibre chemical sensors is to coat optical fibres with nanoporous functional materials. A variety of materials, including polymers, mesoporous silica, metal oxides, silicon, sol gel and zeolites have been researched either as selective adsorbing overcoats or as immobilizers for dispersing of chemically sensitive materials on optical substrates. Among these, zeolites have received much interest in recent years and are used to develop highly selective adsorbents and membranes for molecular separations and electrode modification to obtain enhanced sensitivity of electrochemical sensors. However, zeolite's small pore size does not allow its use for larger molecular adsorption or drug delivery applications. In order to fulfill this problem, in this research, a new type of nanoporous materials (MOFs) were used as a thin film at the end of optical fibre, firstly to capture specific contaminants from water and secondly

for the triggered release of anti-cancer medicine using light via optical fibre. The key findings of this research are summarized below:

Firstly, MFI-type zeolite thin films were grown on the cleaved end-face of a single mode optical fibre using *in situ* hydrothermal synthesis method. The zeolite-fibre device was used to study the molecular sorption induced optical refractive index and optical thickness changes for ammonium, 4-Aminopyridine, methanol, ethanol and 2-propanol as model systems. A mathematical procedure was established for the calculation of the optical thickness from the experimentally measured Fabry-Perot interference data. It was found that the zeolite refractive index and optical length increases with increasing the loading of sorbate molecules (e.g. ammonium) in the zeolite cavities. These phenomena are caused by the increase in zeolite overall density and lattice expansion upon molecular sorption into the zeolitic pores. The definitive relationships between the optical properties and the adsorption are necessary for use of the zeolite-fibre device as a sensor for quantitative chemical detections. The sensor exhibited a clear correlation between analyte concentration and optical output that allows quantitative measurement with high sensitivity.

Secondly, optical quality MOF thin films were integrated, for the first time, with structured optical fibre substrates to develop MOF-fibre sensors. In the MOF-fibre structure, the UiO-66 thin film has multi functions to act as an effective analyte collector or concentrator and an optical actuator. The MOF-fibre sensor operates by measuring the shift of wavelength in its reflected spectrum. The shift of wavelength in the interference spectrum is caused by the UiO-66 refractive index variation as a function of the adsorption of analyte molecules into UiO-66 pores. The end-face reflective sensor

was also demonstrated for detection of Rhodamine-B and 4-Aminopyridine dissolved in water. The sensor exhibited quantitative measurement capability for Rhodamine-B dissolved in water as the sensor signal decreased monotonically with an increase of chemical concentration in the tested concentration range. The sensor's response to a 0.1 mM Rhodamine-B concentration indicated that the sensor's detection limit could be at lower mM levels. At low concentration the sensor's response to 4-Aminopyridine dissolved in water was much less accurate than that of Rhodamine-B dissolved in water and 4-Aminopyridine was not detected by this method in water.

Rationally designed drug delivery system enables us to precisely control drug release rates for prolonged duration and sometimes help targeting drugs, such as anti-cancer medicine, to specific body sites. With taking advantage of MOF-fibre structure, we successfully applied sublimation technology for the anti-cancer drug, 5-Fluorouracil, encapsulation into UiO-66 cage. The design and development of this technique posed various challenges involving optimization of drug entrapment, release from the UiO-66 cage, stability evaluation and utility as a safer alternative to conventional chemotherapy method. The basic idea was to reduce the toxicity of the cytotoxic anti-cancer drug by making use of its administration to the body via triggered release by means of an optical fibre without compromising the clinical efficacy. This drug delivery system demonstrated a great potential in this regard with delivering 110 μM of 5-FU in less than one minute with just one optical fibre. However, the major issue limiting its utility is the released drug dose which can be overcome by using larger core diameter optical fibres.

In short, this study presented a novel thin film based optical fibre chemical sensor and actuator for water evaluation and anti-cancer drug delivery. This proposed device will help promote a more promising method for sensing harmful chemicals in water and delivering toxic medicines to the rural areas of the body.

7.2 Future Directions

As the science is growing, new methods and materials must be discovered. Further studies could consider the following approaches:

- Investigating how the UiO-66 structure could be improved via functionalising with other ligands for various contaminant selectivities and sensitivities;
- Considering alternative MOF structures to capture larger anti-cancer molecules;
- Using different types of optical fibres to minimise loss or having larger surface area to coat with thin film and hence heavy encapsulation of anti-cancer medicine into thin film which leads to higher dose release;
- Photonic crystal fibres (PCF), which are being used in analyte detection as they allow infiltration, could be investigated as an alternative (possibly improving the ability to detect lower concentrations).

Appendix A

Signal Processing Algorithm

A.1 Matlab Coding for Signal Processing

The procedure described in Section 3.4.4 involves the following Matlab coding:

```
clc;
clear all;
close all;
filename = '.....xlsx';
RIS = xlsread(filename,'B:B');
Wavelength = xlsread (filename, 'A:A');
ArrayL = length(RIS);
RIS = RIS - mean(RIS);
[C, L] = wavedec(RIS,6,'db7');
cA = wrcoef('a',C,L,'db7',6);
cD5 = wrcoef('d',C,L,'db7',5);
cD4 = wrcoef('d',C,L,'db7',4);
cD3 = wrcoef('d',C,L,'db7',3);
cD2 = wrcoef('d',C,L,'db7',2);
cD1 = wrcoef('d',C,L,'db7',1);
DenoisedRIS = cA + cD5 + cD6;
figure,
plot(Wavelength,RIS,Wavelength,DenoisedRIS);
Lambda0 = (((Wavelength(end) + Wavelength(1)) / 2) / nIndex) * 10-9;
LambdaS = (Wavelength(end) - Wavelength(1))/ArrayL;
```

```
Fs = 1 / LambdaS;
N = 100000;
freq = linspace(0,Fs,N);
fftedRIS = fft(DenoisedRIS,N);
figure,
plot(freq(1:floor(end/10)),abs(fftedRIS(1:floor(end/10))))[maxAm, ind]=max(abs(fftedRIS));
hold on, plot(freq(ind),maxAm,'r*')
legend('Freq Spectrum', 'Fundamental Freq')
th = .....;
[pks, dep, pidx, didx] = peakdet(abs(fftedRIS),th);
for i=1 : (length(pidx) / 2)
T(i) = (1 / freq(pidx(i))) * 10-9
d(i) = (Lambda02) / (2 * T(i));
text(Fs/20, maxAm/2-(i*maxAm)/10, num2str(d(i)));
end
A1 = cos(2*pi*freq(pidx(1)) .* Wavelength);
A2 = cos(2*pi*freq(pidx(2)) .* Wavelength);
figure,
plot(Wavelength,A1,Wavelength,A2);
```


References

- [1] Kristina Konstas, Kim F. Taupitz, David R. Turner, Danielle F. Kennedy, and Matthew R. Hill. A new family of zinc metal-organic framework polymorphs containing anthracene tetracarboxylates. *CrystEngComm*, 16:8937–8940, 2014.
- [2] Ravichandar Babarao, Campbell J. Coghlan, Damien Rankine, Witold M. Bloch, Gemma K. Gransbury, Hiroshi Sato, Susumu Kitagawa, Christopher J. Sumby, Matthew R. Hill, and Christian J. Doonan. Does functionalisation enhance co₂ uptake in interpenetrated mofs? an examination of the irmof-9 series. *Chem. Commun.*, 50:3238–3241, 2014.
- [3] Cher Hon Lau, Ravichandar Babarao, and Matthew R. Hill. A route to drastic increase of co₂ uptake in zr metal organic framework uio-66. *Chem. Commun.*, 49:3634–3636, 2013.
- [4] Richelle Lyndon, Kristina Konstas, Bradley P. Ladewig, Peter D. Southon, Prof Cameron J. Kepert, and Matthew R. Hill. Dynamic photo-switching in metal-organic frameworks as a route to low-energy carbon dioxide capture and release. *Angewandte Chemie International Edition*, 52(13):3695–3698, 2013.

- [5] Seda Keskin and Seda Kzlel. Biomedical applications of metal organic frameworks. *Industrial and Engineering Chemistry Research*, 50(4):1799–1812, 2011.
- [6] Patricia Horcajada, Tamim Chalati, Christian Serre, Brigitte Gillet, Catherine Sebrie, Tarek Baati, Jarrod F. Eubank, Daniela Heurtaux, Pascal Clayette, Christine Kreuz, Jong-San Chang, Young Kyu Hwang, Veronique Marsaud, Phuong-Nhi Bories, Luc Cynober, Sophie Gil, Gerard Ferey, Patrick Couvreur, and Ruxandra Gref. Porous metal-organic-framework nanoscale carriers as a potential platform for drug delivery and imaging. *Nat Mater*, 9(2):172–178, 2010. 10.1038/nmat2608.
- [7] Chunbai He, Kuangda Lu, Demin Liu, and Wenbin Lin. Nanoscale metal organic frameworks for the co delivery of cisplatin and pooled sirnas to enhance therapeutic efficacy in drug resistant ovarian cancer cells. *Journal of the American Chemical Society*, 136(14):5181–5184, 2014. PMID: 24669930.
- [8] Mahesh Uttamlal and David R. Walt. A fibre optic carbon dioxide sensor for fermentation monitoring. *Nat Biotech*, 13(6):597–601, 1995. 10.1038/nbt0695-597.
- [9] S. T. Vohra, F. Bucholtz, G. M Nau, K. J. Ewing, and I. D. Aggarwal. Remote detection of trichloroethylene in soil by a fibre optic infrared reflectance probe. *Appl. Spectrosc.*, 50(8):985–990, Aug 1996.
- [10] Artur Dybko, Wojciech Wrblewski, Ewa RoÅniecka, Krzysztof Pozniakb, Janusz Maciejewski, Ryszard Romaniuk, and Zbigniew Brzozka. Assessment

- of water quality based on multiparameter fibre optic probe. *Sensors and Actuators B: Chemical*, 51(13):208 – 213, 1998.
- [11] H. Steiner, M. Jakusch, M. Kraft, M. Karlowatz, T. Baumann, R. Niessner, W. Konz, A. Brandenburg, K. Michel, C. Boussard-Pldel, B. Bureau, J. Lucas, Y. Reichlin, A. Katzir, N. Fleischmann, K. Staubmann, R. Allabashi, J. M. Bayona, and B. Mizaikoff. In situ sensing of volatile organic compounds in groundwater: First field tests of a mid-infrared fibre optic sensing system. *Applied Spectroscopy*, 57(6):607–613, 2003.
- [12] Irwin Schneider, G. Nau, T.V.V. King, and I. Aggarwal. Fibr optic near-infrared reflectance sensor for detection of organics in soils. *Photonics Technology Letters, IEEE*, 7(1):87–89, Jan 1995.
- [13] Dianna S. Blair and Jeanne Bando. Quantitative monitoring of volatile organic compounds in water using an evanescent fiber optic chemical sensor. *Environmental Science and Technology*, 32(2):294–298, 1998.
- [14] Mahmoud A. El-Sherif, Jianming Yuan, and Alan Macdiarmid. Fiber optic sensors and smart fabrics. *Journal of Intelligent Material Systems and Structures*, 11(5):407–414, 2000.
- [15] Stephen J. Mihailov. Fibre bragg grating sensors for harsh environments. *Sensors*, 12(2):1898, 2012.
- [16] Karen S. Bronk, Karri L. Michael, Paul. Pantano, and David R. Walt. Combined imaging and chemical sensing using a single optical imaging fibre. *Analytical Chemistry*, 67(17):2750–2757, 1995.

- [17] Y. Chang and C.K. Ting. Spinal cord's epidural space detection by using fibre optic technology, April 16 2009. US Patent App. 12/113,691.
- [18] Seng Khoon Teh, Wei Zheng, Khek Yu Ho, Ming Teh, Khay Guan Yeoh, and Zhiwei Huang. Near-infrared raman spectroscopy for optical diagnosis in the stomach: Identification of helicobacter-pylori infection and intestinal metaplasia. *International Journal of Cancer*, 126(8):1920–1927, 2010.
- [19] Shiyamala Duraipandian, Jianhua Mo, Wei Zheng, and Zhiwei Huang. Near-infrared raman spectroscopy for assessing biochemical changes of cervical tissue associated with precarcinogenic transformation. *Analyst*, 139:5379–5386, 2014.
- [20] Mads Sylvest Bergholt, Wei Zheng, Kan Lin, Jianfeng Wang, Hongzhi Xu, Jianlin Ren, Khek Yu Ho, Ming Teh, Khay Guan Yeoh, and Zhiwei Huang. Characterizing variability of in vivo raman spectroscopic properties of different anatomical sites of normal colorectal tissue towards cancer diagnosis at colonoscopy. *Analytical Chemistry*, 87(2):960–966, 2015. PMID: 25495077.
- [21] T.P. Jenkins, J.I. Eldridge, S.W. Allison, R.P. Howard, E.H. Jordan, and D.E. Wolfe. An experimental investigation of luminescence lifetime thermometry for high temperature engine components using coatings of yag:dy and yag:tm. volume 495, pages 47–58, 2013.
- [22] Otto S. Wolfbeis. Fiber-optic chemical sensors and biosensors. *Analytical Chemistry*, 80(12):4269–4283, 2008. PMID: 18462008.
- [23] Xu-Dong Wang and Otto S. Wolfbeis. Fibre optic chemical sensors and biosensors (20082012). *Analytical Chemistry*, 85(2):487–508, 2013. PMID: 23140530.

- [24] Soichi Otsuki, Kimihiro Adachi, and Takahisa Taguchi. A novel fiber-optic gas-sensing configuration using extremely curved optical fibers and an attempt for optical humidity detection. *Sensors and Actuators B: Chemical*, 53(12):91 – 96, 1998.
- [25] Cndido Bariin, Ignacio R Matas, Francisco J Arregui, and Manuel Lpez-Amo. Optical fiber humidity sensor based on a tapered fiber coated with agarose gel. *Sensors and Actuators B: Chemical*, 69(12):127 – 131, 2000.
- [26] Sunil K. Khijwania, Kirthi L. Srinivasan, and Jagdish P. Singh. Performance optimized optical fiber sensor for humidity measurement. *Optical Engineering*, 44(3):034401–034401–7, 2005.
- [27] M. Batumalay, S.W. Harun, F. Ahmad, R.M. Nor, N.R. Zulkepely, and H. Ahmad. Study of a fiber optic humidity sensor based on agarose gel. *Journal of Modern Optics*, 61(3):244–248, 2014.
- [28] Shiquan Tao, Lina Xu, and Joseph C. Fanguy. Optical fiber ammonia sensing probes using reagent immobilized porous silica coating as transducers. *Sensors and Actuators B: Chemical*, 115(1):158 – 163, 2006.
- [29] Shau Shao, Yu Hung, and Shiquan Tao. Simultaneous monitoring of electrical resistance and optical absorbance signals of a fiber optoelectrode for multiple gas sensing, 2013.
- [30] Paul R. Ohodnicki Jr., Sittichai Natesakhawat, John P. Baltrus, Bret Howard, and Thomas D. Brown. Characterization of optical, chemical, and structural changes

- upon reduction of solgel deposited SnO_2 thin films for optical gas sensing at high temperatures. *Thin Solid Films*, 520(19):6243 – 6249, 2012.
- [31] Cesar Elosua, Ignacio R. Matias, Candido Barriain, and Francisco J. Arregui. Volatile organic compound optical fiber sensors: A review. *Sensors (Basel, Switzerland)*, 6(11):1440–1465, 2006.
- [32] S.-M. Lee, S.-W. Jang, S.-H. Lee, J.-H. Kim, S.-H. Kim, and S.-W. Kang. Measurement of basic taste substances by a fiber optic taste sensor using evanescent field absorption. *Sensors and Materials*, 14(1):11–21, 2002.
- [33] Xuemei Hu and Shiquan Tao. An optical fiber H_2O_2 sensing probe using a titanium(IV) oxyacetylacetonate immobilized nafion coating on a bent optical fiber probe. *Sensors Journal, IEEE*, 11(9):2032–2036, Sept 2011.
- [34] Andrew M. King, Nathan B. Menke, Kenneth D. Katz, and Anthony F. Pizon. 4-aminopyridine toxicity: a case report and review of the literature. *Journal of Medical Toxicology*, 8(3):314–321, 2012.
- [35] Ramesh C. Gupta. *Veterinary Toxicology*. Academic Press, 2nd edition.
- [36] K. Neil Harker. Ammonium sulfate effects on the activity of herbicides for selective grass control. *Weed Technology*, 9(2):pp. 260–266, 1995.
- [37] N.P. Cheremisinoff. *Industrial Solvents Handbook, Revised And Expanded*. Chemical Industries. Taylor & Francis, 2003.
- [38] Susan E. Powers, Craig S. Hunt, Stephen E. Heermann, Henry X. Corseuil, David Rice, and Pedro J. J. Alvarez. The transport and fate of ethanol and BTEX in

- groundwater contaminated by gasohol. *Critical Reviews in Environmental Science and Technology*, 31(1):79–123, 2001.
- [39] INTERNATIONAL PROGRAMME ON CHEMICAL SAFETY. Environmental health criteria 103, 2-propanol, 1990.
- [40] R. Jain, M. Mathur, S. Sikarwar, and A. Mittal. Removal of the hazardous dye rhodamine b through photocatalytic and adsorption treatments. *Journal of Environmental Management*, 85(4):956–964, 2007.
- [41] Mustafa Soylak, Yunus Emre Unsal, Erkan Yilmaz, and Mustafa Tuzen. Determination of rhodamine b in soft drink, waste water and lipstick samples after solid phase extraction. *Food and Chemical Toxicology*, 49(8):1796 – 1799, 2011.
- [42] Kai Shen and M.A. Gondal. Removal of hazardous rhodamine dye from water by adsorption onto exhausted coffee ground. *Journal of Saudi Chemical Society*, 2013.
- [43] Syiska Atikl Maryanti, Siti Suciati, Endang Sri Wahyuni, Sanarto Santoso, and I Wayan Arsana Wiyasa. Rhodamine b triggers ovarian toxicity through oxidative stress, decreases in the number of follicles, 17 β -estradiol level, and thickness of endometrium. *Cukurova Medical Journal*, 39(3):451–457, 2014.
- [44] N. Subrahmanyam, B. Lal, and N. Avadhanulu. *A Text Book of Optics*. S. Chand Limited, 2004.
- [45] C E Lee, J J Alcoz, Y Yeh, W N Gibler, R A Atkins, and H F Taylor. Optical fiber fabry-perot sensors for smart structures. *Smart Materials and Structures*, 1(2):123, 1992.

- [46] Tao Zhu, Di Wu, Min Liu, and De-Wen Duan. In-line fibre optic interferometric sensors in single-mode fibres. *Sensors*, 12(8):10430, 2012.
- [47] J.L. Santos and F. Farahi. *Handbook of Optical Sensors*. Taylor & Francis, 2014.
- [48] I Juvells, A Carnicer, J Ferr-Borrull, E Martn-Badosa, and M Montes-Usategui. Understanding the concept of resolving power in the fabry perot interferometer using a digital simulation. *European Journal of Physics*, 27(5):1111, 2006.
- [49] Ian J. Hodgkinson, Qihong Wu, and Martin W. McCall. *Birefringent Thin Films and Polarizing Elements*. Imperial College Press, 2014.
- [50] Ghenadii Korotcenkov. *Chemical Sensors. Simulation and Modeling Volume 4: Optical Sensors*. New York : Momentum Press, 2013.
- [51] B.D. Mac Craith, C. McDonagh, G. O’Keeffe, T. Butler, B. O’Kelly, and J.F. McGilp. Fibre optic chemical sensors based on evanescent wave interactions in sol-gel-derived porous coatings. *Journal of Sol-Gel Science and Technology*, 2(1-3):661–665, 1994.
- [52] P Suresh Kumar, C P G Vallabhan, V P N Nampoore, V N Sivasankara Pillai, and P Radhakrishnan. A fibre optic evanescent wave sensor used for the detection of trace nitrites in water. *Journal of Optics A: Pure and Applied Optics*, 4(3):247, 2002.
- [53] Harpreet K. Bal, Zourab Brodzeli, Nicoleta M. Dragomir, Stephen F. Collins, and Fotios Sidiroglou. Uniformly thinned optical fibres produced via hf etching with spectral and microscopic verification. *Appl. Opt.*, 51(13):2282–2287, May 2012.

- [54] Xiaoyi Dong, Hao Zhang, Bo Liu, and Yinping Miao. Tilted fibre bragg gratings: Principle and sensing applications. *Photonic Sensors*, 1(1):6–30, 2011.
- [55] Zhengtian Gu, Jinlong Lan, Haiyun Chen, and Kan Gao. Characteristics and design of coated lpg sensor based on mode transition. In *Numerical Simulation of Optoelectronic Devices (NUSOD), 2013 13th International Conference on*, pages 51–52, Aug 2013.
- [56] S.W. James and R.P. Tatam. Optical fibre long-period grating sensors: Characteristics and application. *Measurement Science and Technology*, 14(5):R49–R61, 2003.
- [57] Stefan Huber, Arantzazu Zabala Ruiz, Huanrong Li, Greta Patrinoiu, Chiara Botta, and Gion Calzaferri. Optical spectroscopy of inorganic organic host guest nanocrystals organized as oriented monolayers. *Inorganica Chimica Acta*, 360(3):869 – 875, 2007. Protagonists in Chemistry: Vincenzo Balzani.
- [58] M. Noack, P. Klsch, V. Seefeld, P. Toussaint, G. Georgi, and J. Caro. Influence of the si/al ratio on the permeation properties of mfi membranes. *Microporous and Mesoporous Materials*, 79(1-3):329–337, 2005.
- [59] Sankar Nair, Zhiping Lai, Vladimiro Nikolakis, George Xomeritakis, Griselda Bonilla, and Michael Tsapatsis. Separation of close-boiling hydrocarbon mixtures by mfi and fau membranes made by secondary growth. *Microporous and Mesoporous Materials*, 48(13):219 – 228, 2001.

- [60] Xuehong Gu, Junhang Dong, and Tina M. Nenoff. Synthesis of defect-free fau-type zeolite membranes and separation for dry and moist CO_2/N_2 mixtures. *Industrial and Engineering Chemistry Research*, 44(4):937–944, 2005.
- [61] Takaaki Matsufuji, Norikazu Nishiyama, Masahiko Matsukata, and Korekazu Ueyama. Separation of butane and xylene isomers with mfi-type zeolitic membrane synthesized by a vapor-phase transport method. *Journal of Membrane Science*, 178(12):25 – 34, 2000.
- [62] L. Zhou, T. Wang, Q.T. Nguyen, J. Li, Y. Long, and Z. Ping. Cordierite supported zsm-5 membrane: Preparation and pervaporation properties in the dehydration of water-alcohol mixture. *Separation and Purification Technology*, 44(3):266–270, 2005.
- [63] L. Li, N. Liu, B. McPherson, and R. Lee. Enhanced water permeation of reverse osmosis through mfi-type zeolite membranes with high aluminum contents. *Industrial and Engineering Chemistry Research*, 46(5):1584–1589, 2007.
- [64] Shiguang Li, Vu A. Tuan, Richard D. Noble, and John L. Falconer. A ge-substituted zsm-5 zeolite membrane for the separation of acetic acid from water. *Industrial and Engineering Chemistry Research*, 40(26):6165–6171, 2001.
- [65] Travis C Bowen, Halil Kalipcilar, John L Falconer, and Richard D Noble. Pervaporation of organic/water mixtures through b-zsm-5 zeolite membranes on monolith supports. *Journal of Membrane Science*, 215(12):235 – 247, 2003.

- [66] Vu A Tuan, Shiguang Li, John L Falconer, and Richard D Noble. Separating organics from water by pervaporation with isomorphously-substituted mfi zeolite membranes. *Journal of Membrane Science*, 196(1):111 – 123, 2002.
- [67] X. Zou, G. Zhu, H. Guo, X. Jing, D. Xu, and S. Qiu. Effective heavy metal removal through porous stainless-steel-net supported low siliceous zeolite zsm-5 membrane. *Microporous and Mesoporous Materials*, 124(1-3):70–75, 2009.
- [68] O Hugon, M Sauvan, P Benech, C Pijolat, and F Lefebvre. Gas separation with a zeolite filter, application to the selectivity enhancement of chemical sensors. *Sensors and Actuators B: Chemical*, 67(3):235 – 243, 2000.
- [69] Jian Zhang, Xiling Tang, Junhang Dong, Tao Wei, and Hai Xiao. Zeolite thin film-coated long period fibre grating sensor for measuring trace organic vapors. *Sensors and Actuators B: Chemical*, 135(2):420 – 425, 2009.
- [70] Hai Xiao, Jian Zhang, Junhang Dong, Ming Luo, Robert Lee, and Van Romero. Synthesis of mfi zeolite films on optical fibres for detection of chemical vapours. *Opt. Lett.*, 30(11):1270–1272, Jun 2005.
- [71] Graham Walsh, Cunqiang Sun, Hai Xiao, Ning Liu, Junhang Dong, and Van Romero. An optical fibre based microsensor for explosives detection. volume 6217, pages 62171L–62171L–6. 10.1117/12.665572.
- [72] N. Liu, L. Li, and R. Lee. Fabrication of an integrated zeolite-fibre optical chemical sensor for detection of mercury (ii) ion in water. *Sensors and Transducers*, 131(8):43–51, 2011.

- [73] Ning Liu, Juan Hui, Cunqiang Sun, Junhang Dong, Luzheng Zhang, and Hai Xiao. Nanoporous zeolite thin film-based fibre intrinsic Fabry Perot interferometric sensor for detection of dissolved organics in water. *Sensors*, 6(8):835–847, 2006.
- [74] Bradley P Ladewig, Richelle Lyndon, and Matthew R Hill. The carbon sponge: squeezing out captured carbon dioxide. *Carbon Management*, 5(1):9–11, 2014.
- [75] Hiroyasu Furukawa, Kyle E. Cordova, Michael O’Keeffe, and Omar M. Yaghi. The chemistry and applications of metal-organic frameworks. *Science*, 341(6149), 2013.
- [76] Akili D. Khawaji, Ibrahim K. Kutubkhanah, and Jong-Mihn Wie. Advances in seawater desalination technologies. *Desalination*, 221(13):47 – 69, 2008.
- [77] M.A. Shannon, P.W. Bohn, M. Elimelech, J.G. Georgiadis, B.J. Maras, and A.M. Mayes. Science and technology for water purification in the coming decades. *Nature*, 452(7185):301–310, 2008.
- [78] Miguel Angelo Granato, Vanessa Duarte Martins, Alexandre Filipe P. Ferreira, and Alrio E. Rodrigues. Adsorption of xylene isomers in mof uio-66 by molecular simulation. *Microporous and Mesoporous Materials*, 190(0):165 – 170, 2014.
- [79] Aderonke Ajibola Adeyemo, Idowu Olatunbosun Adeoye, and Olugbenga Solomon Bello. Metal organic frameworks as adsorbents for dye adsorption: overview, prospects and future challenges. *Toxicological and Environmental Chemistry*, 94(10):1846–1863, 2012.

- [80] Xie Liting Liu Dahuan Yang Qingyuan Zhong Chongli Tong Minman, Zhao Xudong. Treatment of waste water using metal-organic frameworks. *Progress in Chemistry*, (9):1646, 2012.
- [81] Siew-Teng Ong, Pei-Sin Keng, Weng-Nam Lee, Sie-Tiong Ha, and Yung-Tse Hung. Dye waste treatment. *Water*, 3(1):157, 2011.
- [82] Kun-Yi Andrew Lin, Hsuan-Ang Chang, and Chung-Jun Hsu. Iron-based metal organic framework, mil-88a, as a heterogeneous persulfate catalyst for decolorization of rhodamine b in water. *RSC Adv.*, 5:32520–32530, 2015.
- [83] Kyo Sung Park, Zheng Ni, Adrien P. Ct, Jae Yong Choi, Rudan Huang, Fernando J. Uribe-Romo, Hee K. Chae, Michael O'Keeffe, and Omar M. Yaghi. Exceptional chemical and thermal stability of zeolitic imidazolate frameworks. *Proceedings of the National Academy of Sciences*, 103(27):10186–10191, 2006.
- [84] Jin Chong Tan, Thomas D. Bennett, and Anthony K. Cheetham. Chemical structure, network topology, and porosity effects on the mechanical properties of zeolitic imidazolate frameworks. *Proceedings of the National Academy of Sciences*, 107(22):9938–9943, 2010.
- [85] Enamul Haque, Ji Eun Lee, In Tae Jang, Young Kyu Hwang, Jong-San Chang, Jonggeon Jegal, and Sung Hwa Jung. Adsorptive removal of methyl orange from aqueous solution with metal-organic frameworks, porous chromium-benzenedicarboxylates. *Journal of Hazardous Materials*, 181(13):535 – 542, 2010.

- [86] Aderonke Ajibola Adeyemo, Idowu Olatunbosun Adeoye, and Olugbenga Solomon Bello. Metal organic frameworks as adsorbents for dye adsorption: overview, prospects and future challenges. *Toxicological and Environmental Chemistry*, 94(10):1846–1863, 2012.
- [87] Chen Chen, Meng Zhang, Qingxin Guan, and Wei Li. Kinetic and thermodynamic studies on the adsorption of xylenol orange onto mil-101(cr). *Chemical Engineering Journal*, 183(0):60 – 67, 2012.
- [88] Shu-Hui Huo and Xiu-Ping Yan. Metal-organic framework mil-100(fe) for the adsorption of malachite green from aqueous solution. *J. Mater. Chem.*, 22:7449–7455, 2012.
- [89] Wei Xia, Xiangmei Zhang, Ling Xu, Yingxia Wang, Jianhua Lin, and Ruqiang Zou. Facile and economical synthesis of metal-organic framework mil-100(al) gels for high efficiency removal of microcystin-lr. *RSC Adv.*, 3:11007–11013, 2013.
- [90] Enamul Haque, Jong Won Jun, and Sung Hwa Jung. Adsorptive removal of methyl orange and methylene blue from aqueous solution with a metal-organic framework material, iron terephthalate (mof-235). *Journal of Hazardous Materials*, 185(1):507 – 511, 2011.
- [91] Chi Yang, Ushasree Kaipa, Qian Zhang Mather, Xiaoping Wang, Vladimir Nesterov, Augustin F. Venero, and Mohammad A. Omary. Fluorous metalorganic frameworks with superior adsorption and hydrophobic properties toward oil spill

- cleanup and hydrocarbon storage. *Journal of the American Chemical Society*, 133(45):18094–18097, 2011. PMID: 21981413.
- [92] Eun Young Park, Zubair Hasan, Nazmul Abedin Khan, and Sung Hwa Jung. Adsorptive removal of bisphenol-a from water with a metal-organic framework, a porous chromium-benzenedicarboxylate. *Journal of Nanoscience and Nanotechnology*, 13(4):2789–2794, 2013-04-01T00:00:00.
- [93] Feng-Xiang Qin, Shao-Yi Jia, Yong Liu, Hao-Yang Li, and Song-Hai Wu. Adsorptive removal of bisphenol a from aqueous solution using metal-organic frameworks. *Desalination and Water Treatment*, 54(1):93–102, 2015.
- [94] Gregory W. Peterson, Joseph A. Rossin, Jared B. DeCoste, Kato L. Killops, Matthew Browe, Erica Valdes, and Paulette Jones. Zirconium hydroxidemet-alorganic framework composites for toxic chemical removal. *Industrial and Engineering Chemistry Research*, 52(15):5462–5469, 2013.
- [95] Elham Tahmasebi, Mohammad Yaser Masoomi, Yadollah Yamini, and Ali Morsali. Application of mechanosynthesized azine-decorated zinc(ii) metalorganic frameworks for highly efficient removal and extraction of some heavy-metal ions from aqueous samples: A comparative study. *Inorganic Chemistry*, 54(2):425–433, 2015. PMID: 25548873.
- [96] Xinlei Liu, Nilay Keser Demir, Zhentao Wu, and Kang Li. Highly water-stable zirconium metalorganic framework uio-66 membranes supported on alumina hollow fibers for desalination. *Journal of the American Chemical Society*, 137(22):6999–7002, 2015. PMID: 26023819.

- [97] Zhou Sha, Jiulong Sun, Hardy Sze On Chan, Stephan Jaenicke, and Jishan Wu. Enhanced photocatalytic activity of the agi/uio-66(zr) composite for rhodamineb degradation under visible-light irradiation. *ChemPlusChem*, pages n/a–n/a, 2015.
- [98] Hai-Bo Shang, Cheng-Xiong Yang, and Xiu-Ping Yan. Metalorganic framework uio-66 coated stainless steel fiber for solid-phase microextraction of phenols in water samples. *Journal of Chromatography A*, 1357(0):165 – 171, 2014. *Advanced Materials for Separation Science*.
- [99] Zhou Sha, Jiulong Sun, Hardy Sze On Chan, Stephan Jaenicke, and Jishan Wu. Bismuth tungstate incorporated zirconium metal-organic framework composite with enhanced visible-light photocatalytic performance. *RSC Adv.*, 4:64977–64984, 2014.
- [100] Zhou Sha and Jishan Wu. Enhanced visible-light photocatalytic performance of bio-br/uio-66(zr) composite for dye degradation with the assistance of uio-66. *RSC Adv.*, 5:39592–39600, 2015.
- [101] Lijuan Shen, Weiming Wu, Ruowen Liang, Rui Lin, and Ling Wu. Highly dispersed palladium nanoparticles anchored on uio-66(nh₂) metal-organic framework as a reusable and dual functional visible-light-driven photocatalyst. *Nanoscale*, 5:9374–9382, 2013.
- [102] Rachel C Huxford, Joseph Della Rocca, and Wenbin Lin. Metalorganic frameworks as potential drug carriers. *Current Opinion in Chemical Biology*, 14(2):262 – 268, 2010. *Biocatalysis and Biotransformation/Bioinorganic Chemistry*.

- [103] Xiangyang Zhu, Jinlou Gu, Yao Wang, Bing Li, Yongsheng Li, Wenru Zhao, and Jianlin Shi. Inherent anchorages in uio-66 nanoparticles for efficient capture of alendronate and its mediated release. *Chem. Commun.*, 50:8779–8782, 2014.
- [104] Patricia Horcajada, Christian Serre, Guillaume Maurin, Naseem A. Ramsahye, Francisco Balas, Mara Vallet-Reg, Muriel Sebban, Francis Taulelle, and Grard Frey. Flexible porous metal-organic frameworks for a controlled drug delivery. *Journal of the American Chemical Society*, 130(21):6774–6780, 2008. PMID: 18454528.
- [105] Patricia Horcajada, Christian Serre, Mara Vallet-Reg, Muriel Sebban, Francis Taulelle, and Grard Frey. Metalorganic frameworks as efficient materials for drug delivery. *Angewandte Chemie International Edition*, 45(36):5974–5978, 2006.
- [106] ngels Ruyra, Amirali Yazdi, Jordi Espn, Arnau Carn-Snchez, Nerea Roher, Julia Lorenzo, Inhar Imaz, and Daniel Maspoch. Synthesis, culture medium stability, and in vitro and in vivo zebrafish embryo toxicity of metalorganic framework nanoparticles. *Chemistry A European Journal*, 21(6):2508–2518, 2015.
- [107] Cristina Tamames-Tabar, Denise Cunha, Edurne Imbuluzqueta, Florence Ragon, Christian Serre, Maria J. Blanco-Prieto, and Patricia Horcajada. Cytotoxicity of nanoscaled metal-organic frameworks. *J. Mater. Chem. B*, 2:262–271, 2014.
- [108] Chun-Yi Sun, Chao Qin, Xin-Long Wang, and Zhong-Min Su. Metal-organic frameworks as potential drug delivery systems. *Expert Opinion on Drug Delivery*, 10(1):89–101, 2013. PMID: 23140545.

- [109] Maria C. Bernini, David Fairen-Jimenez, Marcelo Pasinetti, Antonio J. Ramirez-Pastor, and Randall Q. Snurr. Screening of bio-compatible metal-organic frameworks as potential drug carriers using monte carlo simulations. *J. Mater. Chem. B*, 2:766–774, 2014.
- [110] C.G. Piscopo, A. Polyzoidis, M. Schwarzer, and S. Loebbecke. Stability of uio-66 under acidic treatment: Opportunities and limitations for post-synthetic modifications. *Microporous and Mesoporous Materials*, 208(0):30 – 35, 2015.
- [111] Agilent Technologies, Inc. *Agilent 83438A Erbium ASE Source Product Overview*.
- [112] Jia-Rong Zhao, Xu-Guang Huang, Wei-Xin He, and Ji-Huan Chen. High-resolution and temperature-insensitive fiber optic refractive index sensor based on fresnel reflection modulated by fabry perot interference. *Lightwave Technology, Journal of*, 28(19):2799–2803, Oct 2010.
- [113] Bing Qi, Gary R. Pickrell, JunCheng Xu, Po Zhang, Yuhong Duan, Wei Peng, Zhenyu Huang, Wei Huo, Hai Xiao, Russell G. May, and Anbo Wang. Novel data processing techniques for dispersive white light interferometer. *Optical Engineering*, 42(11):3165–3171, 2003.
- [114] Jiehui Xie, Fuyin Wang, Yao Pan, Junjie Wang, Zhengliang Hu, and Yongming Hu. High resolution signal-processing method for extrinsic fabry perot interferometric sensors. *Optical Fiber Technology*, 22:1 – 6, 2015.
- [115] Z. Wang, Y. Jiang, W. Ding, and R. Gao. A cross-correlation based fibre optic white-light interferometry with wavelet transform denoising. volume 8924, 2013.

- [116] Ingrid Daubechies. Chapter 3 - discrete wavelet transforms: Frames. In *Ten Lectures on Wavelets*, pages 53–105. 1992.
- [117] Mallat Stphane. Chapter 7 - wavelet bases. In *A Wavelet Tour of Signal Processing (Third Edition)*, pages 263 – 376. Academic Press, Boston, third edition edition, 2009.
- [118] K. R. Rao, D. N. Kim, and J.-J. Hwang. *Fast Fourier Transform - Algorithms and Applications*. Springer Publishing Company, Incorporated, 1st edition, 2010.
- [119] J. Treacy and J.B. Higgins. *Collection of Simulated XRD Powder Patterns for Zeolites Fifth (5th) Revised Edition*. Collection of Simulated XRD Powder Patterns for Zeolites. Elsevier Science, 2007.
- [120] Xiling Tang, Justin Provenzano, Zhi Xu, Junhang Dong, Hongbiao Duan, and Hai Xiao. Acidic zsm-5 zeolite-coated long period fibre grating for optical sensing of ammonia. *J. Mater. Chem.*, 21:181–186, 2011.
- [121] P. Atkins, J. De Paula, and V. Walters. *Physical Chemistry*. Macmillan Higher Education, 2006.
- [122] David Ohayon, Raymond Le Van Mao, David Ciaravino, Helen Hazel, Angeline Cochenec, and Nolwenn Rolland. Methods for pore size engineering in zsm-5 zeolite. *Applied Catalysis A: General*, 217(12):241 – 251, 2001.
- [123] T.C Jorgensen and L.R Weatherley. Ammonia removal from wastewater by ion exchange in the presence of organic contaminants. *Water Research*, 37(8):1723 – 1728, 2003.

- [124] Bo Zhu, Cara M. Doherty, Xiurong Hu, Anita J. Hill, Linda Zou, Y.S. Lin, and Mikel Duke. Designing hierarchical porous features of zsm-5 zeolites via si/al ratio and their dynamic behavior in seawater ion complexes. *Microporous and Mesoporous Materials*, 173:78 – 85, 2013.
- [125] Travis C. Bowen, Richard D. Noble, and John L. Falconer. Fundamentals and applications of pervaporation through zeolite membranes. *Journal of Membrane Science*, 245(12):1 – 33, 2004.
- [126] Nicolas Brodu, Marie-Hlne Manero, Caroline Andriantsiferana, Jean-Stphane Pic, and Hctor Valds. Role of lewis acid sites of zsm-5 zeolite on gaseous ozone abatement. *Chemical Engineering Journal*, 231(0):281 – 286, 2013.
- [127] Li Can and Wu Zili. *Microporous Materials Characterized by Vibrational Spectroscopies*. CRC Press, 2003. doi:10.1201/9780203911167.ch11.
- [128] F. Eder, M. Stockenhuber, and J.A. Lercher. Sorption of light alkanes on h-zsm5 and h-mordenite. In Laurent Bonneviot and Serge Kaliaguine, editors, *Zeolites: A Refined Tool for Designing Catalytic Sites Proceedings of the International Zeolite Symposium*, volume 97 of *Studies in Surface Science and Catalysis*, pages 495 – 500. Elsevier, 1995.
- [129] Jared B. DeCoste, Gregory W. Peterson, Bryan J. Schindler, Kato L. Killops, Matthew A. Browe, and John J. Mahle. The effect of water adsorption on the structure of the carboxylate containing metal-organic frameworks cu-btc, mg-mof-74 and uio-66. *J. Mater. Chem. A*, 1:11922–11932, 2013.

- [130] Eric Cockayne and Eric B. Nelson. Density functional theory meta-gga + u study of water incorporation in the metal-organic framework material cu-btc. *The Journal of Chemical Physics*, 143(2):–, 2015.
- [131] Hiroyasu Furukawa, Felipe Gndara, Yue-Biao Zhang, Juncong Jiang, Wendy L. Queen, Matthew R. Hudson, and Omar M. Yaghi. Water adsorption in porous metalorganic frameworks and related materials. *Journal of the American Chemical Society*, 136(11):4369–4381, 2014. PMID: 24588307.
- [132] Andreas Schaate, Pascal Roy, Adelheid Godt, Jann Lippke, Florian Waltz, Michael Wiebcke, and Peter Behrens. Modulated synthesis of zr-based metalorganic frameworks: From nano to single crystals. *Chemistry A European Journal*, 17(24):6643–6651, 2011.
- [133] Mohamed Eddaoudi, David B. Moler, Hailian Li, Banglin Chen, Theresa M. Reineke, Michael O’Keeffe, and Omar M. Yaghi. Modular chemistry: secondary building units as a basis for the design of highly porous and robust metalorganic carboxylate frameworks. *Accounts of Chemical Research*, 34(4):319–330, 2001. PMID: 11308306.
- [134] Loredana Valenzano, Bartolomeo Civalleri, Sachin Chavan, Silvia Bordiga, Merete H. Nilsen, Sren Jakobsen, Karl Petter Lillerud, and Carlo Lamberti. Disclosing the complex structure of uio-66 metal organic framework: A synergic combination of experiment and theory. *Chemistry of Materials*, 23(7):1700–1718, 2011.

- [135] Denise Zacher, Osama Shekhah, Christof Woll, and Roland A. Fischer. Thin films of metal-organic frameworks. *Chem. Soc. Rev.*, 38:1418–1429, 2009.
- [136] O. Shekhah, J. Liu, R. A. Fischer, and Ch. Woll. Mof thin films: existing and future applications. *Chem. Soc. Rev.*, 40:1081–1106, 2011.
- [137] Guang Lu and Joseph T. Hupp. Metalorganic frameworks as sensors: A zif-8 based fabry perot device as a selective sensor for chemical vapors and gases. *Journal of the American Chemical Society*, 132(23):7832–7833, 2010. PMID: 20486704.
- [138] Constantinos Dimitrakakis, Christopher D. Easton, Benjamin W. Muir, Bradley P. Ladewig, and Matthew R. Hill. Spatial control of zeolitic imidazolate framework growth on flexible substrates. *Crystal Growth and Design*, 13(10):4411–4417, 2013.
- [139] Qi Chen, Qinqin He, Mengmeng Lv, Yanli Xu, Hanbiao Yang, Xueting Liu, and Fengyu Wei. Selective adsorption of cationic dyes by uio-66-nh2. *Applied Surface Science*, 327:77 – 85, 2015.
- [140] Yan-Qiu Zhang, Chong-Chen Wang, Tian Zhu, Peng Wang, and Shi-Jie Gao. Ultra-high uptake and selective adsorption of organic dyes with a novel polyoxomolybdate-based organic-inorganic hybrid compound. *RSC Adv.*, 5:45688–45692, 2015.
- [141] Qinqin He, Qi Chen, Mengmeng L, and Xueting Liu. Adsorption behavior of rhodamine b on uio-66. *Chinese Journal of Chemical Engineering*, 22(1112):1285 – 1290, 2014.

References

- [142] M Kara, H Yuzer, E Sabah, and M.S Celik. Adsorption of cobalt from aqueous solutions onto sepiolite. *Water Research*, 37(1):224 – 232, 2003.
- [143] Ivari Kaljurand, Toomas Rodima, Ivo Leito, Ilmar A. Koppel, and Reinhard Schwesinger. Self-consistent spectrophotometric basicity scale in acetonitrile covering the range between pyridine and dbu. *The Journal of Organic Chemistry*, 65(19):6202–6208, 2000. PMID: 10987960.
- [144] Sachin Chavan, Jenny G. Vitillo, Diego Gianolio, Olena Zavorotynska, Bartolomeo Civalleri, Soren Jakobsen, Merete H. Nilsen, Loredana Valenzano, Carlo Lamberti, Karl Petter Lillerud, and Silvia Bordiga. H₂storage in isostructural uio-67 and uio-66 mofs. *Phys. Chem. Chem. Phys.*, 14:1614–1626, 2012.
- [145] Niederhuber, Armitage, Doroshov, Kastan, and Tepper. *Abeloff's Clinical Oncology*. Saunders, 5th edition edition.
- [146] Julie Lemieux, Elizabeth Maunsell, and Louise Provencher. Chemotherapy-induced alopecia and effects on quality of life among women with breast cancer: a literature review. *Psycho-Oncology*, 17(4):317–328, 2008.
- [147] Kerryann Lotfi-Jam, Mariko Carey, Michael Jefford, Penelope Schofield, Catherine Charleson, and Sanchia Aranda. Nonpharmacologic strategies for managing common chemotherapy adverse effects: A systematic review. *Journal of Clinical Oncology*, 26(34):5618–5629, 2008.
- [148] Accelrys. *Materials Studio*. San Diego, 2014.

References

- [149] Jrn Ilja Siepmann and Daan Frenkel. Configurational bias Monte Carlo: a new sampling scheme for flexible chains. *Molecular Physics*, 75(1):59–70, January 1992.
- [150] D Frenkel and G C A M Mooij and B Smit. Novel scheme to study structural and thermal properties of continuously deformable molecules. *Journal of Physics: Condensed Matter*, 4(12):3053, 1992.
- [151] Juan J. de Pablo, Manuel Laso, and Ulrich W. Suter. Simulation of polyethylene above and below the melting point. *The Journal of Chemical Physics*, 96(3):2395–2403, 1992.
- [152] T. J. H. VLUGT, M. G. MARTIN, B. SMIT, J. I. SIEPMANN, and R. KRISHNA. Improving the efficiency of the configurational-bias Monte Carlo algorithm. *Molecular Physics*, 94(4):727–733, July 1998.
- [153] Marcus G. Martin and J. Ilja Siepmann. Novel Configurational-Bias Monte Carlo Method for Branched Molecules. Transferable Potentials for Phase Equilibria. 2. United-Atom Description of Branched Alkanes. *The Journal of Physical Chemistry B*, 103(21):4508–4517, May 1999.
- [154] A. K. Rappe, C. J. Casewit, K. S. Colwell, W. A. Goddard, and W. M. Skiff. UFF, a full periodic table force field for molecular mechanics and molecular dynamics simulations. *Journal of the American Chemical Society*, 114(25):10024–10035, December 1992.

- [155] Anthony K. Rappe and William A. Goddard. Charge equilibration for molecular dynamics simulations. *The Journal of Physical Chemistry*, 95(8):3358–3363, April 1991.
- [156] G. Kresse and J. Hafner. ab-initio molecular dynamics for open-shell transition metals. *Physical Review B*, 48(17):13115–13118, November 1993.
- [157] G. Kresse and J. Furthmüller. Efficiency of ab-initio total energy calculations for metals and semiconductors using a plane-wave basis set. *Computational Materials Science*, 6(1):15–50, July 1996.
- [158] John P. Perdew, Kieron Burke, and Matthias Ernzerhof. Generalized gradient approximation made simple. *Phys. Rev. Lett.*, 77:3865–3868, Oct 1996.
- [159] Stefan Grimme. Semiempirical gga-type density functional constructed with a long-range dispersion correction. *Journal of Computational Chemistry*, 27(15):1787–1799, 2006.
- [160] K. Kavitha, A. Srinivasa Rao, and C.N. Nalini. An investigation on enhancement of solubility of 5 fluorouracil by applying complexation technique-characterization, dissolution and molecular-modeling studies. *Journal of Applied Pharmaceutical Science*, 3(3):162–166, 2013.
- [161] R. Ishii, H. Mori, K. Matsumura, N. Hongo, H. Kiyosue, S. Matsumoto, T. Yoshimi, and S. Ujiie. Molecular interactions between anticancer drugs and iodinated contrast media: An in vitro spectroscopic study. *Journal of Biomedical Science and Engineering*, 5:24–33, 2012.

- [162] G.N. Ten, T.G. Burova, and V.I. Baranov. Calculation and interpretation of ir and resonant raman spectra of 5-halosubstituted uracils. *Journal of Applied Spectroscopy*, 73(4):492–498, 2006.
- [163] Denise Cunha, Mouna Ben Yahia, Shaun Hall, Stuart R. Miller, Hubert Chevreau, Erik Elkam, Guillaume Maurin, Patricia Horcajada, and Christian Serre. Rationale of drug encapsulation and release from biocompatible porous metal organic frameworks. *Chemistry of Materials*, 25(14):2767–2776, 2013.
- [164] Andres Canales, Xiaoting Jia, Ulrich P Froriep, Ryan A Koppes, Christina M Tringides, Jennifer Selvidge, Chi Lu, Chong Hou, Lei Wei, Yoel Fink, and Polina Anikeeva. Multifunctional fibers for simultaneous optical, electrical and chemical interrogation of neural circuits in vivo. *Nat Biotech*, 33(3):277–284, March 2015.
- [165] Yoan Le Chasseur, Suzie Dufour, Guillaume Lavertu, Cyril Bories, Martin Deschenes, Real Vallee, and Yves De Koninck. A microprobe for parallel optical and electrical recordings from single neurons in vivo. *Nat Meth*, 8(4):319–325, April 2011.
- [166] P. G. Dinning, L. Wiklendt, L. Maslen, V. Patton, H. Lewis, J. W. Arkwright, D. A. Wattchow, D. Z. Lubowski, M. Costa, and P. A. Bampton. Colonic motor abnormalities in slow transit constipation defined by high resolution, fibre-optic manometry. *Neurogastroenterology and Motility*, 27(3):379–388, 2015.

- [167] Gyungseok Oh, Euiheon Chung, and Seok H. Yun. Optical fibers for high-resolution in vivo microendoscopic fluorescence imaging. *Optical Fiber Sensors*, 19(6, Part B):760–771, December 2013.
- [168] John W. Arkwright, Ian D. Underhill, Simon A. Maunder, Neil Blenman, Michal M. Szczesniak, Lukasz Wiklendt, Ian J. Cook, David Z. Lubowski, and Phil G. Dinning. Design of a high-sensor count fibre optic manometry catheter for in-vivo colonic diagnostics. *Opt. Express*, 17(25):22423–22431, Dec 2009.
- [169] P. G. Dinning, L. M. Hunt, J. W. Arkwright, V. Patton, M. M. Szczesniak, L. Wiklendt, J. B. Davidson, D. Z. Lubowski, and I. J. Cook. Pancolonic motor response to subsensory and suprasensory sacral nerve stimulation in patients with slow-transit constipation. *British Journal of Surgery*, 99(7):1002–1010, 2012.
- [170] M. Wasif Saif, Adrienne Choma, Salvatore J. Salamone, and Edward Chu. Pharmacokinetically Guided Dose Adjustment of 5-Fluorouracil: A Rational Approach to Improving Therapeutic Outcomes. *Journal of the National Cancer Institute*, 101(22):1543–1552, November 2009.
- [171] G. Des Guetz, B. Uzzan, J.F. Morere, G. Perret, and P. Nicolas. Duration of adjuvant chemotherapy for patients with non-metastatic colorectal cancer. *Cochrane database of systematic reviews (Online)*, (1), 2010.
- [172] The Netherlands Pharmachemie BV., Haarlem. *Physician’s Package Insert, FLUOROURACIL*. Ministry of Health.
- [173] F. Cavalli, S.B. Kaye, H.H. Hansen, J.O. Armitage, and M. Piccart-Gebhart. *Textbook of Medical Oncology*. CRC Press, 2009.